Vamsi Prakash Makkapati, Dipl.-Ing.

Performance improvement of servo drive systems involving an elastic coupling

DOCTORAL THESIS

to achieve the university degree of

Doktor der technischen Wissenschaften

submitted to

Graz University of Technology

Supervisor:
Univ.-Prof. Dipl-Ing. Dr.techn. Martin Horn

Institute of Automation and Control
Graz University of Technology

Graz, April 2016

This document is set in Palatino, compiled with pdfLaTeX2e and `Biber`.

The LaTeX template from Karl Voit is based on KOMA script and can be found online: https://github.com/novoid/LaTeX-KOMA-template

AFFIDAVIT

I declare that I have authored this thesis independently, that I have not used other than the declared sources/resources, and that I have explicitly indicated all material which has been quoted either literally or by content from the sources used. The text document uploaded to TUGRAZonline is identical to the present doctoral thesis.

Graz, _____ _____

Date Signature

Abstract

With the improvements in power densities of electric motors and their capability of an almost instantaneous torque generation, dynamics of the mechanical drive-trains becomes more critical in the servo drive systems employing these motors. And the dynamics of these drive-trains depend on the (often) under-damped shafts and elastic couplings that are typically employed. Impulsive torques from the motors may excite mechanical resonances in these drive-trains which lead to torsional oscillations, ultimately degrading the performance of motion control systems.
The work presented in this thesis deals with the performance improvement of the motion controller for an oscillatory servo drive system. First a classification is made for the problems involving mechanical resonance based on how the speed control loop is influenced by the mechanical resonance. Then, for the case of low-frequency resonance the acceleration feedback approach is applied and an extension is proposed for the considered problem. It is also apparent that dead times within the considered mechatronic system have a negative influence on the achievable closed loop performance. A method for modelling the plant with dead time as a non-minimum phase system is exploited for designing a model based tracking controller based on the so-called stable system center approach. The developed techniques are evaluated on experimental testbenches.

Kurzfassung

Die ständige Verbesserung von Elektromotoren, z.B. hinsichtlich ihrer Leistungsdichte, ermöglicht die Erzeugung hoher Drehmomentspitzen innerhalb kürzester Zeiten. Dies führt dazu, dass innerhalb des von diesen Motoren aktuierten mechanischen Systems – beispielsweise ein Antriebsstrang – unerwünschte Schwingungen angeregt werden können. Die Dynamik dieser mechanischen Systeme ist häufig durch schwach gedämpfte Wellen und elastische Kupplungen geprägt. In einem Antriebsstrang können Momentenspitzen des elektrischen Antriebes daher zu unerwünschten Torsionsschwingungen führen.

Diese Arbeit beschäftigt sich mit der Verbesserung der Antriebsregelung eines elektrischen Motors als Teil eines mechatronischen, schwingungsfähigen Systems. Zunächst wird eine Klassifikation der Problemstellung erläutert. Für den Fall "niedriger" Resonanzfrequenzen wird das "acceleration feedback"-Verfahren verwendet, das in dieser Arbeit für die betrachtete Problemstellung entsprechend erweitert wird. Es zeigt sich, dass auch bei den zugrunde liegenden mechatronischen Systemen Totzeiten einen negativen Einfluss auf die erreichbare Qualität des geschlossenen Regelkreises haben. Es wird eine Methode zur Modellierung der Totzeit verwendet, die zu einem nicht phasenminimalen Modell der Regelstrecke führt. Darauf aufbauend wird mit der Methode der "stable system center" eine modellbasierte Regelung entworfen. Die Praxistauglichkeit der erarbeiteten Regelungsmethoden wird an Prüfständen demonstriert.

Acknowledgements

This thesis would not have been possible without the inspiration and support of a number of wonderful individuals with whom I was involved with during my time working at the Alpen-Adria University of Klagenfurt and Graz University of technology.

I owe my deepest gratitude to my supervisor Univ.-Prof. Dipl.-Ing. Dr.tech. Martin Horn for giving me the opportunity to work on this thesis and for his patience, constant encouragement and support throughout my doctoral studies.

Special thanks go to my second supervisor Prof. Dr. techn. Felix Gausch (Universität Paderborn) for his willingness to review my work and for his constructive suggestions.

I greatly appreciate and am thankful to Dr. Markus Reichhartinger for his invaluable suggestions and for the numerous discussions that inspired a lot of the work documented in this thesis.

I gratefully acknowledge the financial and technical support from the company Bernecker & Rainer in Salzburg which made this work possible.

I also take this opportunity to express thankfulness and gratefulness to Em.Univ.-Prof. Dipl.-Ing. Dr.techn. Nicolaos Dourdoumas, for inspiring and encouraging me in bettering myself both personally and professionally.

I really appreciate the amiable atmosphere – both at CMS and IRT – thanks to the friendly colleagues whom I would forever be thankful for pushing me to improve my German speaking ability.

Last but not the least, my family: I express my profound gratitude to my parents – Mallikarjuna Rao and Lakshmi – for providing me with unconditional support, continuous encouragement and for imbibing in me the moral and social values that made me what I am today. A big thanks goes to Rakee and Soujanya for their trust and understanding. At the end I would like to express appreciation to my beloved wife Madhu for her patience, sincere love and support.

Vamsi Prakash Makkapati, 24-05-2016 Graz.

Nomenclature

Only frequently used symbols are given here.

Physical quantities

Symbol	Definition	Units
J_M	Moment of inertia of the motor	kg.m^2
J_L	Moment of inertia of the load	kg.m^2
d	Torsional damping coefficient of the shaft	N.m.s/rad
k	Torsional stiffness of the shaft	N.m/rad
ω_r	Angular resonance frequency	rad/s
ω_{ar}	Angular anti-resonance frequency	rad/s
f_r	$= \omega_r/2\pi$, Resonance frequency	Hz
f_{ar}	$= \omega_{ar}/2\pi$, Anti-resonance frequency	Hz
r	$= J_M/(J_M + J_L)$, inertial ratio	-
T	Torque	N.m
φ_M	Angular position of the motor	rad
φ_L	Angular position of the load	rad
R	Resistance	ohms (Ω)
L	Inductance	H
v	Gear ratio	-
fr_c	Coulomb friction	N.m
fr_v	Viscous friction	N.m.s./rad
k_t	Torque constant of the motor	N.m/A

State variables and other signals

Symbol	Definition	Units
$\Delta\varphi$	$= \varphi_M - \varphi_L$, difference in angular positions	rad
ω_M	Angular velocity of the motor	rad/s
ω_L	Angular velocity of the load	rad/s
i_q	Quadrature component of the motor current	A
i_d	Direct component of the motor current	A
U	Voltage	V
i_M	Current passing through the DC motor	A

General symbols describing a system

$\mathbf{A}$	System matrix
$\mathbf{b}, \mathbf{B}$	Input vector, -matrix
$\mathbf{c}$	Output vector
e	Control error
G	Transfer function
L	Open-loop transfer function
P	Polynomial in frequency domain
γ	relative degree
s	complex angular frequency
$u, \mathbf{u}$	Input signal or control input, -vector
ω_n	Natural angular frequency of a spring-mass-damper system
y	Output signal or controlled variable

Note: Bold symbols describe either vectors or matrices unless otherwise stated.

Subscripts

ar	anti-resonance
BW	Band width
C	Compliant shaft
c	command/reference profile
CF	Carrier frame
CL	closed loop
D	Denominator
d	disturbance
e	electric
EAF	Extended acceleration feedback
eq	equivalent
est	estimated
$filt$	filtered signal
L	load
M	motor
m	measured signal
max	maximum
N	Numerator
NF	Notch filter
OL	Open loop
R	Rigid shaft
r	resonance
ref	Reference input
s	shaft
T	Total inertia

Note: A comma in the subscript, for example $i_{q,r}$, represents the reference quadrature current signal and similarly $\omega_{M,m}$ represents the measured angular velocity of the motor.

Mathematical symbols

$\mathrm{adj}(\mathbf{A})$	Adjugate or adjoint of a matrix $\mathbf{A}$
$\mathbb{C}$	The set of Complex numbers
$\mathbb{C}_-$	open left-half Complex plane
$\mathbf{I}$	Identity matrix
$\mathscr{L}\{.\}$	*Laplacian*-operator
$\mathbb{R}$	The set of Real numbers
$\mathbb{R}_+$	$= \{x \in \mathbb{R} : x > 0\}$ The set of Real numbers larger than zero
s	*Laplacian* variable, $s \in \mathbb{C}$
$\mathrm{sgn}(.)$	sign of the variable
$y^{(i)}(t)$	i^{th}-derivative of $y(t)$
$\mathbb{Z}$	The set of Integers
$\forall$	for all
$\because$	because / since
$\overset{!}{=}$	the validity of this equality is to be shown
$\equiv$	Identically equal to
$\approx$	Approximately equal to
$:=$	Defined by
$\mathbf{A}^T$	Transpose of matrix $\mathbf{A}$

Abbreviations

AF	Acceleration feedback
DIO, dio	Dual inertia oscillator
DTC	Dead-time compensator
EAF	Extended acceleration feedback
GM	Gain margin
ID	Internal dynamics
LTI	Linear time-invariant system
NMP	Non-minimum phase
PM	Phase margin
RED	Robust exact differentiator
RFJ	Rotary flexible joint
SISO	Single input single output
SMC	Sliding mode control
SSC	Stable system center

List of Figures

Contents

Part I.

Background

1. Introduction

1.1. Introduction

The electrical drive technology is constantly spreading with applications in various fields of engineering. A basic electrical drive, as shown in Figure 1.1, consists mainly of an electric motor, the mechanical load and a controller. The electric motor drives the load via a mechanical coupling (usually a stiff shaft), and sensors are mounted for measuring the position and/or velocity from the motor and/or load. These measured variables are fed into the controller which includes both control laws, responsible for regulating the measured quantities, and a power converter which provides power to the motor.

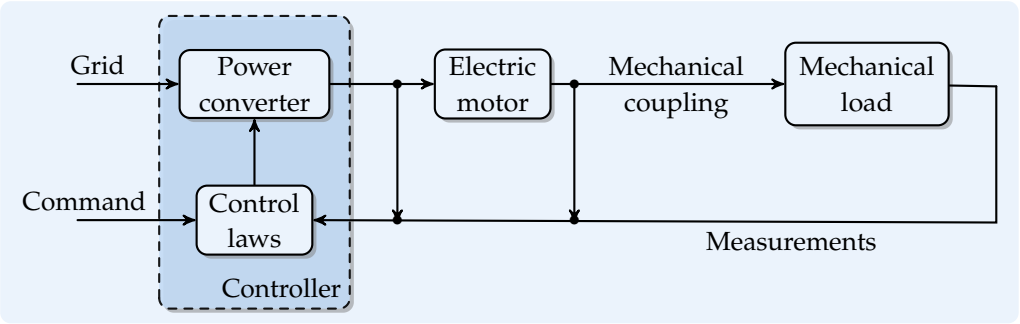

Figure 1.1.: Elements of an electrical drive system

With the improvements in power densities of electric motors, torque generation in these machines effectively became instantaneous. And with the improvements in digital electronics the control equipment has become much faster and reliable which lead to the shift in focus onto the dynamics of mechanical drivetrains which mainly depend on the shafts and couplings that are employed within these drivetrains. In many cases

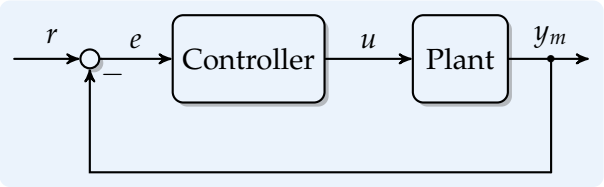

Figure 1.2.: Unity-feedback loop structure for the speed controller

these shafts are assumed to be stiff, yet in many applications, this assumption can lead to damaging oscillations due to the elasticity of the employed components. These elasticities within the drivetrain make it an oscillatory multi-mass system. Oscillations can be introduced into the drivetrain either by the motor in the form of instantaneous torque variations, for example due to a step change in the reference signal or by an external disturbance. If the damping coefficient is small enough, the amplitude of these oscillations becomes very large when their frequency closely matches with the natural frequency of the drivetrain. This phenomenon is the well-known *mechanical resonance*. The magnitude of these amplitude peaks, also known as *resonance peaks*, depend on the damping coefficient which depends on various physical factors like the material of the drive shaft, the friction at the bearings, etc.

The problem of position and/or velocity control for such an oscillatory multi-mass system suffering from mechanical resonance is very interesting and has been an intensive research topic for many years. One of the major goals of controller design for such oscillatory multi-mass system is to improve its dynamic response. Dynamic response describes how fast the closed-loop system (controlled system) reacts to a change in reference and/or to an external disturbance. The higher the dynamic response requirement, the higher are the instantaneous torques introduced by the controller via the motor into the drivetrain.

Consider a standard speed control loop as shown in Figure 1.2, and that the reference velocity r is changed in the form of a step function. By its nature, the step command excites the controller momentarily with all frequencies making up the *Fourier* series for the step function. Consequently, the closed loop is commanded to respond to all frequencies starting from the highest at the initiation of the step to a final steady state value after the transient. An appropriately tuned speed controller loop bandwidth will have its *gain crossover frequency*[1] well below the resonance frequency. Thus, the gain at the resonance frequency is well below unity (or $0dB$) and so the resulting transient

[1]The frequency at which the gain of the open-loop transfer function crosses $0dB$ line.

oscillations from resonance frequency will be damped satisfactorily by the controller. But, due to the mechanical properties of the system or due to the dynamic response requirements, if the resonance frequency is close to the bandwidth of the controller, the controller will not be able to damp the transient oscillations due to resonance. These sustained oscillations often within 100-300 Hz range (bandwidth of a typical speed controller) of the drive train and the inertias are perceived as an audible "humming". These high torque oscillations may decrease the life of drivetrain or ultimately lead to total mechanical failure. Thus, location of the resonance frequency/frequencies in a multi-mass oscillatory system relative to the controller bandwidth plays a crucial role on its performance.

1.2. Literature review

The ubiquitous presence of electrical drive systems in various industrial branches coupled with a continuous rise in the dynamic response, precision and reliability requirements from motion control applications led to the proposal of a multitude of solutions addressing the problem of mechanical resonance. Well known industrial applications suffering from mechanical resonance include, but are not limited to position and velocity control in paper machines [Val+05a] and rolling mills [DKT92; Par+03], electric vehicle transmission [ABP04a; AH11; Pet97], control of deep space antenna drives [Gaw07], position control of robotic manipulators [IYH05].

In spite of this variety the identified mathematical model in most of the cases can be reduced to a two- or three- inertia oscillator system. This observation lead to a lot of publications addressing the problem of speed and position control of such a two mass oscillator (dual inertia oscillator) system. Standard PI controller for such a dual inertia oscillator (DIO) using pole placement techniques to influence the damping characteristics of the system is developed in [Zha00]. Zhang et.al. conclude that the type of pole assignment strongly depends on the inertia ratio of motor to load. A self tuning PI controller based on optimization of the phase margin for a DIO system is proposed in [WS00]. These standard PI controller tuning techniques either require manual tuning of the controller or techniques requiring high computational power. A comparative study on vibration suppression in a DIO system using PI speed controller and additional feedbacks is reported in [SO07]. Hori et.al. [HSC99] proposed a disturbance observer based resonance ratio control (RRC), where the main aim is to change the ratio between the resonance and anti-resonance frequency by feeding back the estimated shaft torque

in a DIO. Katsura et.al. [KO07] uses a similar disturbance observer with a phase-lead compensator for stabilizing all the resonant modes of a multi-mass resonant system. Implementation issues and the resulting performance achieved using PI, PID, and RRC controllers with regard to both closed-loop robustness and control of the process variable of a DIO system are discussed in [Per+07].

State feedback techniques for instance based on H_∞ robust control [KSD00] and μ-synthesis framework [IIM04] have been designed to optimize the performance for guaranteed robust stability. These techniques are computationally demanding and require extensive knowledge for designing the required weights. Kalman filter based shaft torque estimation and consequent feedback of this estimated torque to damp the oscillations in the torque controller of a vehicle drive train is proposed in [ABP04b]. Nonlinear extended Kalman filter is used by Szabat et.al. [SO06] to estimate the shaft torque and load side speed which are used as additional feedbacks for damping the torsional vibrations in a DIO system. A LQ based speed controller using Kalman filter is reported in [JS95]. A torque controller based on sliding mode techniques for both estimation of the shaft torque and control is reported in [AH11]. Model predictive controller based suppression of torsional oscillations in a steel rolling mill is proposed in [Wan+06]. Examining the myriad of proposed solutions it becomes clear that choosing any particular approach for a given problem depends on various factors: formulation of the goal, availability of various signals for measurement, computational effort and ease of deployment and/or tuning.

1.3. Thesis objective and contribution

The main focus of this work is to improve the robustness of an existing speed controller (in a printing testbench) with respect to torsional resonance. The rear axle of the printing testbench described in Section 2.3.1 is modeled as a dual-inertia oscillator. Major constraints for controller design in this particular application are the availability of measurement signals (only motor velocity is measurable) and limited computational power. Figure 1.3 shows the measured open-loop frequency response[2], between the electrical torque input to the actuating motor (see Figure 2.9) and the measured motor velocity (from the rear axle of the) of the testbench, against the calculated response from an identified mathematical model representing a DIO with output delay. Also shown in

[2]Refer to 2.3.2 and 2.3.3 for details regarding the experimental set-up used to measure the frequency response.

green is the response of the same identified DIO model but without the output delay and without the shaft (torsional) compliance, i.e. having a rigid shaft with infinite stiffness. It is evident from the plot that the gains of the system with compliance (shown in red) are increased around and after a certain frequency called the *resonance frequency* f_r. This is due to the well known mechanical resonance phenomenon. Considering a proportional speed controller with unity gain, the measured frequency response plot shown in Figure 1.3 can be also be interpreted as the open loop bode plot for the speed control loop. Magnitude of the resonance frequency relative to that of the *phase crossover frequency* (the frequency at which the open loop has a phase shift of $-180°$, represented as f_{pc} in Figure 1.3) determines how the resonance affects the performance of the speed controller. Within this work the so called *low-frequency resonance* is considered where the resonance frequency is smaller than the first phase crossover frequency.

Using the bode plot from Figure 1.3, the stability of the speed control loop with respect to changes in the controller gain can be assessed using the concept of *gain margin*[3]. Gain margin is the distance expressed in dB between the gain of the open loop transfer

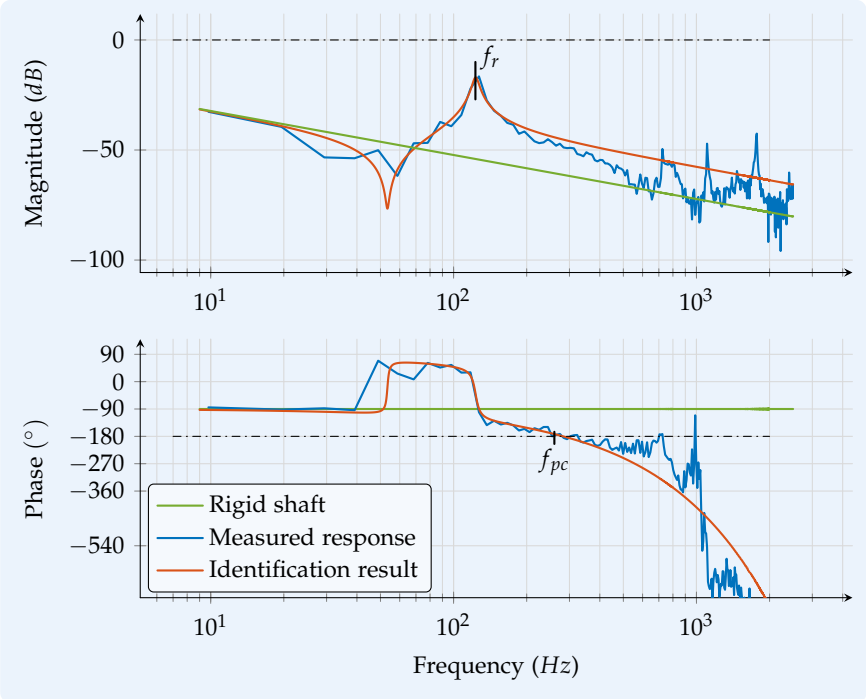

Figure 1.3.: Experimental frequency response of a DIO

[3]Refer to Appendix A.

function at the phase crossover frequency and the $0\,dB$ line. Gain margin is a measure of how much the open loop gain (controller gain + plant gain) can be increased before the stability limit is reached. If the open loop gain is increased beyond this critical gain, the closed loop transfer function is no more BIBO-stable implying that the internal stability of the control loop is lost. Thus, in theory if an open loop transfer function has a gain margin of $-G\ dB$, then the loop gain could be safely increased by a factor of $10^{G/20}$ before the system becomes unstable. But in practice, the loop gains are increased only until the open loop has a safety gain margin of $-G_{sm}\ dB$, ensuring that any unmodeled/neglected dynamics of the plant and/or controller will not render the closed loop unstable. Thus the amount of practical gain margin for any given control loop is $(G_{sm} - G)\ dB$.

Compared to the frequency response of open loop comprising a plant without compliance (see Figure 1.3), the gain margin of the one with compliance is reduced significantly. This lost gain margin significantly decreases the maximum allowed (considering the safety margin as mentioned above) loop gain, thus severely limiting its closed loop performance. The main aim of this thesis is to gain back a portion of the gain margin lost due to the compliance. As a consequence the loop gain of an existing speed controller can be increased without impacting its closed loop stability (Safety) margins. The improved loop gain will ultimately result in improving the dynamic (step- as well as disturbance) response of the speed control.

Towards this goal a technique called the acceleration feedback (AF) is employed. Acceleration feedback works by effectively increasing the moment of inertia of the motor, thereby reducing the drive's sensitivity to mechanical resonance. However the performance improvement achievable with this technique is limited due to the presence of dead time in the speed control loop. An extended version of this approach based on loop-shaping techniques is proposed in this work and is verified both in simulation and with experiments on the printing testbench.

A major contributor to the phase lag of the open-loop transfer function at higher frequencies is the dead-time present in the speed control loop. This dead time is the sum of dead times from various sources like the computational delay, sampling delay, communication delay and various other filters that are used to damp high frequency components in the speed signal. The additional phase lag due to dead time will result in gain margin limitation of the speed control loop. This observation motivated the work on techniques to mitigate the dead time. Use of a Smith-predictor for mitigating the dead-time and ideas of incorporating a rational approximation of the dead-time in

the plant model for the purpose of controller design are analyzed. Stability of these dead-time mitigation techniques with respect to the uncertainties in plant model are also considered. For practical experiments, a technique based on the output tracking for a non-minimum phase system, the so-called stable system center technique is used. The DIO plant is represented as a non-minimum phase plant by considering a Padé approximation for the dead time. Output tracking problem of this non-minimum phase plant is reformulated as a state tracking problem with the use of stable system center approach. A sliding mode controller, because of its robustness property, is used for state tracking. Both numerical and experimental results on a Quanser rotary flexible joint test set-up are reported.

1.4. Structure of this thesis

This document is organized as follows: Chapter 2 starts by summarizing the theory and modeling aspects of the DIO system and closes with a concrete description of the problem. Also described in this chapter are the experimental set-ups used in this work along with their parameter identification results. Chapter 3 presents theoretical analysis of Acceleration Feedback (AF), practical issues concerning the implementation of AF on the printing testbench and the results of implementation. Chapter 4 describes the practical limitations of AF and proposes a technique to extend the AF technique. Chapter 6 starts by representing a DIO as a Non-minimum phase (NMP) system and gives theoretical details regarding the problem of output tracking for such an NMP system. A technique namely, Stable system center approach used for output tracking of an NMP system is introduced. Practical issues and results of implementing this technique on a DIO are presented in Chapter 7. Finally, Chapter 8 gives an outlook and concludes the thesis.

2. Plant Modeling and Analysis

2.1. Mathematical modeling

The class of mechanical systems considered in this work is the so-called Dual-inertia oscillator (DIO), also known as Dual mass oscillator. A schematic of such a dual inertial oscillator is shown in Figure 2.1. The system consists of a motor with moment of inertia equal to J_M driving a load of inertia J_L through a mass-less elastic shaft with stiffness k and a torsional damping coefficient of d. The input to the DIO is the electrical torque T_e, and a disturbance torque equal to T_d acts on the load side. Total torque transmitted by the compliant torsional shaft is denoted by T_s. The angular position and angular velocities on the motor and load side are respectively denoted by φ_M, φ_L, and ω_M, ω_L. Such elastically coupled systems eliminate the use of gearboxes, belts or chains to drive

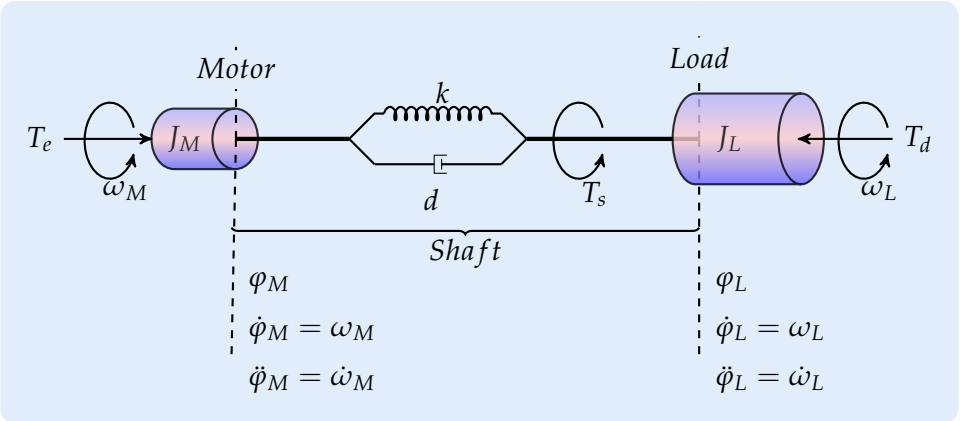

Figure 2.1.: Schematic of the two mass oscillator

the load. This results in increased efficiency, reduced noise, precise positioning, absence

of backlash and also increased longevity of the machines. DIO systems are quite often found in various fields, for example the drive line of an automobile, steel rolling mills, paper production machines, printing machines, etc.

In order to derive a mathematical model for the DIO system, shown in Figure 2.1, the following assumptions are made

- the friction at the bearings is negligible and
- the elastic shaft behaves linearly.

Total torque transmitted by the shaft is given as

$$T_s = k\left(\varphi_M - \varphi_L\right) + d\left(\omega_M - \omega_L\right). \tag{2.1}$$

Torque responsible for the acceleration on motor side, represented by T_M, is given as

$$T_M = T_e - T_s \implies J_M \ddot{\varphi}_M = T_e - k\left(\varphi_M - \varphi_L\right) - d\left(\omega_M - \omega_L\right), \tag{2.2}$$

and the accelerating torque on the load side, represented by T_L, is given as

$$T_L = T_s - T_d \implies J_L \ddot{\varphi}_L = k\left(\varphi_M - \varphi_L\right) + d\left(\omega_M - \omega_L\right) - T_d. \tag{2.3}$$

With the help of Equations (2.1) to (2.3) the signal flow diagram [Scho9] for the DIO system is sketched in Figure 2.2. Torque from the electric motor T_e is the input to the

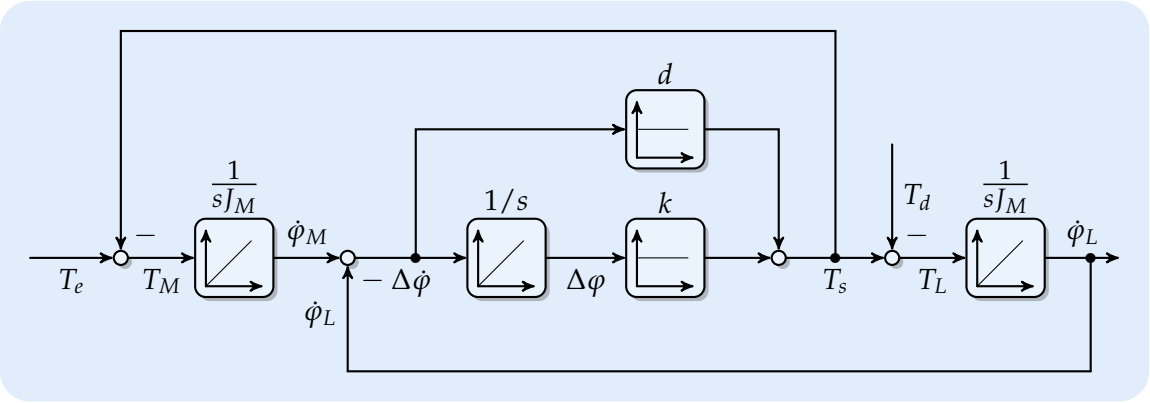

Figure 2.2.: Signal flow diagram for a dual inertia oscillator

system and ω_M, ω_L are the measurable outputs. It can be seen from the signal flow diagram that the system consists of three integrator elements, resulting in a state-space

representation of order three. The three state variables are $\dot{\varphi}_M$, $\Delta\varphi$ and $\dot{\varphi}_L$. T_e represent the manipulated variable and T_d the disturbance variable. With the help of Equations (2.1) to (2.3), the following state equations are written

$$\ddot{\varphi}_M = \frac{1}{J_M} T_e - \frac{k}{J_M}\Delta\varphi - \frac{d}{J_M}\dot{\varphi}_M + \frac{d}{J_M}\dot{\varphi}_L \tag{2.4}$$

$$\Delta\dot{\varphi} = \dot{\varphi}_M - \dot{\varphi}_L \tag{2.5}$$

$$\ddot{\varphi}_L = \frac{k}{J_L}\Delta\varphi + \frac{d}{J_L}\dot{\varphi}_M - \frac{d}{J_L}\dot{\varphi}_L + \frac{1}{J_L} T_d. \tag{2.6}$$

The matrix representation of these state-variable equations is given in Equation (2.7).

$$\begin{pmatrix} \ddot{\varphi}_M \\ \Delta\dot{\varphi} \\ \ddot{\varphi}_L \end{pmatrix} = \begin{pmatrix} -\frac{d}{J_M} & -\frac{k}{J_M} & \frac{d}{J_M} \\ 1 & 0 & -1 \\ \frac{d}{J_L} & \frac{k}{J_L} & -\frac{d}{J_L} \end{pmatrix} \cdot \begin{pmatrix} \dot{\varphi}_M \\ \Delta\varphi \\ \dot{\varphi}_L \end{pmatrix} + \begin{pmatrix} \frac{1}{J_M} \\ 0 \\ 0 \end{pmatrix} \cdot T_e + \begin{pmatrix} 0 \\ 0 \\ \frac{1}{J_L} \end{pmatrix} \cdot T_d \tag{2.7}$$

$$\dot{\mathbf{x}} = \mathbf{A} \cdot \mathbf{x} + \mathbf{b} \cdot u + \mathbf{w} \cdot v$$

2.1.1. Analysis of the model from a system theory perspective

In the present work only ω_M is considered to be measurable. The transfer function between output ω_M and the input T_e is derived as

$$G_{dio}(s) = \frac{\mathscr{L}\{\omega_M\}}{\mathscr{L}\{T_e\}} = \underbrace{\frac{1}{(J_M + J_L)s}}_{G_R(s)} \underbrace{\frac{J_L s^2 + ds + k}{\left(\frac{J_M J_L}{J_M + J_L}\right) s^2 + ds + k}}_{G_C(s)}. \tag{2.8}$$

The first fraction in Equation (2.8) denoted by $G_R(s)$ represents a rigidly connected system i.e., when the motor is rigidly connected with the load. This rigidly connected system is represented by a scaled integrator. The second fraction denoted by $G_C(s)$ represents the effect of the compliant shaft. In order to analyze this fraction its numerator and denominator are compared to a standard second-order polynomial

$$P(s) = s^2 + 2\vartheta\omega_n s + \omega_n^2, \tag{2.9}$$

where ω_n is the natural frequency and ϑ the damping ratio. The characteristic frequencies of the numerator and denominator represented by $\omega_{n,N}$ and $\omega_{n,D}$ respectively are given

as

$$\omega_{n,N} = \sqrt{\frac{k}{J_L}} \text{ rad/s} \qquad \omega_{n,D} = \sqrt{\frac{k\,(J_M + J_L)}{J_M J_L}} \text{ rad/s}. \tag{2.10}$$

To investigate the frequency response of the transfer function given by Equation (2.8), first its limiting behaviour at very low frequencies and at very high frequencies is considered.
At low frequencies, i.e. $s \to 0$:

$$G_{dio}(s) \approx \frac{1}{s\,(J_M + J_L)} = \frac{1}{sJ_t}, \tag{2.11}$$

where J_T represents the total inertia, i.e. $J_T = J_M + J_L$. Equation (2.11) is same as that of the fraction $G_R(s)$ in Equation (2.8), implying that the low frequency behaviour of the DIO system is same as that of a rigidly connected system.

At higher frequencies, i.e. $s \to \infty$:

$$G_{dio}(s) \approx \frac{1}{s\,(J_M + J_L)} \frac{J_L}{\frac{J_M J_L}{J_M + J_L}} = \frac{1}{sJ_M}. \tag{2.12}$$

At high frequencies the effective inertia is contributed solely by the motor as can be seen from Equation (2.12). This can be physically envisioned by considering the fact that the reaction of the load via the elastic shaft on the motor is always delayed.
Now in order to investigate the frequency response behaviour around the frequencies $\omega_{n,N}$, $\omega_{n,D}$, the following inertia ratio is introduced

$$r = \frac{J_M}{J_M + J_L} = \frac{J_M}{J_T} < 1. \tag{2.13}$$

Using Equation (2.13), Equation (2.10) is rewritten as

$$\omega_{n,N} = \sqrt{\frac{k}{(1-r)\,J_T}} \qquad \omega_{n,D} = \sqrt{\frac{k}{r\,(1-r)\,J_T}}. \tag{2.14}$$

From Equation (2.14) and the fact that $r < 1$ it follows that $\forall (k, J_M, J_L) \in \mathbb{R}_+$, $\omega_{n,N} < \omega_{n,D}$ and the ratio of natural frequencies is given as

$$\frac{\omega_{n,N}}{\omega_{n,D}} = \sqrt{r}. \tag{2.15}$$

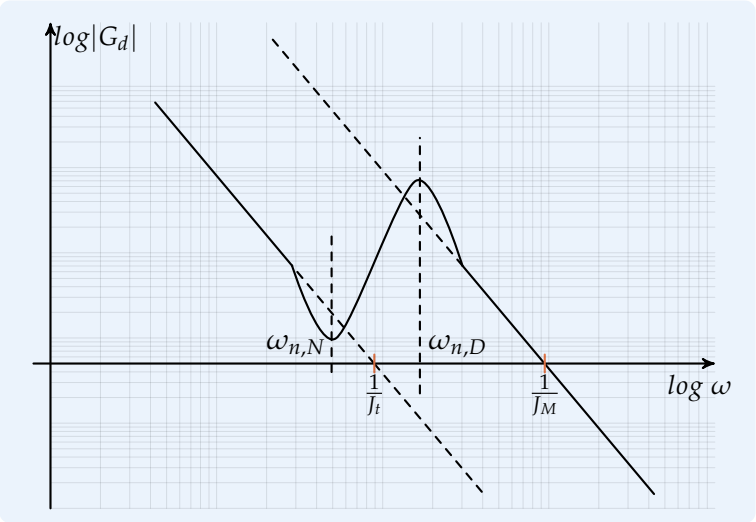

Figure 2.3.: Schematic sketch of the amplitude response of a dual inertia oscillator

Using Equations (2.10) till (2.12) a schematic sketch for the amplitude response of transfer function in Equation (2.8) is drawn in Figure 2.3. The shape of the amplitude response around the natural frequencies of the numerator and denominators of the fraction $G_C(s)$ is regulated by the amount of damping from the corresponding polynomial. At and around the natural frequency of the numerator polynomial the magnitude is reduced and similarly, at and around the natural frequency of the denominator the magnitude is increased. Similar to the amplitude response, due to the integral behaviour of Equation (2.11) phase of $G_{dio}(s)$ is -90° at low frequencies and increases first ($\because \omega_{n,N} < \omega_{n,D}$) due to the numerator term and decreases afterwards due to the denominator and finally goes back to -90° at high-frequencies due to Equation (2.12). Based on the behaviour of magnitude around the natural frequencies, given by Equation (2.10), these frequencies are given the names Anti-Resonance f_{ar} and Resonance f_r frequencies respectively. These frequencies in Hz are given as

$$f_{ar} = \frac{1}{2\pi}\sqrt{\frac{k}{J_L}}Hz \tag{2.16}$$

$$f_r = \frac{1}{2\pi}\sqrt{\frac{k\,(J_M + J_L)}{J_M J_L}}Hz. \tag{2.17}$$

Figure 2.4 shows the bode plot of a transfer function given by Equation (2.8) with different values for the inertia ratio r given by Equation (2.13). The higher the inertia ration r, i.e. the greater the inertia of motor compared to the total inertia, the lower

is the resonance frequency. This relation between motor inertia J_M and the resonance frequency f_r can also be seen from Equation (2.17); when $J_L >> J_M$,

$$f_r \approx \frac{1}{2\pi}\sqrt{\frac{k}{J_M}}. \tag{2.18}$$

In many practical applications there is always a small dead time around the control loop. This dead time is the result of the combination of several factors. Due to the fact that the controllers are implemented on a digital microprocessor, sampling process is inevitable. In addition to the inherent delay from sampling and calculation processes, there is the velocity calculation delay in motion control applications. Usually in motion control applications the position is measured and the velocity is calculated as the difference of the two most recent positions. Depending on the quality of the position measurement additional signal processing is done on the calculated velocity signal which will also add some delay. This dead time can be represented as an exponential function in *Laplacian* domain as shown in Equation (5.2). Taking these dead times into account the DIO system

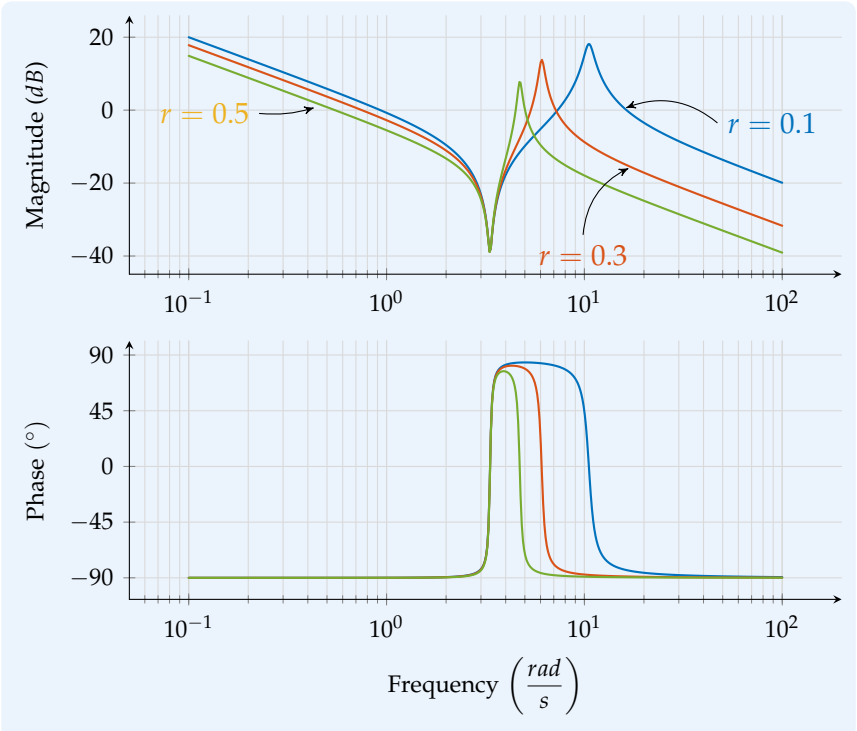

Figure 2.4.: Bode plot of $G_{dio}(s)$ with different inertia ratios.

represented by Equation (2.8) is modified as

$$G_t(s) = G_{dio}(s) \cdot e^{-\tau s}, \tag{2.19}$$

where τ is the dead time around the loop in seconds. Figure 2.5 shows the effect of the dead time on the frequency response of a DIO system. A detailed description of the affects of dead time on the stability of close-loop are given in Section 5.2.

The following facts support the assumption made at the beginning of this section that only the motor angular velocity is measurable.

- A transfer function between T_e and ω_L is given as

$$G_{dL}(s) = \frac{\omega_L(s)}{T_e(s)} = \frac{1}{(J_M + J_L)s} \frac{ds + k}{\left(\frac{J_M J_L}{J_M + J_L}\right) s^2 + ds + k}. \tag{2.20}$$

  Due to the missing s^2 term in the numerator (compared to Equation (2.8)), the

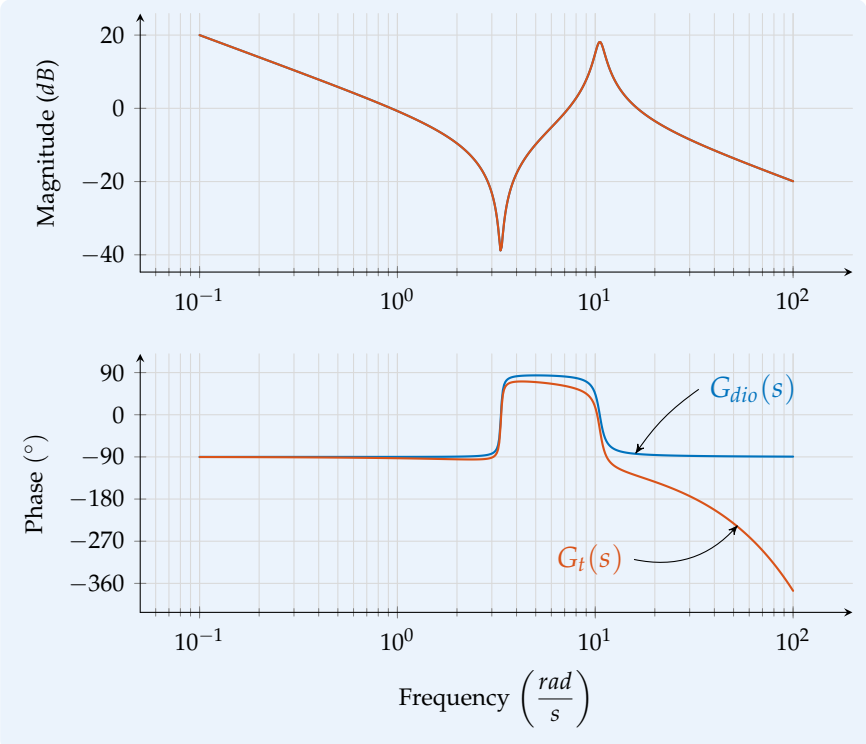

Figure 2.5.: Bode plot of $G_{dio}(s)$ and $G_t(s)$

phase goes below -180° which makes it much more hard to control the plant with ω_L as the measured output.

- One encoder on the motor is always required for controlling the motor and an additional encoder on the load side increases the associated costs.

2.2. Problem description

Example 2.2.1 (Motivating example)**.** Consider the problem of calculating a speed controller for a DIO described by Equations (2.4) to (2.6). The unity-feedback loop shown in Figure 2.6 is considered for this purpose. For the sake of analysis

- the controller is assumed to be a proportional controller with gain k_p, and
- dynamics of the current controller and the power inverter, which are essential for real world implementation (see Section 2.3.2), are neglected assuming that their dynamics are sufficiently faster than that of DIO.

In Figure 2.6, $\omega_{M,r}$ represents the reference angular velocity of the motor and y_m represents the measured motor angular velocity. In order to predict the closed loop dynamics of this unity-feedback system, its open-loop is studied. The open-loop or the loop transfer function, using Equation (2.8) is given as

$$L(s) = k_p G_{dio}(s) e^{-\tau s}. \tag{2.21}$$

Using the parameters in Table 2.1, the bode plot of the open-loop is drawn in Figure 2.7a and the closed loop frequency response is plotted in Figure 2.7b. It is evident from Figure 2.7 that the closed loop system is unstable based on the fact that both gain and phase margins are negative and are equal to $-2.1\,\mathrm{dB}$ and -24.6° respectively.

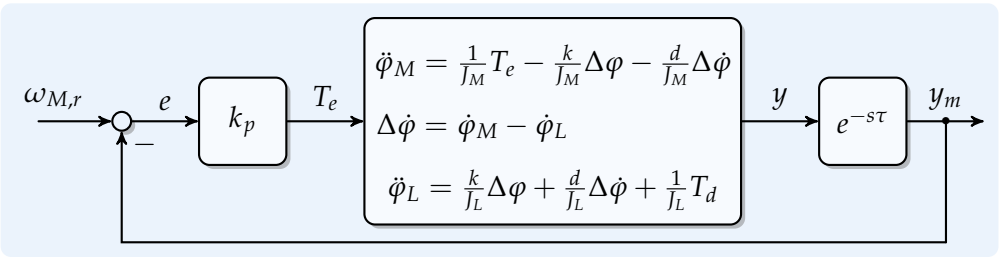

Figure 2.6.: Unity-feedback loop structure for the speed control

Table 2.1.: Simulation parameters

Parameter	Value	Units
J_M	0.1	kg.m^2
J_L	0.9	kg.m^2
d	0.1	N.m.s/rad
k	10	N.m/rad
τ	0.01	s
k_p	20	A.s

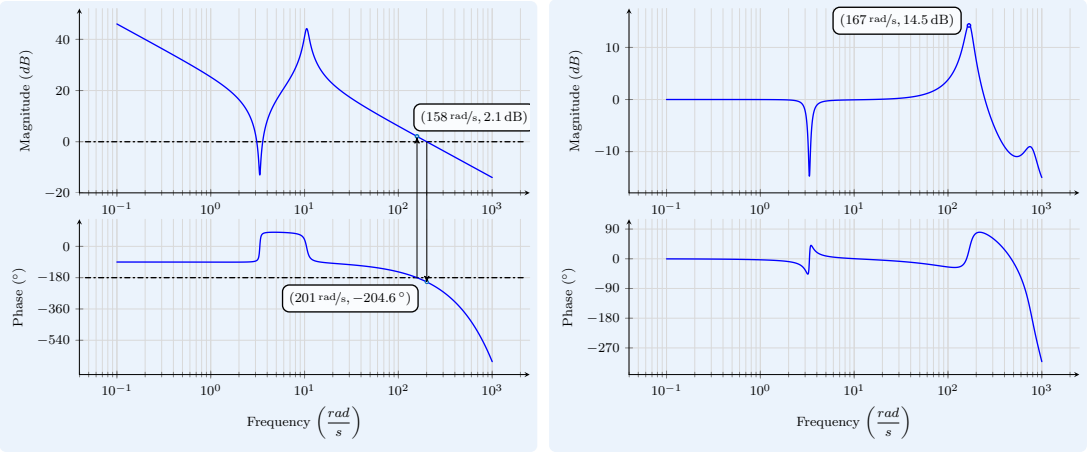

(a) Open-loop bode plot

(b) Close-loop bode plot

Figure 2.7.: Bode plot depicting the inertial-reduction instability

In order to study the influence of mechanical compliance present within the DIO on the performance of the speed controller, bode plot of the open-loop system as given by Equation (2.21) is plotted twice in Figure 2.8 once with the mechanical compliance and once without (for simplicity k_p is set to 1 in both the cases). The first curve, drawn in blue, represents the open-loop system with mechanical compliance and the second curve, drawn in red, represents the system with a rigid shaft. GM_C, GM_R represent the gain margins of the open-loop system with and without the compliant shaft. It is obvious from Figure 2.8 that $GM_C < GM_R$. Due to the increase in gain (of the DIO) around and after the resonance frequency, the gain margin of an otherwise rigidly connected motor and load is eroded. This reduction in gain margin ultimately affects the closed loop performance (by reducing the maximum achievable gain of the controller before

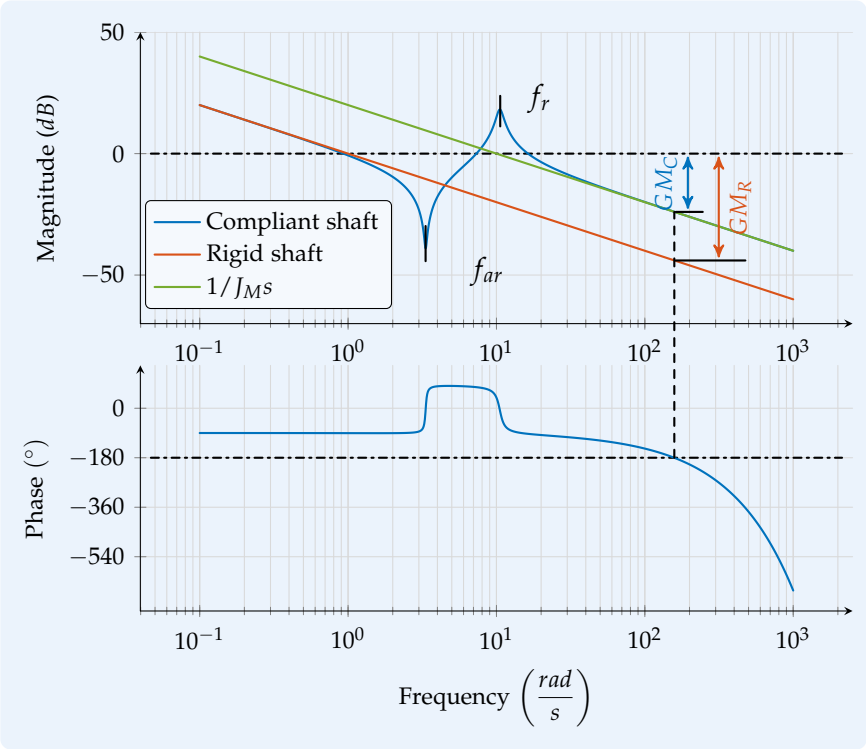

Figure 2.8.: Plot depicting the erosion of gain margin due to the elastic shaft

the closed loop is rendered unstable). ▲

Mechanical compliance can generate instability in two ways: *tuned resonance* and *inertial-reduction instability* [Ello4]. With tuned resonance (also known as high-frequency resonance), the system oscillates at the resonant frequency of the combined motor and load; the motor and load oscillate at that frequency, moving in opposite directions as energy circulates between the two. A common characteristic of tuned resonance is that the resonance frequency is often above the first phase crossover frequency. Machines that most often demonstrate tuned resonance are those with low cross-coupled viscous damping. The system often oscillates with frequencies over a narrow band around the resonance frequency resulting in a pure pitch, sounding much like a tuning fork. The frequency of oscillation is mechanically fixed, and changing controller gains may change the intensity of the oscillations but not the pitch.

With inertial-reduction instability (sometimes also known as low-frequency resonance), the system becomes unstable above the motor-load resonant frequency. Here the flexible

coupling essentially disconnects the load from the motor. Figure 2.8 plots the bode plot of the DIO together with lines representing the rigidly connected DIO and of the motor only (represented by red and brown lines respectively). At low frequencies, the DIO with compliant shaft overlaps with rigidly connected system and at high frequencies it overlaps with that of the motor only. This can also be seen from Equations (2.11) and (2.12). A key characteristic of a system exhibiting inertial-reduction instability is that the resonance frequency is below the first phase crossover frequency, and in case instability, the system oscillated with a frequency which is above, often well above, the resonant frequency of the motor and load. This can be seen from the closed loop frequency response plot in Figure 2.7b; the frequency of oscillation (represented by the peak) is 167 rad/s where as the resonance frequency is 10 rad/s. Instability in inertial-reduction instability comes from a gain increase that occurs over a wide frequency range, not from a narrow gain spike as with tuned resonance. Thus the frequency of oscillation can occur anywhere above the resonant frequency of the motor and load, but close to the bandwidth of the speed controller.

A machine suffering with tuned resonance will usually emit a pure pitch, like a tuning fork. The frequency of the oscillation is fixed (and depends on the mechanical parameters), and changing the controllers gains only changes the intensity of the pitch, but not the pitch. Whereas in the case of inertial-reduction instability, the frequency of oscillation is influenced by the control loop gain. A little variation of the loop gain[1] is common, and any variations influences the frequency of instability through a corresponding shift. Such variations causes the frequency of oscillation to vary resulting in a distorted tone. Thus a system suffering from inertial-reduction instability makes a rough grinding noise.

The problem of instability due to inertial-reduction is considered in this work. Main goal of this work is to improve the performance of a DIO suffering from inertial-reduction instability. Two different approaches, namely acceleration feedback and output tracking of a non-minimum phase system are employed in this work. Acceleration feedback deals with the problem mentioned above by artificially increasing the motor inertia and thereby improving the gain margin. The second technique approaches the problem from a different perspective, i.e. by mitigating the dead-time and thus reducing the phase lag around the loop.

[1] for instance, current loop performance can vary because large current magnitudes can reduce rotor inductance

2.3. Printing testbench

2.3.1. Features

The printing testbench shown in figure 2.9, built in cooperation with Bernecker and Rainer Industrie-Elektronik Ges.m.b.H. [BRA] from Salzburg, is used for experiments in this work. The rear axle of the testbench consisting of the actuating motor, the elastic shaft, a load inertia and a disturbance motor behaves as a DIO.

Main aim behind the development of this printing testbench is to simulate various problems with printing machines in a laboratory environment. An annotated CAD drawing of its top-view highlighting important components is shown in Figure 2.10. The motor on the top left drives the counter-pressure cylinder via an elastic shaft. This shaft is connected to the motor on one side and the cylinder on the other with the help of rigid couplings. There is an additional motor on the right side of the counter-pressure cylinder which can be used to simulate disturbance torques. The disturbance motor and the counter-pressure cylinder are joined using a bellow coupling, which is used to compensate for any axial misalignment. A second larger cylinder the so-called print cylinder is driven by another motor, and this whole axis is mounted on a pivot-able

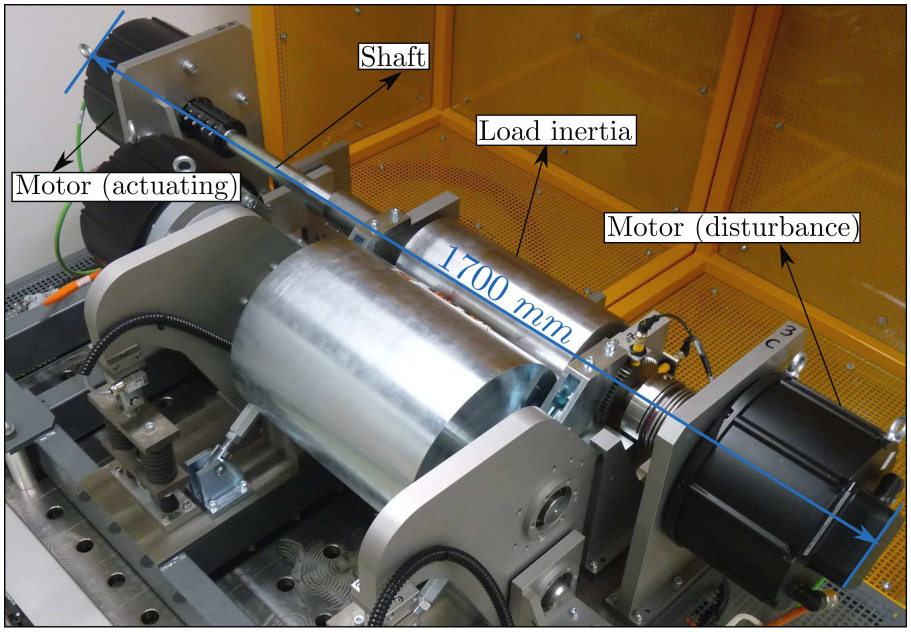

Figure 2.9.: Printing testbench

arm as can be seen from Figure 2.11. This pivot-able arm is connected to the base plate via a spring mounted load-cell enabling the measurement of contact force between

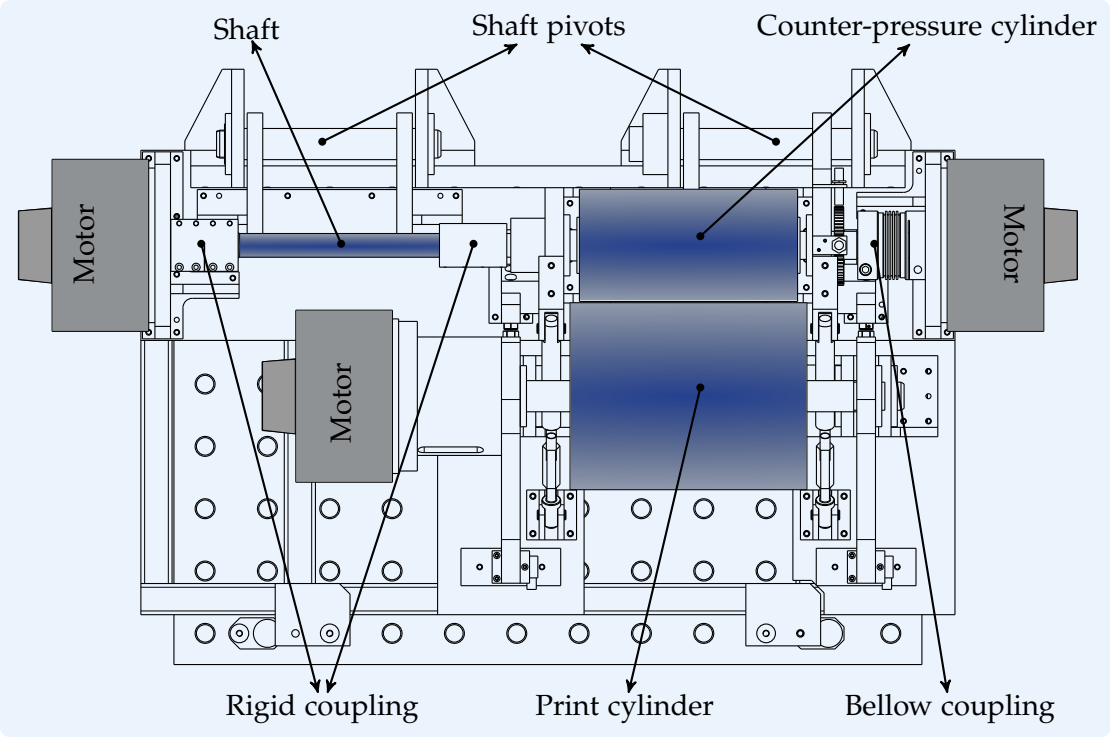

Figure 2.10.: Printing testbench; Top view

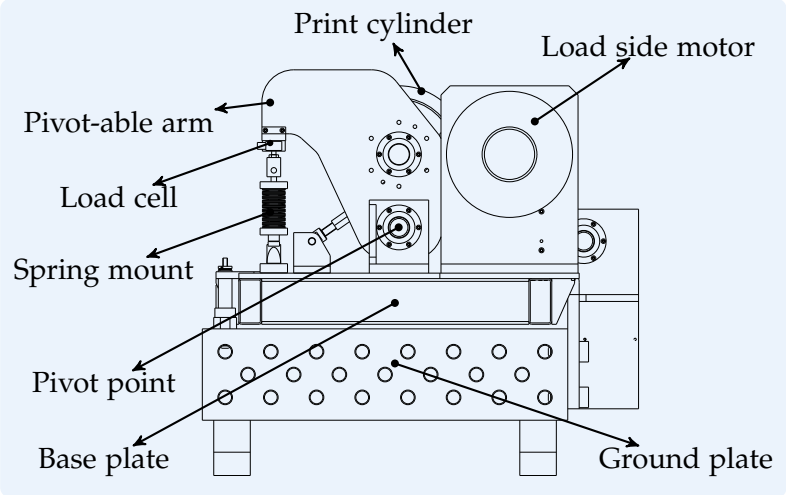

Figure 2.11.: Printing testbench; Side view

the two cylinders. The printing process is described with the help of Figure 2.12. The print cylinder is wrapped with a rubber cliché which carries the impression to be printed onto the paper, and the paper itself is fed between the cylinders. The pressure between the two cylinders is used to transfer the ink onto the paper. An optimal pressure has to be maintained in order to ensure a consistent print quality. Often the rubber cliché is not long enough to cover the entire circumference of the print cylinder resulting in uneven contact force between the cylinders during operation, which ultimately introduces vibrations into the base plate.

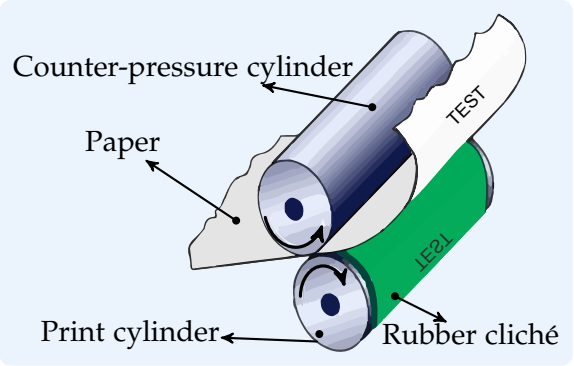

Figure 2.12.: Illustration of the printing process

It can be seen from Figure 2.11 and Figure 2.10 that the whole machine rests on a pivot-able base plate which is connected to the ground plate via a couple of shaft pivots. Carefully placed encoders at these pivot points enables the measurement of the relative movement between the base and ground plates. This feature enables the testbench to simulate the vibrational behaviour of a pick-and-place robot. A pick-and-place robot introduces vibrations into its base due to the rapid start and stop moves between two given points in space. If the rear axle of the machine is rapidly positioned back and forth between two points, it introduces torsional oscillations in the elastic shaft which ultimately introduce vibrations in the base plate.

2.3.2. Motor controller

All the three motors used in the testbench are three phase permanent magnet synchronous motors (PMSM) with a rated torque of 39 Nm and a rated speed of 1000 rpm. These motors are driven with ACOPOSmulti [ACO], a servo drive from B&R, which mainly consist of

- EnDAT[int] interface for communicating with the motor encoder
- motion controller
- power converter.

The power converter is used as the actuator (variable frequency signal generator) which drives the PMSM. The motors are fitted with absolute encoders which are used for measuring the rotor position. This rotor position is used on one hand by the servo drive for the commutation of currents and on the other hand for the feedback control of velocity and position of the motor. The servo drive together with the driven mechanical load is often called as the servo drive axis.

An industry standard cascaded type controller, shown in Figure 2.13, is used as the motion controller on the ACOPOSmulti. A signal generator within the position controller is used to generate a reference position profile based on the current position and the target position φ_r. The signal generator also takes into account the restrictions on the maximum acceleration and velocities of the motor while calculating the reference profile. This reference profile is compared against the measured position φ_m by the position controller to generate the reference velocity ω_r. Also within the position controller is a filter that calculates the current velocity ω_m from the measured position. The position controller task runs every 400 µs, i.e. with a frequency of 2.5 kHz. The measured velocity along with the reference velocity are processed by the velocity controller running every 200 µs or at 5 kHz to calculate the reference quadrature current $i_{q,r}$.

The machine is normally operated in constant torque mode where the direct-axis current i_d is set to zero, and only the quadrature-axis current i_q is responsible for the torque production [Krio1]. This torque producing reference quadrature-axis current $i_{q,r}$ is calculated by the velocity controller. The aim of the current controller is make the measured current components $i_{q,m}$ and $i_{d,m}$ to correspond to the desired values ($i_{q,r}$ and $i_{d,r}$). Based on the error between the desired and the measured values current controller calculates the reference voltages $v_{q,r}$ and $v_{d,r}$ in d-q frame. The reference voltages in d-q frame are converted to the three phase voltages using Park transformations [Vuk12]. These reference voltages are realized by the switching action of power transistors in the

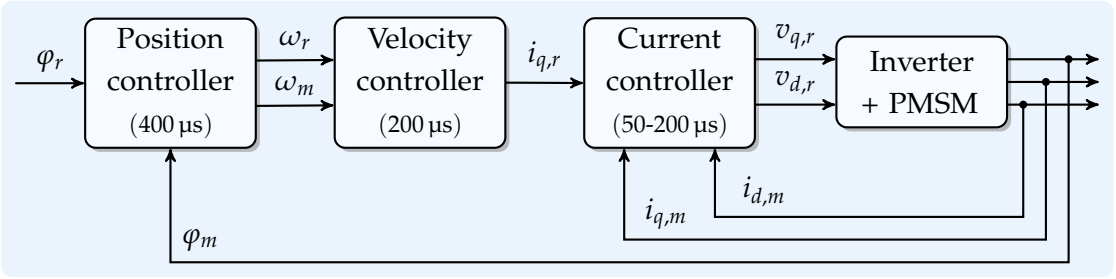

Figure 2.13.: Structure of the cascaded controller structure used in ACOPOS

inverter circuit. The operating frequency of the current controller can be set to 2.5 kHz, 5 kHz, 10 kHz or 20 kHz. The power transistors within the inverter module are switched at the same frequency as that of the current controller. It is well known that higher switching frequencies tend to dampen the magnitude of ripple in the current signal. All the experiments performed on the testbench in this work are programmed in the current controller part. So if the switching frequency is increased (by decreasing the cyclic time of the current controller task) the time available for executing the user written programs is reduced. A switching frequency of 5 kHz is used for all the experiments presented in this work.

The following three different control modes are differentiated

1. position control mode
2. speed control mode
3. torque control mode.

When a machine in running is position control mode, all the three cascaded controllers are active and are working to keep the position of the motor at a given reference value or following a given reference trajectory. In the case of speed control mode only the speed controller and the underlying current controller are actively keeping the reference velocity / velocity profile. The third case is when only the current controller is active and a reference torque is generated by the motor.

2.3.3. Parameter identification

As mentioned in Section 2.3.1, the rear axle of the printing testbench behaves as a DIO. This section presents the details regarding parameter estimation for this DIO system. Parameters that need to be estimated are the motor, load inertia, and stiffness, damping of the shaft. For identification the DIO is excited with a Pseudo-Random-Binary-Signal (PRBS) [MRH10]. The PRBS is fed into the mechanics as the torque generating component of the stator current [VPE05; WGH13]. The advantage of using PRBS signal is that it minimizes the movement due to excitation so that it is suitable also for machines with limited movement capabilities. The response of the excitation is

measured by differentiating the position signal[2] which is measured by the encoder on the motor shaft. The quantization effects from the differentiation can be neglected due to the high resolution of the encoders in industrial servo drives. A switching frequency of 5 kHz was used for the identification experiment. Figure 2.14 plots the time domain data collected from an identification experiment. The transient data is neglected from the experimental data and only the steady state measurements are used for identification. Using the time domain experimental data the frequency response data is calculated using *fast Fourier transform* (FFT) algorithm in MATLAB. This frequency domain data is used to fit a parametric model based on the transfer function given by

$$G_d(s) = \frac{\mathscr{L}\{\omega_m\}}{\mathscr{L}\{T_e(s)\}} = \frac{1}{(J_M + J_L)s} \frac{J_L s^2 + ds + k}{\left(\frac{J_M J_L}{J_M + J_L}\right) s^2 + ds + k} e^{-\tau s}, \tag{2.22}$$

where τ represents the dead-time. The transfer function in (2.22) is parametrized using J_T, f_r, f_{ar}, d, τ and the initial values for the parameters J_T, f_r and f_{ar} are estimated from

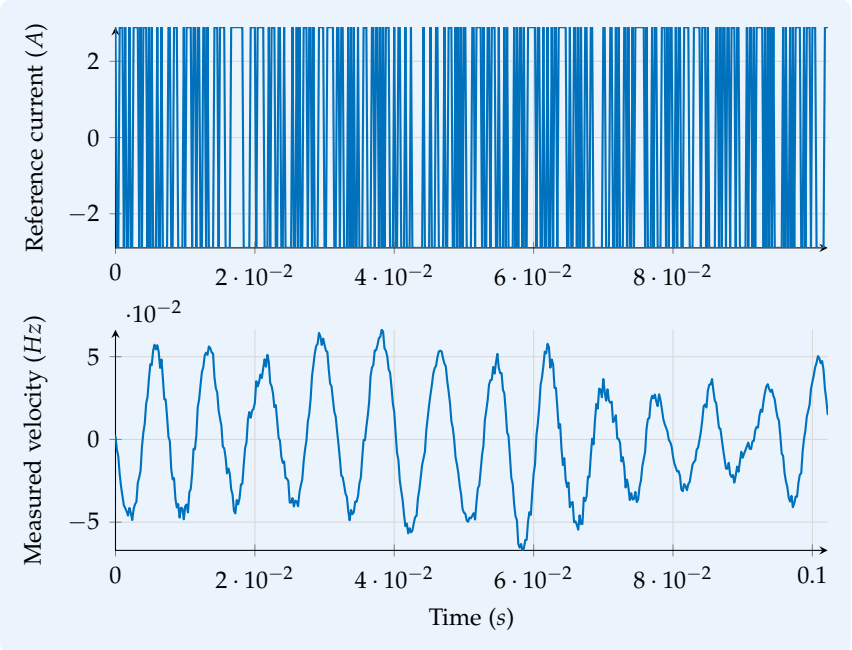

Figure 2.14.: Time domain measurements from the identification experiment

[2]The differentiation and subsequent conditioning and filtering operations on the position signal are performed in the firmware of the servo drive and only the angular velocity is available for experiments, thus the angular velocity is assumed to be measured in this work.

Table 2.2.: Estimated parameters

Parameter	Value	Units
J_M	0.0658	kg.m^2
J_L	0.2843	kg.m^2
d	2.51	N.m.s/rad
k	32.013	kN.m/rad
τ	0.001	s

the experimental data. A non linear least squares fitting technique is used to fit the model to the experimental data.

Figure 2.15 plots the frequency response of the identified model against the measured frequency response from the PRBS excitation. Number of data points in the low frequency are limited due to the limited amount of memory available on the servo drive. The high frequency content (around 1000 Hz) shows a number of secondary resonance peaks in the magnitude response. These secondary resonance peaks are formed by the

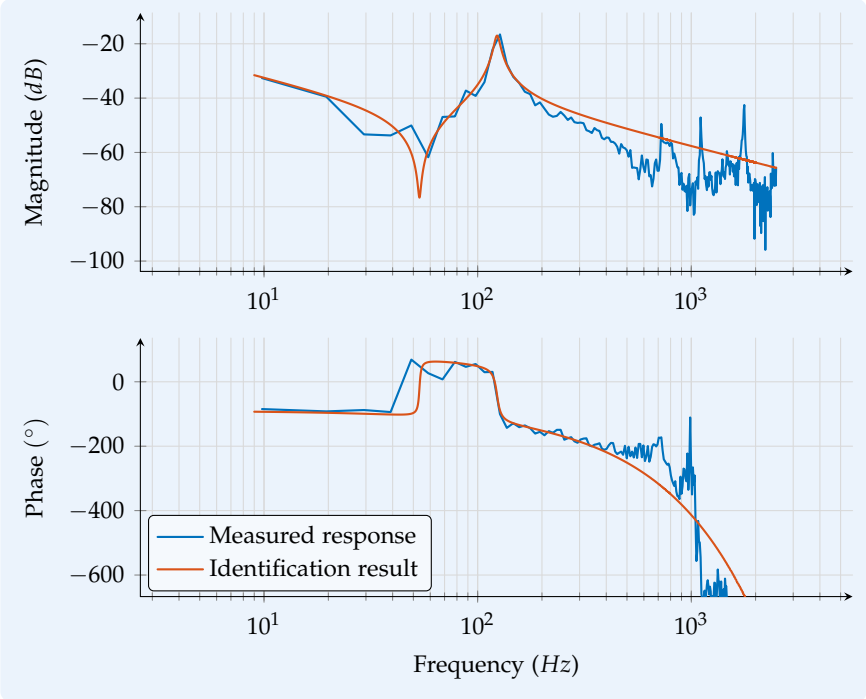

Figure 2.15.: Measured frequency response Vs. frequency response of identified model

different couplings present in the drive train connecting the load to the actuating and the disturbance motors (Refer to Figure 2.9). A higher order system considering more than two masses is required to model the behaviour of the system exactly, but for the purpose of experiments in this work only the dominant resonance frequency and the corresponding dual inertia system is modelled. The dominant resonance frequency, the damping factor effecting the magnitude of this resonance peak and the dead-time effecting the phase are satisfactorily identified. Table 2.2 lists the identified parameters.

2.4. Quanser rotary flexible joint

Figure 2.16 shows the experimental setup with the rotary flexible joint (RFJ) from Quanser [Qua]. The setup mainly consists of an aluminium frame which supports all the mechanics. A DC motor drives the carrier frame via a reduction gear. A rotary cantilever load is mounted on the carrier frame with the help of two flexible springs. Additional weights are mounted on the cantilever to increase the moment of inertia. Two encoders,

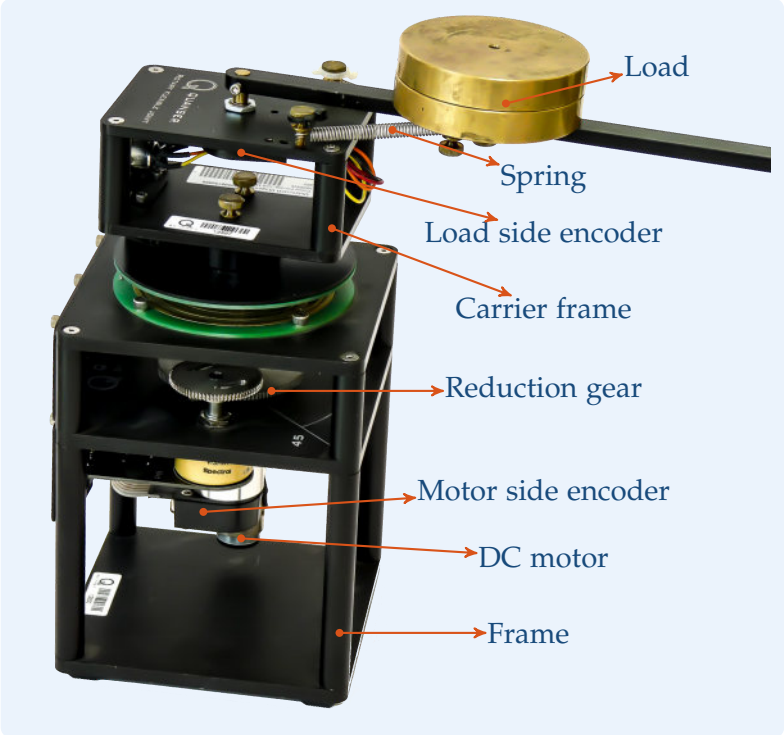

Figure 2.16.: Quanser rotary flexible joint experimental setup

one on the motor and the other on the load side, allow for the measurement of angular positions. An equivalent circuit diagram depicting both the electromagnetic subsystem and the mechanical subsystem of the RFJ setup is shown in Figure 2.17. The DC motor (with moment of inertia J_{dc} about the axis of rotation, electrical resistance R_M, inductance L_M, motor torque constant K_t, motor current i_M, input voltage U_M, rotor position φ_M and rotor velocity ω_M) drives the carrier frame via a gear box with gear ratio v. The load (with moment of inertia J_L) is connected to the carrier frame (with moment of inertia J_{CF}) via the spring with stiffness k and damping factor d. The velocities of both the motor and load are calculated using the difference between two recent position measurements. It is assumed that the shafts connecting the motor to the gears and the gears to the carrier frame are rigid, and that there is no play in the gears. Using this assumption the total inertia to the left of the spring (in Figure 2.17) can be lumped together into J_M making the dynamics of the RFJ setup similar to that of DIO.

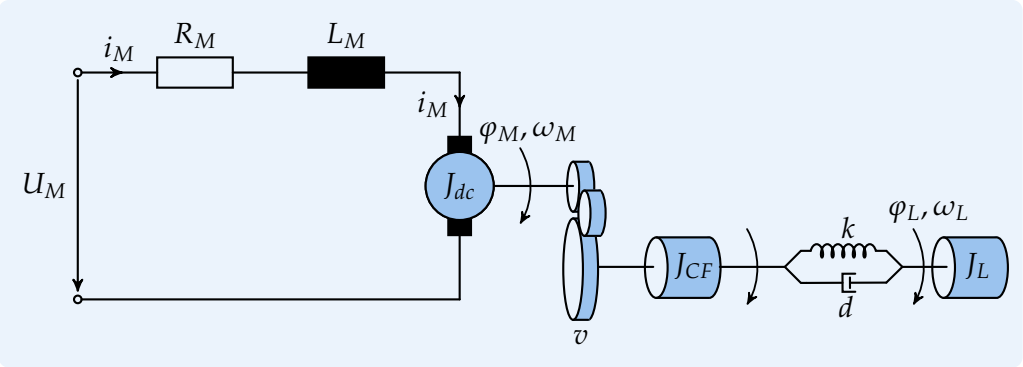

Figure 2.17.: Equivalent electromechanical circuit diagram of the Quanser RFJ setup

2.4.1. Parameter estimation

For the purpose of identification, back-EMF introduced within the DC motor is neglected. This allows the relation between the torque induced by the DC motor and the applied voltage U_M to be described by the following linear equation

$$T_e = \underbrace{\frac{K_t v}{R_M}}_{:=K_M} U_M. \tag{2.23}$$

An excitation signal in the form of T_e is generated and applied to the setup via U_M using the relation (2.23). The motor speed ω_M is calculated from the measured rotor position

φ_M. Additional low-pass filters are used as well to filter out high frequency noise from the calculated speed signals. These input and output signals are used for estimating the parameters describing the dynamics of the RFJ setup in the form of DIO. Coulomb and viscous friction components are also considered in the parameter estimation. The parameters are estimated using a recursive least square identification technique. Table 2.3 presents the estimated model parameters, fr_c, fr_v denote the Coulomb and Viscous friction coefficients. Plotted in Figure 2.18 are the input torque from the DC motor (related to the input voltage via (2.23)), the measured and simulated velocities and the error in the simulated velocity. In spite of the fact that the dynamics of the RFJ setup are approximated to that of DIO, the estimated model fits the measured data quite well as seen from Figure 2.18.

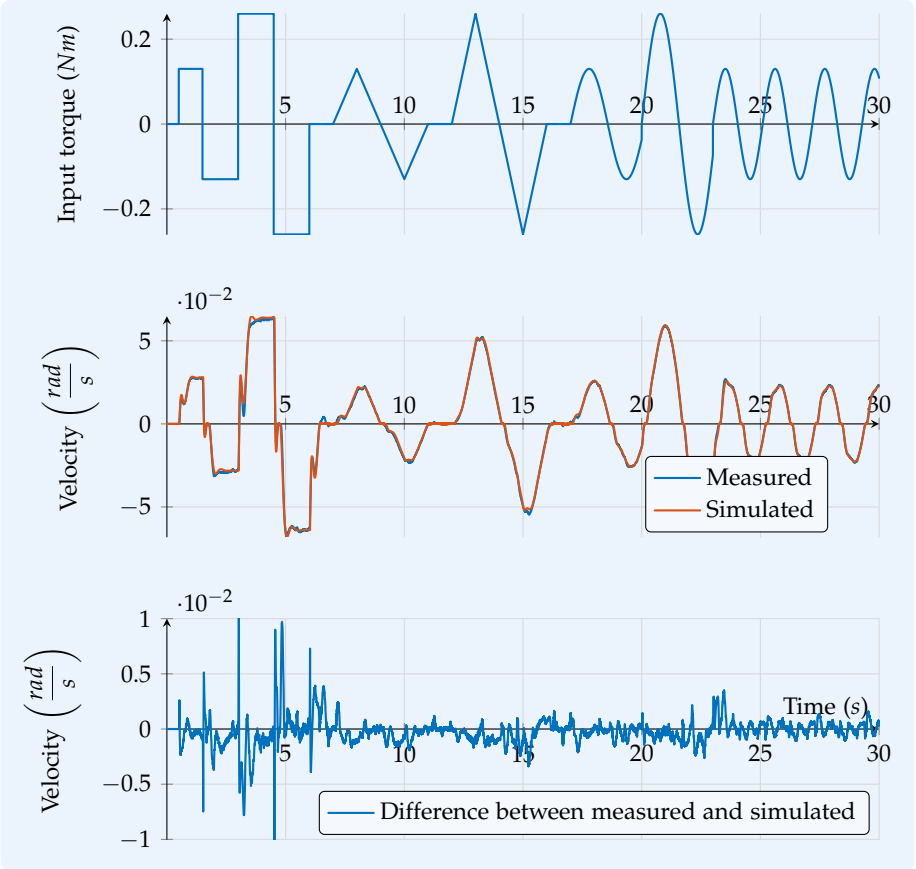

Figure 2.18.: Parameter estimation for the RFJ experimental setup

Table 2.3.: Estimated parameters

Parameter	Value	Units
J_M	0.1897	kg.m^2
J_L	0.4773	kg.m^2
d	0.3	N.m.s/rad
k	39.27	N.m/rad
τ	0.03	s
$fr_{v,M}$	3.56	N.m.s/rad
$fr_{v,L}$	0.07	N.m.s/rad
$fr_{c,M}$	0.028	N.m
$fr_{c,L}$	0.00	N.m
K_M	0.13	A.s

Part II.

Acceleration Feedback

3. Acceleration Feedback

As described in Section 2.2, elastic shaft connecting the driving motor to the driven load leads to a increase in gains around and after the resonance frequency. These increased gains erode the gain margin thus limiting the performance of a speed control loop. Following section presents some well-known cures for mechanical resonance. Motivation and the basic idea behind Acceleration Feedback (AF) technique are presented in Section 3.2. Theoretical analysis of AF supported by numerical simulations is presented in Section 3.3. Section 3.4 presents three differentiation techniques which can be used with noise corrupted measurement signal for estimating the acceleration signal. Implementation details for implementing AF on the printing testbench and the experimental results are discussed in Sections 3.5 and 3.6 respectively.

3.1. Cures for mechanical resonance

There are numerous mechanical and electrical cures for mechanical resonance described in the literature [EG01; VBL05, and references therein]. The following techniques are quite often employed

- increase motor to load inertia ratio,
- stiffen the shaft,
- electronic filters.

Increasing the motor to load inertia ratio is one of the most reliable ways of improving the resonance problem. This is because the smaller the ratio of load inertia to motor inertia, the less compliance will affect the system. The effect of this inertia ratio can be seen from Figure 2.4; the smaller the ratio of load to motor inertia, the shorter is

the distance between two parallel lines (refer Equations (2.11) and (2.12)). This in-turn reduces the amount of gain margin lost due to resonance phenomenon.

Increasing the stiffness of the elastic shaft connecting the motor to the load is another well-known technique for improving the performance of a system affected by resonance. Increasing the stiffness of the shaft will push the resonance and anti-resonance frequencies higher on the frequency axis (see Equations (2.16), (2.17)). There will be a stiffness value after which the resonance frequency is above the first phase crossover frequency, resulting in changing the system behaviour from inertial-reduction instability to a tuned resonance. Stiffness of the shafts can be increased by using stiffer materials, increasing the diameter of shaft, or by using shorter shafts [VBL05]. Adding more mechanical damping will also help. These mechanical solutions are almost always economically taxing, and in some situations may not be implementable because of design restrictions.

Electronic solutions generally make use of Notch filters [SR99], and Bi-quad filters [EG01]. The common objective for these two filters is to attenuate the loop gain at a particular frequency, thus suppressing the effects of resonance. These filters are tuned to the frequency at which the closed loop oscillates (see Figure 2.7b). These filters are rendered useless when there is a change in peaking frequency of the closed loop. As mentioned in Section 2.2 the frequency of oscillation in case of a system suffering from inertial-reduction instability is not fixed.

Another solution is the so-called acceleration feedback (AF) which increases the motor inertia electronically. It has been shown in [Val+05b] that this method is robust against variations in inertia ratio, damping and stiffness of the connecting shaft. And the fact that this technique can be applied by electronic means makes it more interesting.

3.2. Motivation

The amount of gain margin (GM) lost due to the increase in gain around and after the resonance frequency depends on the moment of inertia of the motor, as can be inferred from Figure 2.3 and Figure 2.8. In order to increase the GM it is sufficient if the moment of inertia of the motor is increased. This way the high frequency asymptote is shifted closer to the low frequency asymptote, resulting in an increased GM. The main goal behind AF is to electronically increase the inertia of the motor. Assuming that this goal

is achieved by adding an additional inertia J_a to J_M, Equation (2.4) is modified as

$$\ddot{\varphi}_M (J_M + J_a) = T_e - k(\varphi_M - \varphi_L) - d(\dot{\varphi}_M - \dot{\varphi}_L) \tag{3.1}$$

$$\implies \ddot{\varphi}_M J_M = T_e - k(\varphi_M - \varphi_L) - d(\dot{\varphi}_M - \dot{\varphi}_L) - \ddot{\varphi}_M J_a$$

$$\implies \ddot{\varphi}_M J_M = T_e - \ddot{\varphi}_M J_a - k(\varphi_M - \varphi_L) - d(\dot{\varphi}_M - \dot{\varphi}_L). \tag{3.2}$$

As seen from Equation (3.2) subtracting the signal $\ddot{\varphi}_M J_a$ from T_e results in an apparent increase in the motor moment of inertia. This additional signal is the product of motor acceleration $\ddot{\varphi}_M$, which is not directly measurable, and a constant gain J_a, which is chosen at will. Following section presents the numerical simulation of AF technique for a dual-inertia oscillator.

3.3. Numerical simulation of AF technique

Consider the velocity control loop as shown in Figure 3.1, where a proportional controller is used for tracking the reference angular velocity $\omega_{M,r}$. Acceleration feedback, as mentioned in the previous section is implemented with a gain of J_a which effectively becomes the additional (or active) inertia added to J_M.

For the sake of simplicity, acceleration signal is assumed to be available by differentiating the output velocity signal. The transfer function of the open-loop system is given as

$$\frac{y_m}{\omega_{M,r}} = k_p \frac{G_{dio}(s)}{1 + G_{dio}(s)\, J_a\, s}, \tag{3.3}$$

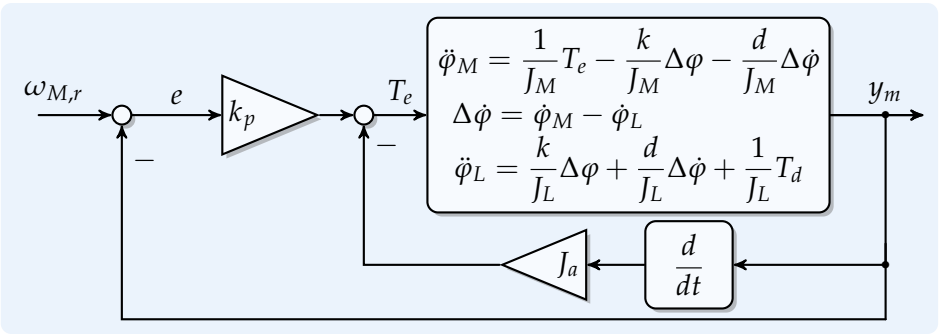

Figure 3.1.: Velocity control loop with incorporated AF loop

using Equation (2.8), the above equation is rewritten as

$$\frac{y_m}{\omega_{M,r}} = k_p \frac{1}{(J_M + J_a + J_L)s} \frac{J_L s^2 + ds + k}{\left(\frac{(J_M + J_a)J_L}{J_M + J_a + J_L}\right) s^2 + ds + k}. \tag{3.4}$$

One can see that the numerator does not change implying that the antiresonance frequency remains the same, but the resonance frequency is shifted to a lower frequency.

$$f_r = \frac{1}{2\pi} \sqrt{\frac{k(J_M + J_a + J_L)}{(J_M + J_a)\, J_L}} \tag{3.5}$$

This shift in the resonance frequency (compare Equations (2.17) and (3.5)) is also seen when the bode plot of the open loop is plotted as shown in Figure 3.2. The identified printing testbench parameters from Table 2.2 together with a proportional gain of $k_p = 1$ are used for plotting this bode diagram. It can also be seen from the figure that the magnitude peak at the resonance frequency is also damped with the use of AF. The effective increase in the motor inertia also increases the gain margin of the speed control loop.

For simulating the behaviour of AF in closed speed control loop, consider the proportional gain $k_p = 80$. Now the results of two simulations, one with $J_a = 2J_M$ and the second one with $J_a = 3J_M$, are presented in Figure 3.3. In both the cases the speed controller gain remains the same. It is clearly seen from Figure 3.3 that the speed controller without AF yields the undesirable peaking behaviour in closed loop where as the simulations with AF does not. This implies that the step response of the closed loop without AF is oscillating with a dominant frequency equal to the frequency of the peak in the bode plot shown in Figure 3.2. Another fact is that this frequency is higher than the original mechanical resonance frequency. The resonance frequency of the plant is about 130 Hz where as the frequency of oscillation in closed loop (represented by the peak) is well above the original resonance frequency, about 250 Hz. This once again proves the fact that the printing testbench can be classified as a mechanical system suffering from inertial-reduction instability as mentioned in Section 2.2.

Thus AF is effectively a method of reducing drives sensitivity to mechanical resonance achieved by electronically increasing the drive's inertia. This active inertia, J_a is superior because it does not require extra flywheels and does not limit the response of drive to fast commands as adding physical inertia would. For implementation, differentiating the measured motor velocity signal $\dot{\varphi}_M$ is not appropriate because the acceleration signal

that results is badly contaminated with quantization noise and has an inherent lagging property. Some interesting techniques to counteract these limitations are presented in Section 3.4.

3.4. Differentiation techniques for estimating the acceleration

Fast and robust estimation of the derivatives of measured (or sampled) time signals is a very important issue in a variety of applications in control engineering, failure diagnosis, signal processing, etc. Due to the fact that, in practice, signals are affected by measurement noise, main goal of any differentiator is to achieve a good signal-to-noise ratio for the calculated derivative. In this section three techniques for estimating the derivative of a signal corrupted with measurement noise are presented. First, a nonlinear technique namely the Robust exact differentiator (RED) which is based on a 2-order sliding mode algorithm[1] is presented. The second technique presented here

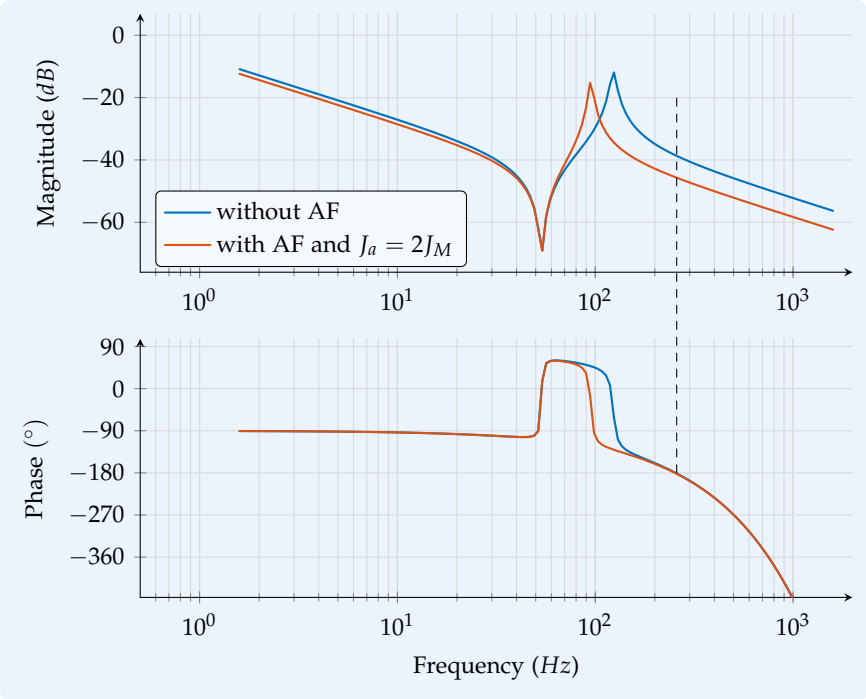

Figure 3.2.: Comparison (in simulation) of open loop bode plot with and without AF

[1]The underlying ideas of Sliding mode control are presented in Appendix C

is the so-called algebraic derivative estimation. This technique is used to approximate the derivative of a signal based on truncated Taylor series approximation of the signal and its representation as a chain of integrators. The third method uses LTI systems to approximate the derivative of a signal. The relative advantages/disadvantages of each method in view of implementation/tuning on a real-time hardware are discussed as well.

3.4.1. Robust exact differentiator

Levant [Lev98] proposed a robust exact differentiation (RED) technique based upon 2-sliding algorithm[2] for signals with a given upper bound on the Lipschitz's constant of their derivatives. Given an input signal $y(t)$, the *Lipschitz's* constant is a constant L defined as

$$L = \sup \frac{|y(t_1) - y(t_2)|}{|t_1 - t_2|} = \sup \left| \frac{\delta y}{\delta t} \right|. \tag{3.6}$$

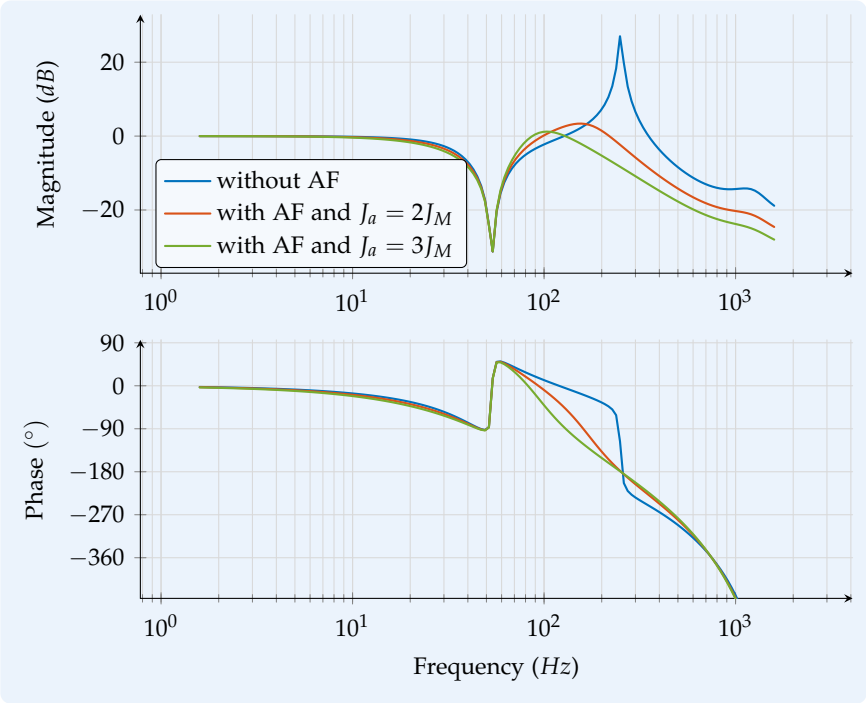

Figure 3.3.: Closed loop simulation of the speed controller for DIO with and without AF

[2]Refer Appendix C

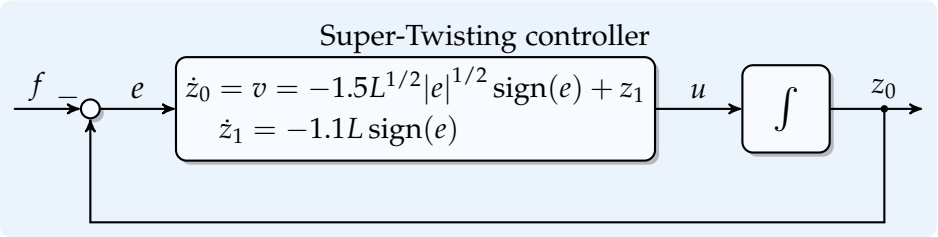

Figure 3.4.: Schematic illustration of Robust exact differentiator

Consider a signal $f(t)$ be a function defined on $[0, \infty)$, which is a result of real-time noise corrupted measurement of some unknown smooth signal $f_0(t)$ with the first derivative $\dot{f}_0(t)$ having a known Lipschitz constant $L > 0$, i.e. $|\ddot{f}_0(t)| \leq L$. The function $f(t)$ is assumed to be Lebesgue-measurable function, the unknown measurement noise $f(t) - f_0(t)$ is assumed to be bounded. The task is to estimate the derivative $\dot{f}(t)$ in real-time using only the values of f and the number L. The estimation is to be exact in the absence of noise i.e., $f(t) = f_0(t)$. Consider an auxiliary system (shown in Figure 3.4)

$$\dot{z}_0 = u, \tag{3.7}$$

where u is the control signal and let the sliding variable be defined as

$$e = z_0 - f(t). \tag{3.8}$$

The idea from here is to drive e and $\dot{e}$ to zero in finite time. This objective can be achieved by the use of a 2-sliding mode. In that case

$$\dot{e} = e = 0 \implies z_0 = f \text{ and } \dot{f} = u. \tag{3.9}$$

A *super-twisting controller* is employed in [Lev98] towards this goal. The differentiator is given as:

$$\dot{z}_0 = v = -\lambda_0 L^{1/2}|z_0 - f|^{1/2}\,\mathrm{sign}(z_0 - f) + z_1, \tag{3.10}$$

$$\dot{z}_1 = -\lambda_1 L\,\mathrm{sign}(z_0 - f), \tag{3.11}$$

with $\lambda_0 = 1.5$, $\lambda_1 = 1.1$. Here z_0 is the smoothed input f and both v, z_1 can be taken as $\dot{f}$. The sufficient convergence conditions are stated as

$$\forall \lambda_2 > L,\ \frac{2(\lambda_2 + L)^2}{\lambda_1^2(\lambda_2 - L)} < 1.$$

It is also shown in [Lev98] that:

1. If $f(t) = f_0(t)$, i.e. in the absence of noise

$$z_0 = f_0(t) \text{ and } z_1 = \dot{f}_0(t).$$

The differentiator is exact in the absence of measurement noise.

2. If $|f(t) - f_0(t)| < \varepsilon$, then there exists a positive constant μ depending exclusively on the parameters of differentiator such that,

$$|z_1 - \dot{f}_0(t)| \leq \mu\varepsilon^{1/2}$$

3. v is noisy in the presence of input noise (measurement noise) and z_1, a Lipschitzian signal, has a small phase delay in the presence of input noise.

4. The transient process time is uniformly bounded if the initial deviations $|z_0(t_0) - f(t_0)|$ and $|z_1(t_0) - \dot{f}(t_0)|$ are bounded.

Example 3.4.1 (RED)**.** This example illustrates the working of a robust exact differentiator as described by Equations (3.10) and (3.11). Consider a signal $f_0(t) = sin(\omega t) + 0.001sin(20\omega t)$; with $\omega = 2\pi * 50\,\text{rad/s}$. To this base signal a noise signal with sufficiently high frequency (filtered white noise with frequency components from 35 kHz to 50 kHz)components is added. The first derivative of f_0 has a Lipschitzian constant of 1.4 ω^2. A robust exact differentiator is calculated for differentiating this signal as described above, and the whole system is simulated with MATLAB/SIMULINK using Euler method with a sample time of 1e-5 s. Figure 3.5 plots the results from this simulation. Referring to the schematic shown in Figure 3.4 the legend in Figure 3.5 is understood as follows:

1. $u = v$: the output of differentiator, u, is taken as v,

2. $u = z_1$: the output of differentiator, u, is taken as z_1, and

3. $\dot{f}_0(t)$ represents the differentiation of the noise less base signal, $f_0(t)$.

It can be easily seen from Figure 3.5 that the noise content of the output signal in the first case is considerably greater than the noise content in second case. However, there is a small phase lag in the second case as mentioned above in this section. ▲

3.4.2. Robust exact differentiator of n-th order

An extension of the above mentioned differentiator to n-th order is proposed in [Levo3]. This differentiator assumes a Lipschitzian bound on the n-th derivative $f_0^{(n)}$ equal to L. The n^{th}-order differentiator has the form:

$$\left.\begin{aligned}
\dot{z}_0 &= v_0,\ v_0 = -\lambda_0 L^{1/(n+1)} |z_0 - f(t)|^{n/(n+1)} \operatorname{sign}(z_0 - f(t)) + z_1 \\
\dot{z}_1 &= v_1,\ v_1 = -\lambda_1 L^{1/n} |z_1 - v_0|^{(n-1)/n} \operatorname{sign}(z_1 - v_0) + z_2 \\
&\vdots \qquad\qquad \vdots \\
\dot{z}_{n-1} &= v_{n-1},\ v_{n-1} = -\lambda_{n-1} L^{1/2} |z_{n-1} - v_{n-2}|^{1/2} \operatorname{sign}(z_{n-1} - v_{n-2}) + z_n \\
\dot{z}_n &= -\lambda_n L \operatorname{sign}(z_n - v_{n-1}),
\end{aligned}\right\} \tag{3.12}$$

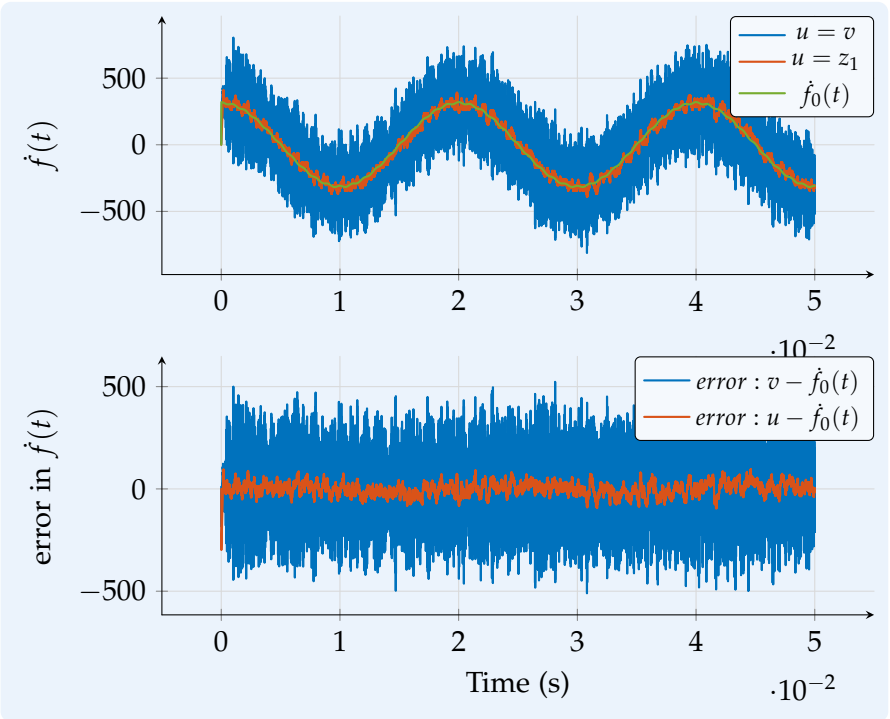

Figure 3.5.: Result of differentiation using RED

where $\lambda_i > 0$ for $i = 0, 1, \ldots, n$ are chosen sufficiently large. z_i is the i^{th} derivative estimate of the input signal.

Example 3.4.2 (RED-n-th order)**.** Consider the same signal as in example 3.4.1, but here a second order differentiator is used to generate the first derivative estimate. All the other simulation parameters remains the same. The constants λ_i are chosen according to [Levo3] as $\lambda_0 = 3, \lambda_1 = 1.5, \lambda_2 = 1.1$, and the results are plotted in Figure 3.6. It is evident from Figure 3.6 that using a second order differentiator for estimating the first derivative of the signal provides a much better accuracy in the presence of noise. Thus, the additional smoothness of the unknown input signal (known Lipschitz constant of second derivative) $f_0(t)$ is used to improve its derivative estimate based on the noisy measurement $f(t)$. ▲

Remarks on RED

Following remarks are relevant for the purpose of real-time implementation of the robust exact differentiator.

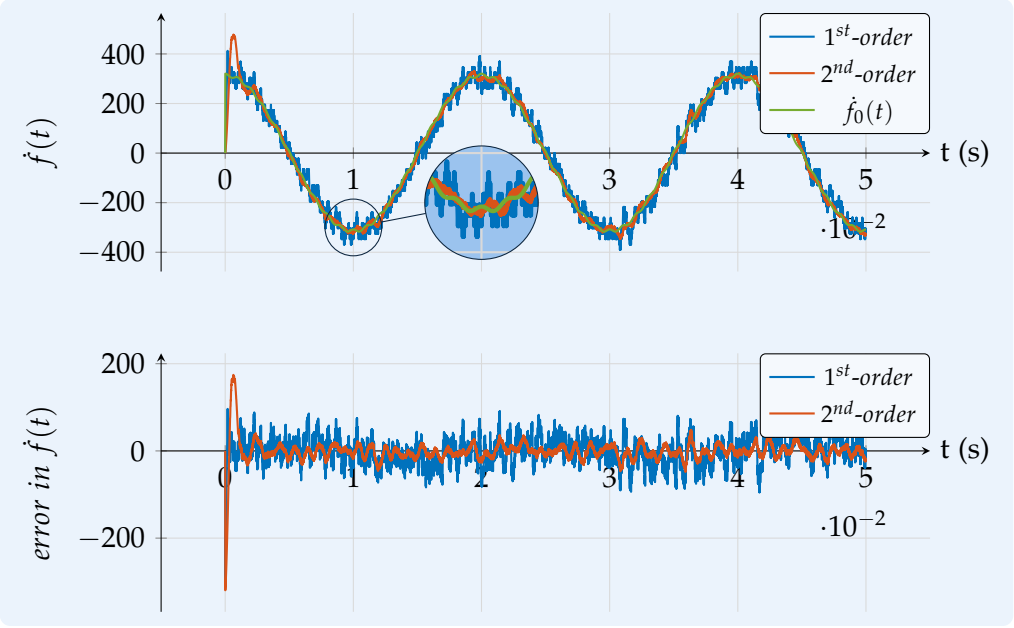

Figure 3.6.: First derivative calculated using first and second order differentiators

1. Knowledge of the Lipschitz constant for the signal to be differentiated is required for tuning the differentiator.
2. Both the variables v and z_1 from Equations (3.10) and (3.11) respectively can be used as the estimated derivative, i.e. both of them converge to $\dot{f}_0(t)$ in the absence of noise.
3. An n^{th}-order differentiator used to estimate l^{th} derivative, with $l < n$, produces a more accurate estimation, in the sense of signal-to-noise ratio.
4. Use of the smallest available integration and sample time steps produces accurate results.

3.4.3. Algebraic derivative estimation

Non-model based close approximations to time derivatives of arbitrary analytical time signals based on truncated Taylor series approximation and its representation as a chain of integrators is proposed in [RRF05]. Due to the fact that the estimates are solely based on the integrals of measured signals, this technique is quite robust with respect to measurement noise. Compared to a linear observer or a linear filter, the non-asymptotic nature of this algebraic derivative estimation technique promises faster estimation.

Consider an analytic time signal $y(t)$ whose derivative is to be determined. The truncated Taylor series approximation of order N is

$$y(t) \approx y_N(t) = \sum_{i=0}^{N} \alpha_i \frac{t^i}{i!}, \tag{3.13}$$

where the coefficients α_i are the *i-th* derivative of $y(t)$ evaluated at $t = 0$, i.e.

$$\alpha_i = \left.\frac{d^i y}{dt^i}\right|_{t=0} \text{ and } i = 0, \ldots, N. \tag{3.14}$$

Using *Laplace* transform,

$$y_N(t) \circ\!\!-\!\!\bullet\, Y_N(s) = \sum_{i=0}^{N} \frac{\alpha_i}{s^{i-1}}. \tag{3.15}$$

The main idea of algebraic derivative estimation method is to manipulate Equation (3.15) with the help of operational calculus, and to isolate the *j-th* coefficient $\alpha_j = y^{(j)}(0),\ j = 0, 1, \ldots, N$. Once this coefficient is isolated, it is transformed back into time domain to

obtain the estimate of the *j-th* time derivative of $y(t)$. The expression for *j-th* derivative is given as

$$y^{(j)}(t) \approx (-1)^j \int_0^T \Pi_{j,N}(t,\tau) y(t-\tau) d\tau, \tag{3.16}$$

where

$$\Pi_{j,N}(t,\tau) = \frac{(N+j+1)!(N+1)!}{t^{N+j+1}} \sum_{\kappa_1=0}^{N-j} \sum_{\kappa_2=0}^{j} \frac{(-1)^{N+j-\kappa_1-\kappa_2} \, (t-\tau)^{\kappa_1+\kappa_2} \, \tau^{N-\kappa_1-\kappa_2}}{\kappa_1!\kappa_2!(N-j-\kappa_1)!(j-\kappa_2)!(N+1-\kappa_1)(N-\kappa_1-\kappa_2)!(\kappa_1+\kappa_2)!} \tag{3.17}$$

where $y(t)$ is the measured signal and T represents the interval of integration. This interval of integration can be interpreted as the window width of a receding horizon strategy and should be chosen small to calculate the derivative estimate within an acceptable short delay. The advantage of this method is that the derivative is obtained by integration of weighted measured signal. In order to suppress the measurement noises the integration interval T has to be chosen large enough.

Example 3.4.3 (Algebraic derivative estimation)**.** Consider the same signal as in Example 3.4.1. A toolbox for Matlab called the derivative estimation toolbox [ZRH07] (DET) which uses the above mentioned algebraic derivative estimation is used for the derivative estimation in this example. Table 3.1 lists the simulation parameters used in this example. Figure 3.7 shows the result of derivative calculation using DET. Represented in blue is

Table 3.1.: Parameters of the simulation

Parameter	Value
Sample time T_s	1*e*-5 s
Window width T	70 T_s s
Taylor series order N	2

the estimated derivative, which is calculated using DET and in red is the derivative of the original noise free signal. The effect of the receding horizon window can be clearly seen from Figure 3.7. During the first 70 samples the derivative remains at zero and then almost instantaneously (non-asymptotically) jumps close to the expected derivative. Inset in Figure 3.7 shows the accuracy of the estimated derivative. ▲

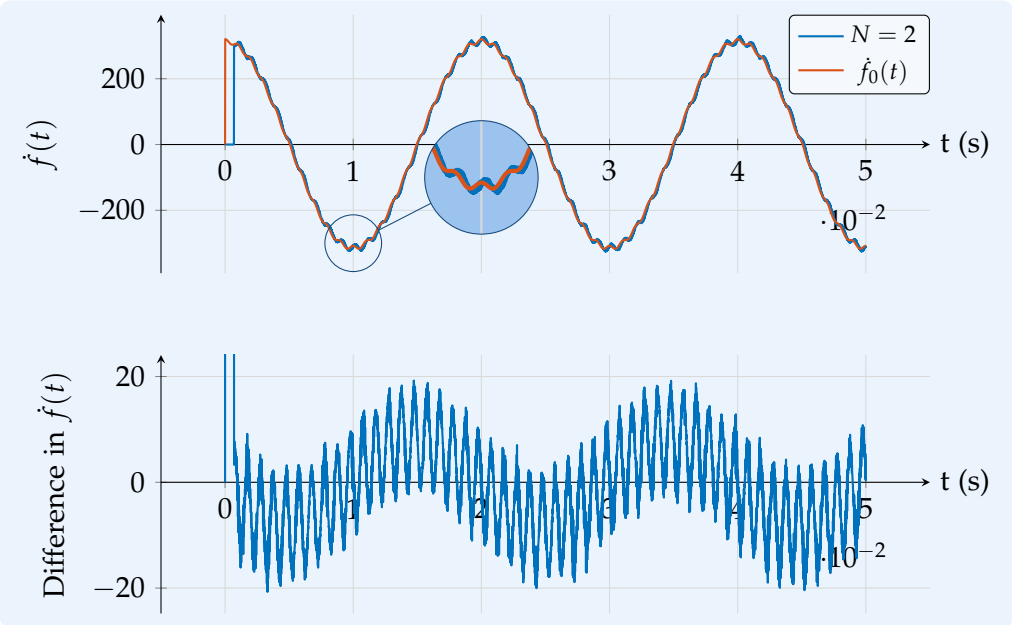

Figure 3.7.: First order derivative estimation using DET

Remarks on algebraic derivative estimation technique

Following remarks are relevant to the practical implementation on an industrial control unit.

1. Estimate of the derivative is only available after a time interval of T seconds but on the other hand the estimate is non-asymptotic.

2. Both the window width T and the order of calculation N are to be tuned beforehand in simulation, preferably with measurement data from the real-world plant.

3. Amount of processing power required depends on the window width and the sample time, because the number of measurement samples that has to be processed at any time is equal to $\frac{T}{T_s}$.

3.4.4. LTI filters for differentiation

Use of LTI filters in combination with a pure differentiator is a very well known technique. For example, a simple first order low-pass filter can be used

$$Y(s) = \frac{s}{\tau s + 1} U(s), \quad \tau > 0 \tag{3.18}$$

where $Y(s)$, $U(s)$ are *Laplace* transforms of the original signal $u(t)$ and $\hat{y}(t)$, the approximation of its derivative, respectively. τ is the time constant of the filter and s the *Laplacian* operator. Similar to the filter given in Equation (3.18) any higher order low-pass filters can be used to achieve a better approximation of the differentiated signal.

A particularly interesting filter is shown in Figure 3.8, where the LTI filter is restructured in the form of a control loop. Noise corrupted measurement signal ω_M enters the filter. The PID block is to be tuned so that the output of an auxiliary plant described as

$$\frac{d}{dt}\omega_{M,filt} = x, \tag{3.19}$$

tracks the input signal (ω_M) asymptotically. Note that this structure is very similar to the structure used in robust exact differentiator. Inspecting the auxiliary plant, x is the acceleration signal to be estimated and $\omega_{M,filt}$ denotes the filtered input signal ω_M. In the case of perfect tracking, i.e.

$$\epsilon := \omega_M - \omega_{M,filt} = 0 \tag{3.20}$$

holds and using Equations (3.19) and (3.20)

$$x = \frac{d}{dt}\omega_M \tag{3.21}$$

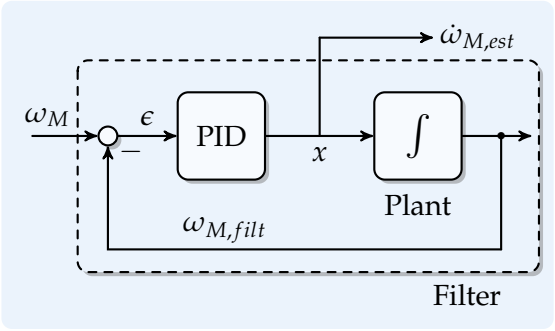

Figure 3.8.: Schematic of the acceleration signal filter

results.

The use of the above mentioned filter structure for calculating the derivative of a signal has the following advantages.

- The transfer function between the input ω_M and the filtered signal $\omega_{M,filt}$ can be tuned to behave as a low-pass filter by appropriately choosing the PID block parameters. Considering the PID parameters to be k_p, k_i, and k_d respectively, the transfer function of the filter is given as

$$\frac{\mathscr{L}\left\{\omega_{M,filt}\right\}}{\mathscr{L}\left\{\omega_M\right\}} = \frac{k_d s^2 + k_p s + k_i}{(1+k_d)\, s^2 + k_p s + k_i}. \tag{3.22}$$

  Choosing appropriate parameters will result in a second order low-pass filter. This is especially useful when the frequency range of the noise in the measured signal is known.

- The structure of the differentiator mentioned above permits it to be studied as an acceleration estimator. To this end, consider the differential equation (2.4), relating the motor acceleration and the electrical torque

$$\ddot{\varphi}_M = \frac{1}{J_M} T_e - \frac{k}{J_M} \Delta\varphi - \frac{d}{J_M} \dot{\varphi}_M + \frac{d}{J_M} \dot{\varphi}_L. \tag{3.23}$$

  If the signals containing stiffness k and damping d are considered as external disturbance, then (3.23) can be considered as an integrator with input $\frac{T_e}{J_M}$ and output $\omega_M = \dot{\varphi}_M$. With this consideration, the acceleration filter mentioned above can be restructured as an observer if the input T_e is measurable. In general the electrical torque input is directly proportional to the motor current which is measurable. Using the measured torque, the structure of the acceleration estimator is shown in Figure 3.9.

3.5. Acceleration feedback implementation on the printing testbench

Both the AF and the differentiator for calculating the acceleration signal are implemented in the current controller part of the standard cascaded control structure shown in Figure 2.13. Due to the unavoidable processing power restrictions imposed by ACOPOS and for

the sake of simplicity of tuning, an acceleration estimator as shown in Figure 3.9, which offers both the advantages of being intuitive to tune and computationally economical, is implemented for differentiating the measured velocity y_m on the testbench.

In order to tune the PID bock in the estimator the transfer function between ω_M and $\omega_{M,filt}$ is considered

$$\frac{\mathscr{L}\{\omega_{M,filt}\}}{\mathscr{L}\{\omega_M\}} = \frac{k_{p,AF}s + k_{i,AF}}{s^2 + k_{p,AF}s + k_{i,AF}}, \tag{3.24}$$

where $k_{p,AF}$ and $k_{i,AF}$ are the proportional and integral gains[3]. Now the filter is tuned by choosing these gains such that the transfer function (3.24) has desired dynamics. In this work, these desired dynamics are chosen as a second order Butterworth low-pass filter, which gives a flat frequency response within the filters bandwidth. The characteristic polynomial of such a second order Butterworth filter is given as

$$s^2 + \sqrt{2}s\omega_c + \omega_c^2, \tag{3.25}$$

where ω_c represents the corner or cut-off frequency of the filter. Comparing the desired dynamics against the filter dynamics, the gains are chosen as

$$k_{p,AF} = \sqrt{2}\omega_c \tag{3.26}$$

$$k_{i,AF} = \omega_c^2. \tag{3.27}$$

For the experiments in this work the filter is set to have a cut-off frequency of 400 Hz.

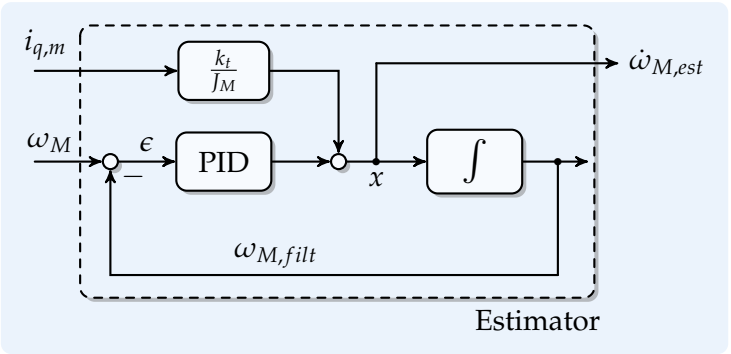

Figure 3.9.: Schematic diagram of the acceleration signal filter with additional feed-forward path

The torque input is calculated based on the measured quadrature component of the

[3]Derivative part is ignored for obvious reasons.

current $i_{q,m}$ and the known torque constant k_t of the PMSM motor[4] as

$$T_e = k_t i_{q,m}, \tag{3.28}$$

The structure of the acceleration estimator with inputs ω_M, $i_{q,m}$ is presented in Figure 3.9.

3.6. Experimental results and discussion

Acceleration feedback together with the acceleration estimator mentioned in the previous section are implemented on the printing testbench and experiments are made to analyse the impact of AF on the speed controller. The experimental setup used here is explained

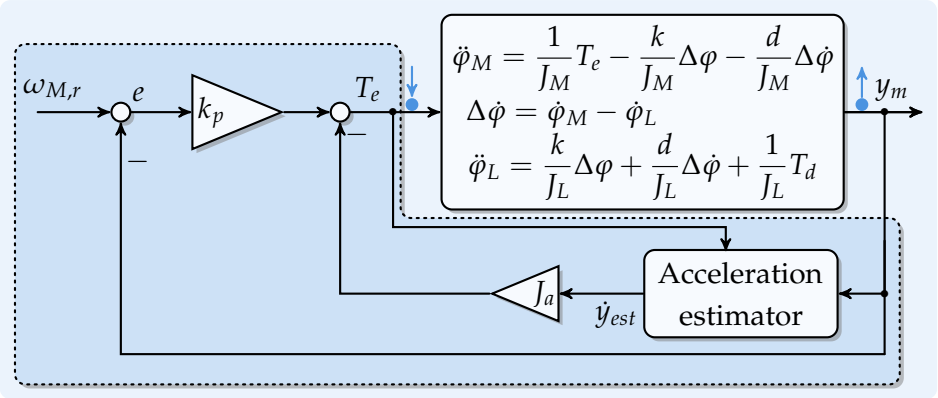

Figure 3.10.: Schematic depicting the experimental setup

based on the schematic shown in Figure 3.10. The actuating motor is driven in speed control mode and AF along with the acceleration estimator are running in the current controller (refer Figure 2.13) of the ACOPOS. In order to verify the influence of AF on the DIO plant several frequency response and step response measurements were taken by varying the speed controller gain and the additional moment of inertia J_a. The frequency response is calculated between the plant input torque and the measured output angular velocity, represented by the blue arrows in Figure 3.10. One result from

[4]zero-direct-axis-current control [Krio1] is used for the PMSMs, allowing the simple linear relation between the torque and the direct component of the current when the parameters of the motor are assumed to be independent of the variations in temperature.

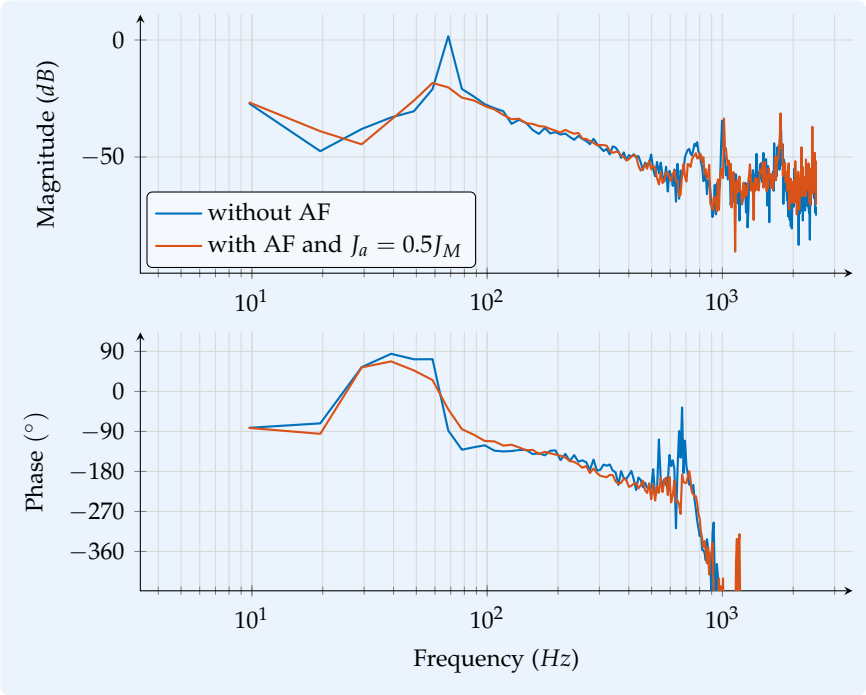

Figure 3.11.: Open loop frequency response depicting the influence of AF

a frequency response test is presented in Figure 3.11 [5]. The depicted plot shows the frequency response of the testbench from torque to motor velocity with and without AF. The value for additional moment of inertia J_a[6] is chosen to be equal to half that of the motor inertia J_M for this experiment. It is evident that the resonance frequency is shifted from around 70 Hz to around 60 Hz and also the magnitude peak at the resonance frequency is damped by about 20 dB. But the open loop gain margin in both the cases is more or less the same, which is unlike the simulation results shown in Figure 3.3. Further results with different values of J_a are depicted in Figure 4.3 presented in the next chapter, also the justification for this unexpected behaviour based on a careful analysis is presented.

In order to see the influence of AF on the performance of the speed controller in time domain, the following experiment is conducted. The actuating motor (see Figure 2.9)

[5]When compared to the measured frequency response shown in Figure 2.15 the resonance frequency of the plant is shifted from around 130 Hz to around 70 Hz. This is because of a change in the shaft to a less stiffer one with stiffness of 9.7541 kN.m/rad.

[6]The values of J_a are always taken as multiples of J_M.

is operated in speed control mode[7], and the parametrization of the speed controller (proportional controller) is performed such that there is gain margin of around 10 dB, which results in the speed controller gain of 70 $\frac{As}{rad}$. The disturbance motor is operated in torque control mode where the current controller parameters are auto tuned by the ACOPOS. With this setup a disturbance torque T_d equal to 32 $N.m$ is applied using the disturbance motor, while the actuating motor is running at a constant speed of 1 Hz. This disturbance is applied as a step by changing the reference current $i_{q,r}$ of the disturbance motor. The motor angular velocity is measured in both the cases with (once again the result shown here is with $J_a = 0.5J_M$) and without AF and is plotted in Figure 3.12. The depicted plot shows that as the step disturbance is applied at about 0.1 s, resonance oscillations are introduced in the velocity and that the magnitude of these oscillations is greatly reduced with AF. Any further increase in the additional J_a inertia

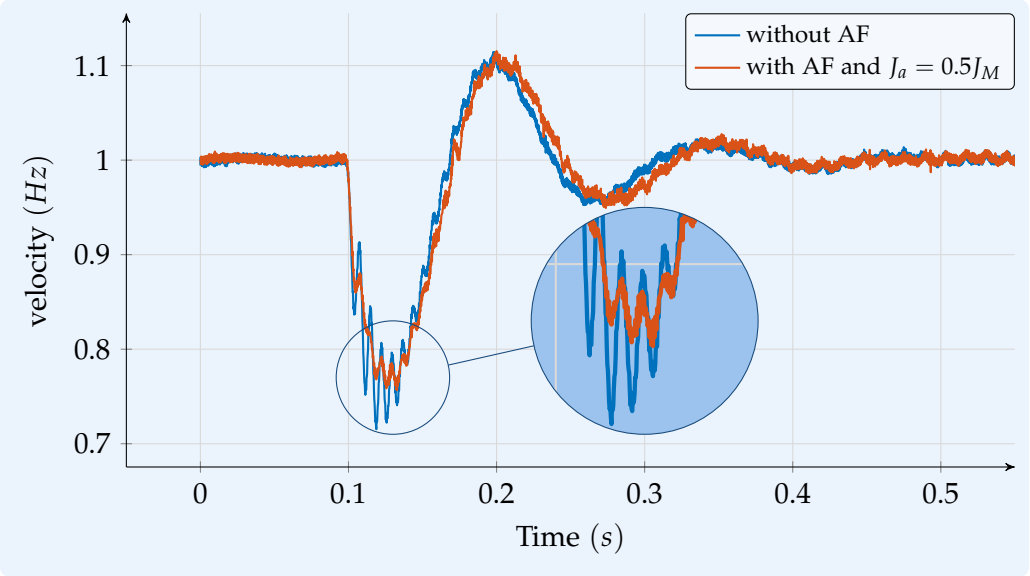

Figure 3.12.: Plot depicting the effect of disturbance on the motor velocity with and without AF

through AF did not bring in any improvement, in fact J_a values above J_M worsened the closed loop response. The reason behind this limit on J_a and a possible way to overcome this limit is dealt with in the next chapter.

[7]refer Section 2.3.2

4. Extended Acceleration Feedback

An extension to the AF technique is proposed in this chapter. It is mentioned in Section 3.6 that there exists a maximum value for the additional inertia J_a above which unwanted oscillations are introduced into the speed control loop. First the reason behind this performance limitation is presented Section 4.1. The technique itself and the numerical simulations using MATLAB are given in Section 4.2. Section 4.3 presents the results of experiments on the printing testbench. Section 4.4 concludes this chapter.

4.1. Motivation

As mentioned before the maximum value of J_a using AF is limited, implying that the improvements in gain margin is limited which ultimately limits the performance improvement of the speed controller. For the purpose of analysing the reason behind this limitation with AF, consider the following schematic shown in Figure 4.1. The closed

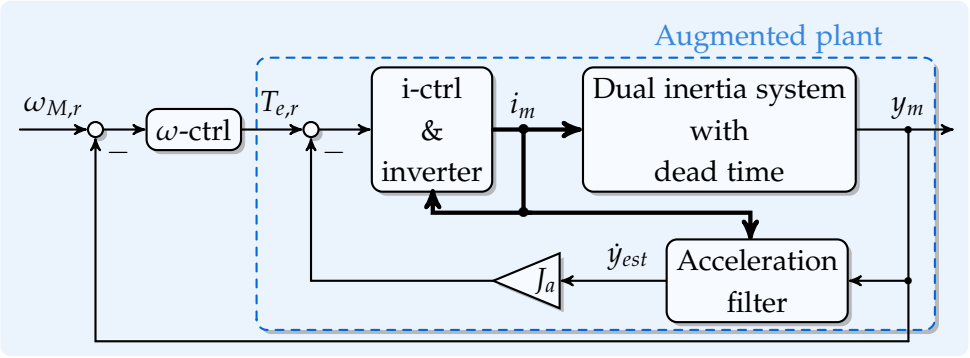

Figure 4.1.: Schematic of the setup with AF

loop with in the blue highlighted rectangle, consisting of the current controller, the plant and the AF is referred to as "Augmented plant". It is to be noted that the dynamics of this augmented plant can be influenced by changing the value of J_a. In this work the dynamics of the current controller and inverter are neglected because their dynamics are considerably faster compared to that of the speed controller (ω-ctrl in Figure 4.1), and the acceleration filter is assumed to be ideal.

In order to study the influence of J_a on the performance of the speed control loop first the augmented plant is studied. Since the augmented plant is itself a closed loop consisting of the DIO and the AF, its open-loop frequency response is analysed. Its open loop transfer function is given as

$$\begin{aligned} G_{ap} &= G_{dio} e^{-\tau s} \cdot s J_a \\ &= \frac{J_a}{J_M + J_L} \frac{J_L s^2 + ds + k}{\left(\frac{J_M J_L}{J_M + J_L}\right) s^2 + ds + k} e^{-\tau s}. \end{aligned} \tag{4.1}$$

Figure 4.2 presents the open loop frequency response of the augmented plant with $J_a = 0.75 J_M$ and $J_a = 2 J_M$. It can be obviously seen from the figure that gain margin of the augmented plant is close to zero when $J_a = J_M$ and the gain margin becomes negative when $J_a > J_M$, ultimately leading to the well known peaking behavior in the magnitude of the closed loop frequency response. This is also confirmed in Figure 4.3 where experimentally measured frequency response plots from the printing testbench are plotted with varying values of J_a. The *secondary peak*[1] clearly forms around the first phase crossover frequency 250 Hz. On the other hand as J_a is increased the frequency and magnitude of the resonance peak is reduced, but this improvement is negated by the secondary peak as it is close to the phase crossover frequency. The aim behind the extended acceleration feedback (EAF) is to manipulate this secondary peak in such a way that there is a positive influence on the speed controllers performance by regaining the eroded gain margin due to the secondary peak.

Similar conclusion can be drawn with the help of *Describing function* analysis [Kha02]. Consider that the speed controller is a saturated proportional controller, then the describing function is given as

$$N(A) = \frac{2k_p}{\pi} \left[\arcsin \frac{a}{A} + \frac{a}{A} \sqrt{1 - \left(\frac{a}{A}\right)^2} \right], \quad A \geq a, \tag{4.2}$$

[1] The primary peak being the peak in magnitude due to the mechanical resonance.

where A denoted the amplitude of sinusoidal input signal of the nonlinear element, a is half the width of the linear zone[2] and k_p is the proportional gain. Introduce for the sake of analysis a new constant $\rho = \frac{a}{A}$, and differentiate $N(A)$ with respect to ρ

$$\frac{d}{d\rho}N(A) = \frac{2k_p}{\pi}\left(\frac{1}{\sqrt{1-\rho^2}} + \sqrt{1-\rho^2} - \frac{\rho^2}{\sqrt{1-\rho^2}}\right) \tag{4.3a}$$

$$= \frac{4k_p}{\pi}\sqrt{1-\rho^2}. \tag{4.3b}$$

The describing function (4.2) is valid only when $A \geq a \Rightarrow \rho \leq 1$ and from (4.3b) $\frac{d}{d\rho}N(A) > 0$, so $N(A)$ is a decreasing function as A is increasing and similarly $-1/N(A)$ is also decreasing. The range of possible values for the amplitude A are from a to ∞, and $-1/N(a) = -1/k_p$ and $-1/N(\infty) = -\infty$. Therefore, the locus of $N(A)$ is a straight line starting from $-1/k_p$ and limiting at $-\infty$. Based on the well known *equation of harmonic balance* [Vido2] a limit cycle occurs at the intersection of the Nyquist plot of

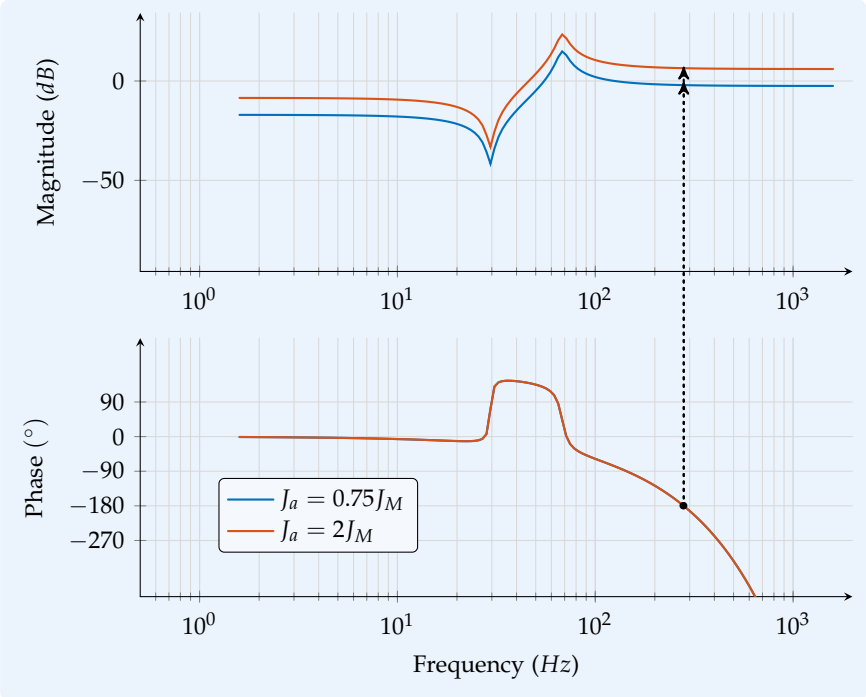

Figure 4.2.: Open loop frequency response of the augmented plant showing the loss of gain margin with the increase in J_a

[2]The parameter a depends on the slope and the saturation limits in the controller.

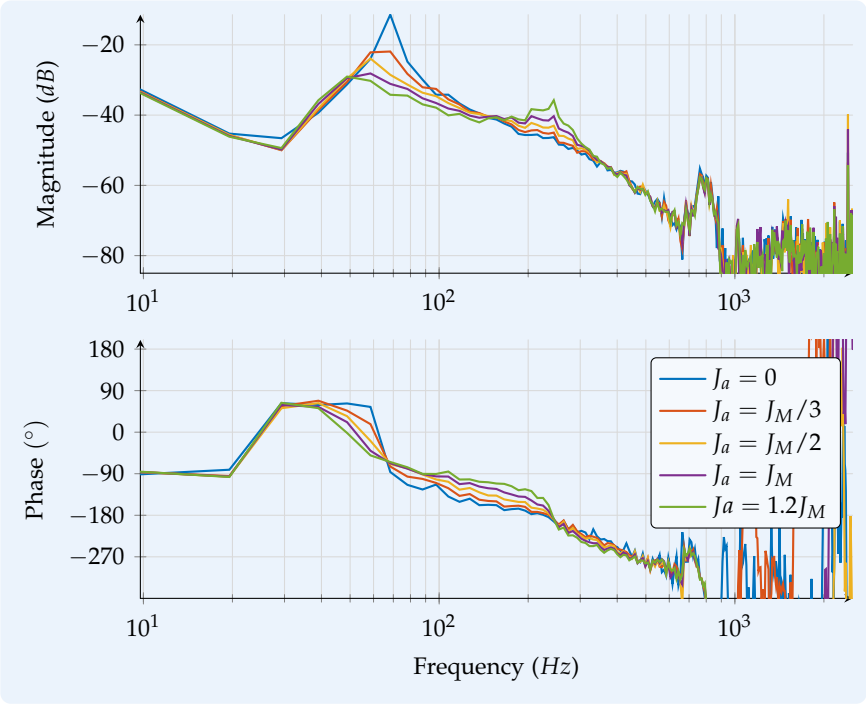

Figure 4.3.: Measured frequency response on the printing testbench with AF showing the influence of J_a

the open-loop (see Figure A.4) and the straight line $-1/N(A)$, i.e. the $-180°$ phase cross-over frequency of the open loop Bode diagram. This once again confirming the conclusion arrived upon by considering the secondary peak argument before.

4.2. Extended acceleration feedback and numerical simulations

The proposed method, Extended Acceleration Feedback (EAF), extends the applicability of AF by manipulating the secondary peak as mentioned in Section 4.1. In order to attenuate the secondary peak an additional filter is employed (see Figure 4.4). Any of the following filters can be used

- Low pass filter
- Lag filter
- Notch filter.

Use of any of the above mentioned filters should also take into account the amount of the introduced phase lag. This is particularly important because, the amount of phase lag introduced by the additional filter influences the first phase crossover (of the open speed control loop) which ultimately determines the gain margin of the speed control loop [MRH12].

Initially the Inward approach [CS90; Che95] is used for the design of the lag and low pass filter. For this approach the closed loop specifications were given in terms of rise time and maximum overshoot. From these specifications the dominant pole pair were calculated. Then the desired closed loop transfer function is designed by placing the remaining stable poles (order of closed loop system[3] - 2) sufficiently away from the dominant pole pair. This design technique did not result in expected behaviour as the controller calculated using the inward approach introduces zeros into the system that the designer has no control over.

Later the filters were tuned in simulation so that the secondary peak in the magnitude plot has the maximum attenuation while keeping the phase lag around the secondary peak frequency to a minimum. For example the plots in Figure 4.5 represent the simulated frequency response of $G_{OL,EAF}$ with AF and EAF using a lag filter, where

$$G_{OL,EAF} = G_{\omega-ctrl}.G_{EAF-filter}.G_{ap}, \tag{4.4}$$

and $G_{\omega-ctrl}$, $G_{EAF-filter}$ are the transfer functions of the speed controller and the EAF-filter respectively. If the amount of phase lag around the secondary peak is too much then the crossover frequency shifts to the left decreasing the gain margin, on the other hand

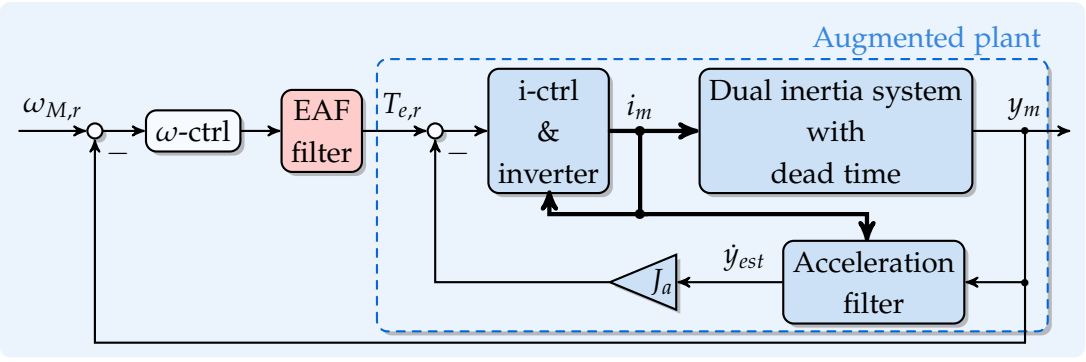

Figure 4.4.: Schematic of extended acceleration feedback

[3]Dead time is approximated as a rational transfer function using Padé approximant

if the phase lag at the crossover frequency is small then the gain margin is improved as shown in the plot. Due to this reason a lag filter is preferred to a low pass filter[4] because the lag filter can provide (at and after a given frequency) the maximum attenuation of the magnitude with very small phase lag.

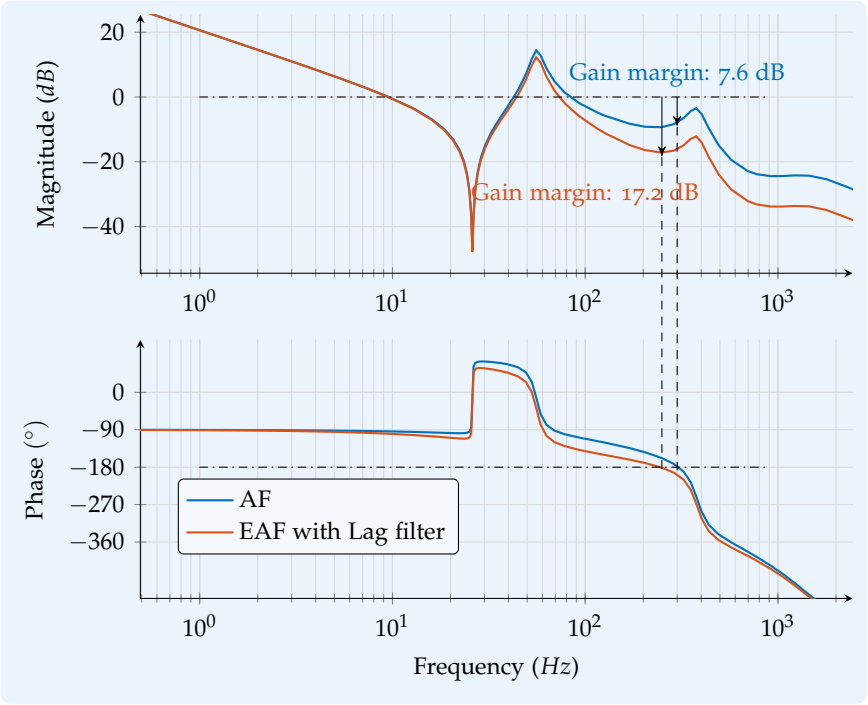

Figure 4.5.: Frequency response plot depicting the increase in gain margin with the use of EAF

Parameterization of the Lag and Notch filters

This section describes the parametrization of lag and notch filters that are used in this work. The lag filter is parametrized based on the mean frequency ω_0 and the maximum lag $\Delta\varphi_{max}$ to be achieved at the mean frequency [HN04]. The parametrized lag filter is

[4]The magnitude of a first order low pass filter rolls off at 20 dB/decade (or at a higher rate for filters of higher order) while the phase lag increases from 0 to 90 degrees and remains at 90 degrees for high frequencies.

given as

$$G_{lag}(s) = \frac{1 + \frac{s\alpha}{\omega_f}}{1 + \frac{s}{\omega_f}}, \tag{4.5}$$

where

$$\omega_f = \omega_0\sqrt{\alpha}, \text{ and } \alpha = \frac{1 - sin(\Delta\varphi_{max})}{1 + sin(\Delta\varphi_{max})}. \tag{4.6}$$

The maximum amount of amplitude attenuation from the lag filter is given as

$$\Delta A_{max} = 20\log_{10}(\alpha). \tag{4.7}$$

Figure 4.6 plots the frequency response of a lag filter with the mean frequency at 110 Hz and varying phase lags at the mean frequency. It can be seen clearly from the plot that the magnitude of the lag filter (depicted in red color) starts from 0 dB and reaches a constant maximum value of -4.6 dB, while the phase lag starts at 0° goes to a maximum of 15° and goes back to 0° at high frequencies. This behaviour of the lag filter makes it possible to attenuate the magnitude at a frequency while keeping the phase lag at that frequency to a minimum, thus rendering it a good candidate for the use in EAF.

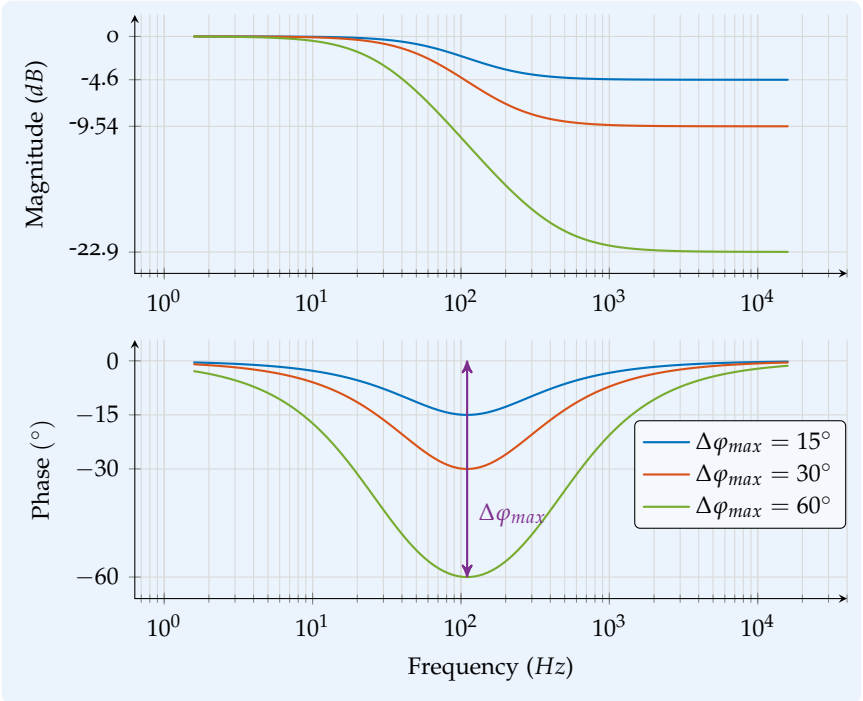

Figure 4.6.: Figure plotting the frequency response of lag filter

Notch filter is parametrized by the notch frequency and the bandwidth. The notch frequency is the frequency at mean frequency ω_0 around which the notch filter is active and the bandwidth ω_{BW} is the difference of the -3 dB cut-off frequencies. The maximum attenuation from the filter ΔA_{max} is fixed to be equal to -40 dB. The filter is given as

$$G_{NF}(s) = \frac{s^2 + 0.01\omega_{BW} + \omega_0^2}{s^2 + \omega_{BW} + \omega_0^2}. \tag{4.8}$$

Figure 4.7 plots the frequency response of a notch filter with the mean frequency at 250 Hz and a bandwidth of 150 Hz.

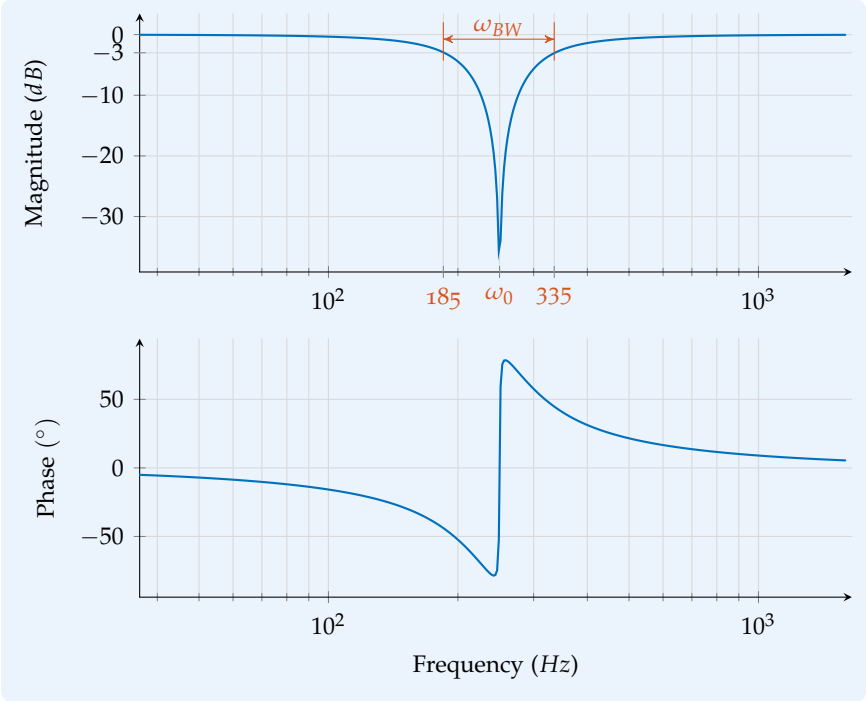

Figure 4.7.: Plot depicting the frequency response of a Notch filter

Matlab tool for estimating the optimal value of J_a

The effect of a well tuned lag filter in series with the speed controller on the frequency response of the open loop, i.e. $G_{OL,EAF}$ can be seen from Figure 4.5. The major advantage with EAF is that the open loop gain margin is improved. This implies that the maximum value of J_a, represented as $J_{a,max}$, for which the closed speed control loop is stable should

also increase compared to AF. The aim of this section is to be able to pre-compute an optimal value for J_a so that the commissioning times can be reduced. This can be done with the help of the flow chart shown in Figure 4.8. First the type of filter and the filter parameters are initialized, then using a pre-defined value for J_{step}, J_a is incremented as shown in the increment (`incr`) block. Using the values of J_a and filter parameters the open loop and closed loop transfer functions, represented by $G_{OL,EAF}$[5] and T_{EAF} respectively, are calculated. The stability of the closed loop determines if the calculation has to be further carried on. If the closed loop is stable, the gain margin of

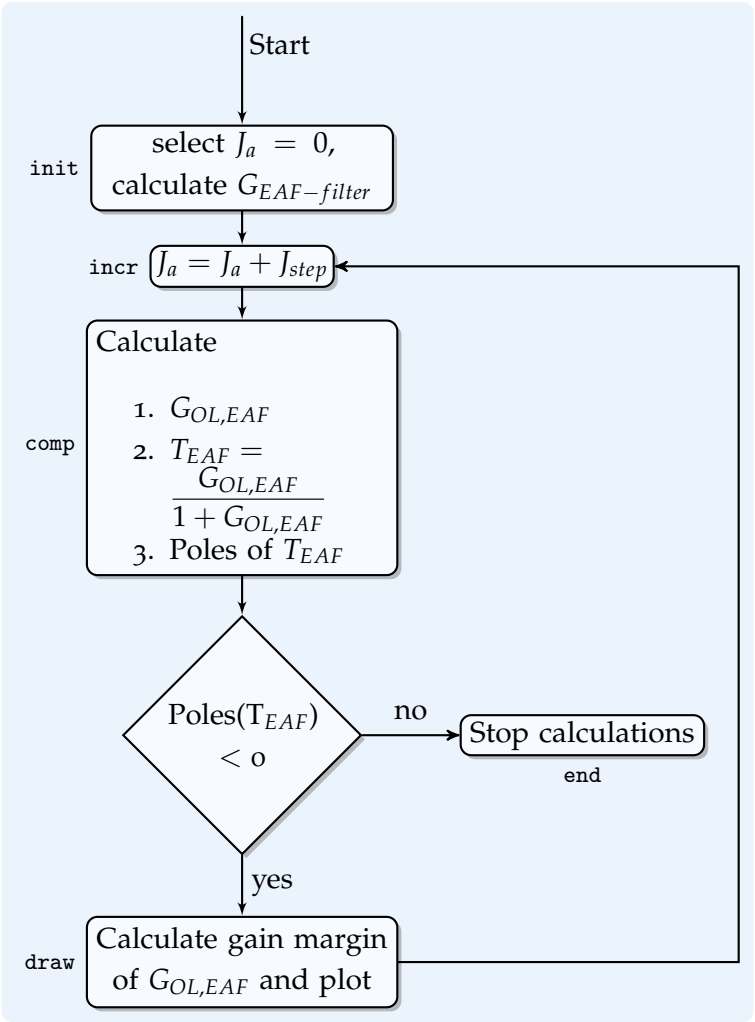

Figure 4.8.: Flow chart to calculate the maximum values of J_a.

[5]Once again the dead time is approximated with the help of Padé approximant.

Table 4.1.: Simulation parameters

Parameter	Value	Units
J_M	0.0658	kg.m^2
J_L	0.2843	kg.m^2
d	2.51	N.m.s/rad
k	9.754	kN.m/rad
τ	0.0012	s

the open loop is calculated from its transfer function $G_{OL,EAF}$ and plotted against the corresponding value of J_a. Figure 4.9 shows such a plot for the printing testbench model. The parameters used for the simulation are tabulated in Table 4.1. The optimal value of J_a as represented by J_a^* in Figure 4.9 represents the value of J_a for which the open loop, represented by $G_{OL,EAF}$ has the maximum gain margin. It can be seen that with AF, the maximum gain margin is achieved for $J_a = \frac{5J_M}{6}$, which is a close match to the actual value from measurements as mentioned in Section 3.6.

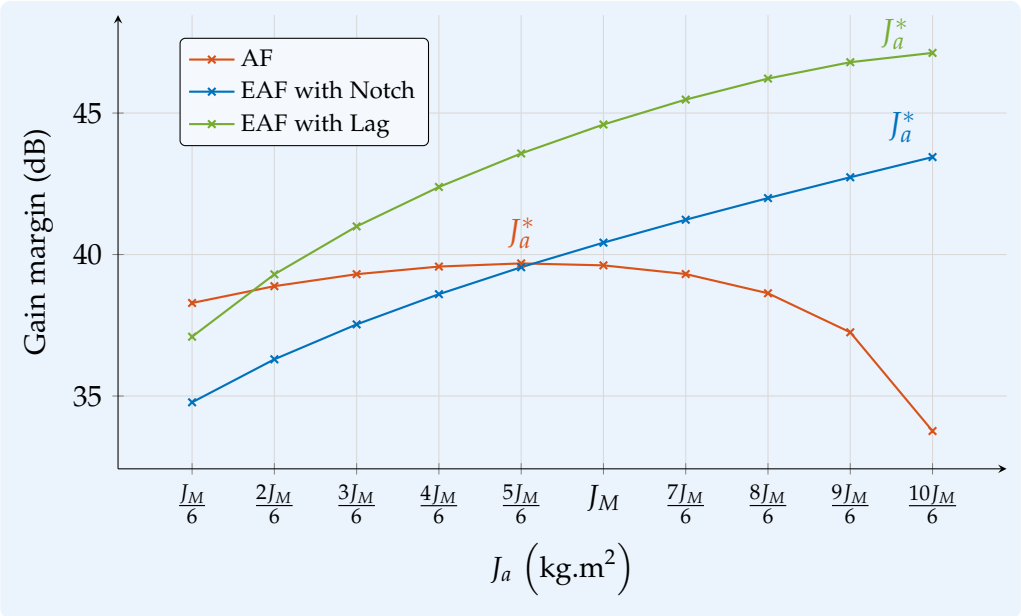

Figure 4.9.: Plot of Gain margin Vs J_a generated using MATLAB, depicting the optimal values J_a^*

4.3. Experimental results and discussion

4.3.1. Frequency response measurements

The proposed EAF filters are implemented in the current controller part of the ACOPOS firmware (refer Figure 2.13). The lag filter is tuned to provide a phase lag of -30° at a mean frequency of 110 Hz and the notch filter is tuned to have a bandwidth of 100 Hz at 250 Hz (mean frequency). With these filters in place, once again open loop frequency response measurements are made on the testbench with the help of PRBS signal. Measured frequency response for three different configurations (cf. to the legend in Figure 4.10) are plotted in Figure 4.10. In each configuration the value of J_a was set to the optimal value as determined from Figure 4.9.
Compared to the frequency response plot with AF, the addition of notch filter shifted the first phase crossover frequency from around 240 Hz to 180 Hz. Also the secondary peak as discussed in Section 4.2 is attenuated by the notch filter. Due to the lag filter the phase crossover is shifted to 160 Hz and there is also a considerable increase in the gain

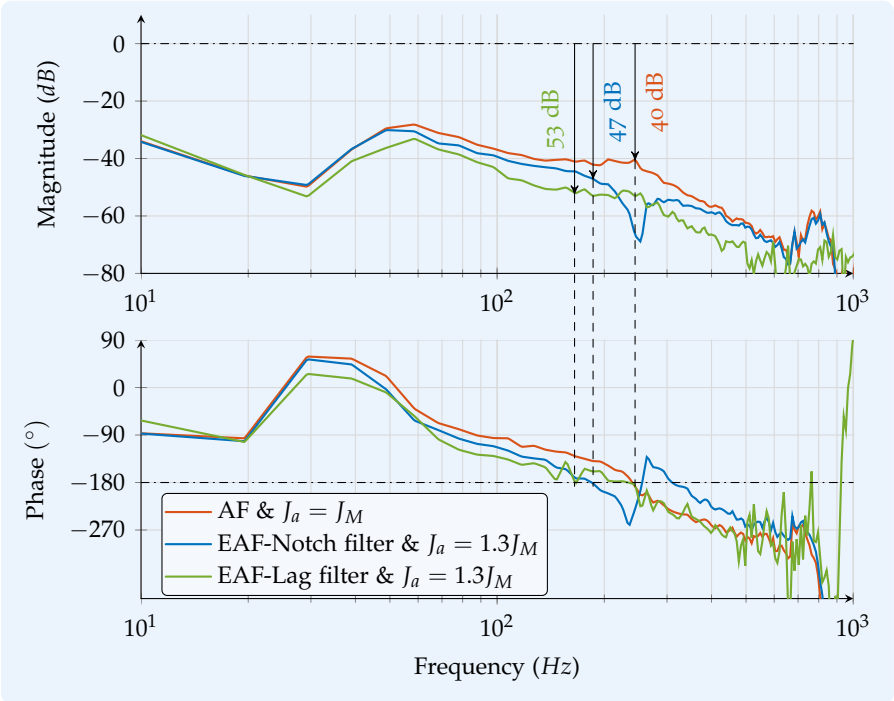

Figure 4.10.: Measured frequency response plots comparing AF and EAF

margin as depicted in Figure 4.10. The simulated gain margins as plotted in Figure 4.9 are in good accordance with the experimental values shown in Figure 4.10.

In order to see the influence of EAF on the speed controller's [6] gain, i.e. to transform the values of gain margins calculated from Figure 4.8 to k_v, the *maximum peak criteria* [SP05, p. 35] is used. According to this criteria, the maximum peak in the complementary sensitivity function[7], defined as

$$M_T = \max_{\omega} |T_{EAF}(j\omega)| \tag{4.9}$$

should be less than 2 dB. A larger value of M_T indicates poor performance as well as poor robustness. If $M_T = 2\ dB$ it can be ensured that the gain margin $GM \geq 1.5$ and the phase margin $PM \geq 29^\circ$. The value of M_T can be estimated either graphically or can be calculated numerically. M_T can be read from the Nichols chart by the use of M-circles (See Figure 5.2). In order to calculate M_T numerically first a speed controller gain is chosen, then using the measured frequency response data from the testbench the closed loop frequency response is calculated. M_T is extracted from this data as the maximum peak in the amplitude and compared against the specification. If the estimated M_T is smaller than the specification, the chosen value of speed controller's gain is increased and the process is repeated until the specification is met. Figure 4.11 shows the numerically calculated frequency response plots of $G_{OL,EAF}$ and T_{EAF} using the measured frequency response of G_{ap}. The calculated values of speed controller gains which meet the maximum peak criteria, denoted by $k_{v,max}$, are plotted against the value of J_a in Figure 4.12.

4.3.2. Time domain measurements

In order to compare the effects of EAF in the time domain, first a benchmarking experiment is carried out without EAF. The aim of this benchmarking experiment is once again, as presented in Section 3.6, to simulate a disturbance toque T_d using the disturbance motor (running in constant torque mode) and measure its effect on the speed controller.

[6] The speed controller is assumed to be a proportional controller. The reason behind this choice will be made clear in Section 4.3.2.

[7] For the unity-feedback loop configuration, the closed loop transfer function also known as the complementary sensitivity function is given as $T(s) = \dfrac{L(s)}{1 + L(s)}$, where $L(s)$ is the open-loop transfer function.

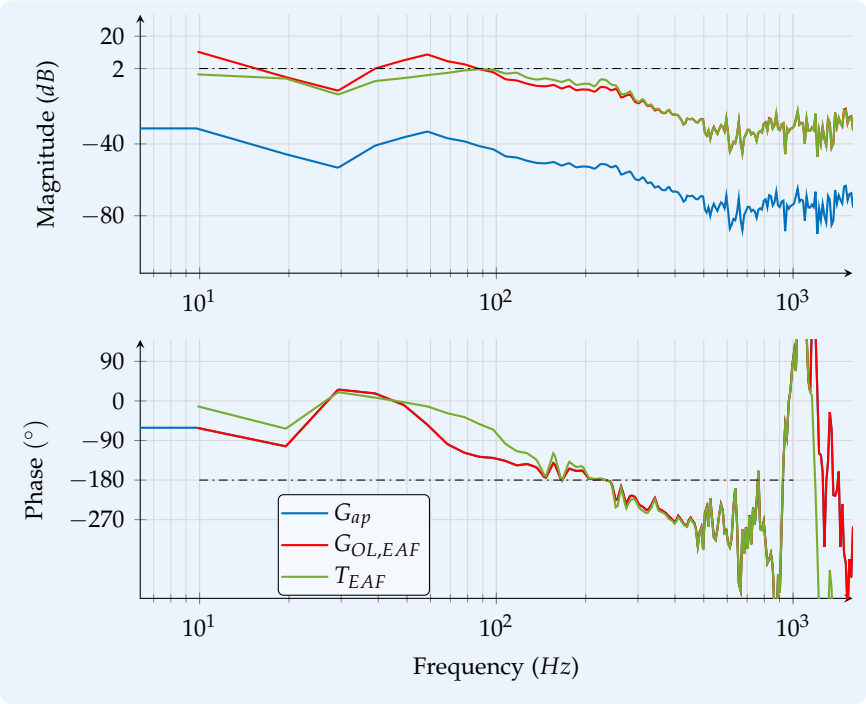

Figure 4.11.: Frequency response plots to calculate k_v using maximum peak criteria

Benchmarking experiment

Normally a printing machine is operated in full cascade control mode as shown in Figure 2.13 (i.e. all the three controllers, position, speed and current are active) to achieve a better printing performance. In addition to the feedback controllers, also feed-forward control is employed to further improve the performance. The lag error calculated within the position control loop is considered as a performance measure. For the benchmark experiment the values of k_p and k_v are chosen as

- $k_p = 50$, proportional gain of the position controller
- $k_v = 120$, proportional gain of the speed controller.

Idea in this experiment is to increase the value of k_v until the loop becomes unstable, where as the value of k_v from Figure 4.12 was based on the more conservative maximum peak criteria. A rectangular periodic disturbance of magnitude ± 16 Nm is applied using the disturbance motor (refer Figure 2.9).

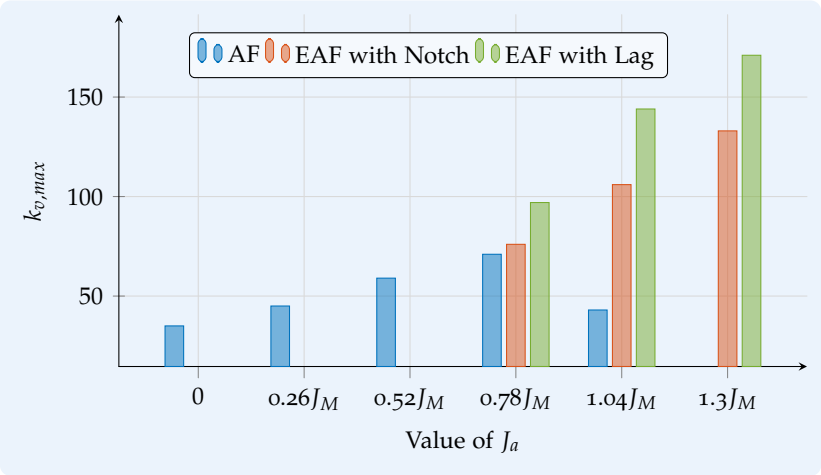

Figure 4.12.: Maximum values of k_v, for which the closed loop satisfies the maximum peak criteria, plotted against J_a.

Experiment with EAF

The same experiment as mentioned previously is repeated with EAF using the lag filter presented in Section 4.3. The proportional gains this time were set to

- $k_p = 50$
- $k_v = 180$.

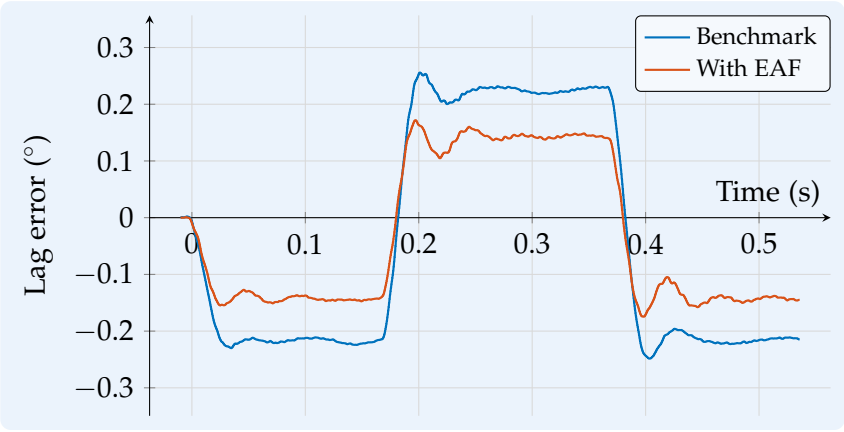

Figure 4.13.: Lag error plot showing the improvement with the use of EAF

Here the position controller remains the same as that of the benchmarking experiment where as the gain of the speed controller is more due to EAF. The resulting lag error in both the experiments is plotted in Figure 4.13. The lag error of the position control loop with EAF has been improved by about 35% compared to the benchmarking experiment. This improvement is attributed to the fact that with an increase of the loop gain, both bandwidth and disturbance attenuation property of the closed loop are improved. This improvement in the loop gains is a direct result of the improvements in the gain margin achieved with the help of EAF.

4.4. Conclusions

Mechanical resonance in electromechanical systems is a phenomenon that is the result of elastic transmission elements used within these systems. In order to meet strict control requirements, these transmission elements are made to have high stiffness to damping ratio resulting in weakly damped resonance frequencies. If these weakly damped resonance frequencies are excited (by for example a disturbance torque), they could lead to a degradation of the controller's performance or in worst case to the drive failure. These resonance frequencies can be divided into two categories, low-frequency and high-frequency resonances depending on how they effect the speed control loop. Low-frequency resonance limits the bandwidth of the speed controller, by decreasing its gain margin (due to the increased gain at and above the resonance frequency), where as the high-frequency resonance does not influence the bandwidth of the speed controller as it is well above the first phase crossover frequency. This distinction is very important in order to design techniques for counteracting the resonance frequency. With the use of acceleration feedback, the magnitude of the resonance peak can be attenuated and the resonant frequency itself can be shifted to lower frequencies. This reduction in magnitude at the resonance frequency helps for the improvement of bandwidth of the speed controller. Another feature of this technique is that it is robust against parameter variations. Following list briefly describes the major results from Chapter 3 and Chapter 4. In conclusion the following remarks are made:

- Acceleration Feedback technique is analysed and implemented on the ACOPOS system,
- The possibility of using AF to increase the loop gains, by improving the gain margin, is presented, and

- Frequency response measurements also indicate the increase in the gain margin.
- Limitation of AF technique has been presented and an extension to AF, using loop-shaping ideas is proposed which further improves the performance of the speed control loop.
- The performance improvement has been experimentally demonstrated both in time and frequency domain.
- MATLAB tools for pre-computing the optimal values of J_a, the additional inertia added by AF and k_v, the speed controllers gain are demonstrated.

Even though the filter in EAF is designed to improve the speed controller's performance, the conservation principles from Bode integrals means that there is always a limit on the performance of a given system. This fact being established, the next chapters in this work deals with the dead time present in the speed control loop. This emphasis on the dead time makes sense because the distinction between low-frequency and high-frequency resonance is made by the amount of dead time. For a given system with known resonance frequency if the dead time is very small then the first phase crossover frequency is far to the right of the resonance frequency which means the increase in magnitude around the resonance frequency does not influence the gain margin. On the contrary, if the dead time is large enough such that the resonance frequency and the first phase crossover frequency are close to one another (on the frequency scale), then the increase in the magnitude at and around the resonance frequency will influence the gain margin.

Part III.

Non-Minimum Phase Output Tracking

5. Dead Time and its Compensation

5.1. Motivation and introduction

Main goal of AF and EAF was to improve the performance of a DIO suffering from mechanical resonance in particular from inertial-reduction instability. Inertial-reduction instability can be distinguished by the fact that the resonance frequency is below the first phase crossover frequency. The presence of the time delays in combination with the increase in gains at the resonance frequency leads to reduced gain margins, resulting in limited bandwidths. EAF technique was able to improve the performance of the speed controller by manipulating its gain margin, i.e. by manipulating the loop gains around the crossover frequency. On the other hand the gain margin can also be improved by manipulating the phase crossover frequency. The motivation behind the work in Chapters 5 - 7 is to manipulate the phase crossover frequency to achieve the goal of improving the speed controller's performance. Since the main reason for the phase lag to increase beyond -180° is the dead time, first the effects of dead time on the closed loop dynamics are presented in this chapter. Later in the chapter, a well-known technique for dead time compensation namely the Smith predictor is also introduced.

Dead time can be represented by an infinite-dimensional system with the transfer function $e^{-s\tau}$. Controllers involving an infinite-dimensional dead time compensator (DTC) like Smith predictor are typically used for mitigating the dead time. Also finite-dimensional controllers are developed by approximating the dead time by a finite-dimensional rational approximation. Any technique employed to mitigate the dead time should also have a certain degree of robustness to the mismatches in dead time between the actual and designed values. A brief introduction on how the dead time affects the closed-loop dynamics is presented in Section 5.2. The Smith predictor and its robustness with respect to mismatches in dead time is presented in Section 5.3.

5.2. Effects of dead time on closed loop dynamics

5.2.1. Introduction

Consider the unity-feedback loop depicted in Figure 5.1, where P is a plant, C is a controller, r is a reference signal, u is the control signal, and y is a measurable output signal. It is assumed that the measured signal y is delayed by τ. This is reflected in Figure 5.1 by the delay operator denoted by D_τ and defined as

$$D_\tau x(t) = x(t-\tau). \tag{5.1}$$

It is readily seen that D_τ is linear and, whenever τ is constant, is time-invariant and BIBO stable. If given $x(t) \circ\!\!-\!\!\bullet X(s)$, then the *Laplace* transform for the delayed signal, $g(t) := x(t-\tau)$, is given by

$$\begin{aligned} g(t) \circ\!\!-\!\!\bullet G(s) &= \int_0^\infty g(t) \cdot e^{-st} dt \\ &= \int_0^\infty x(t-\tau) \cdot e^{-st} dt \\ &= \int_0^\infty x(T) \cdot e^{-s(T+\tau)} dT, \quad \because \tau \text{ is constant} \\ &= e^{-s\tau} \int_0^\infty x(T) \cdot e^{-sT} dT \\ G(s) &= e^{-s\tau} X(s). \end{aligned} \tag{5.2}$$

Thus the transfer function of the dead time is given by $e^{-s\tau}$.

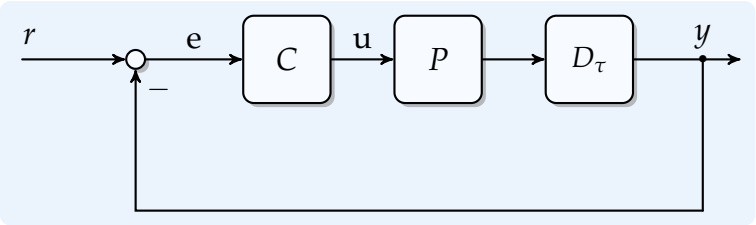

Figure 5.1.: Unity-feedback structure with the plant having output dead time

5.2.2. Effects of loop delays on closed-loop dynamics

This section shows how the presence of loop delays affects the dynamics of the closed-loop control systems. First, the frequency domain properties in connection with the

well known Nyquist stability criterion are considered, then the classical problem of pole placement is presented. At the end, approaches by means of rational approximation of the delay element are presented.

Frequency response and Nyquist stability criterion

Consider the open-loop transfer function of the unity-feedback loop shown in Figure 5.1

$$L(s) = L_r(s)e^{-\tau s},$$

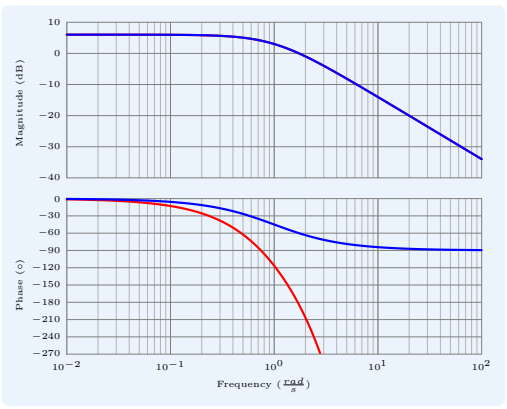

(a) Bode plot

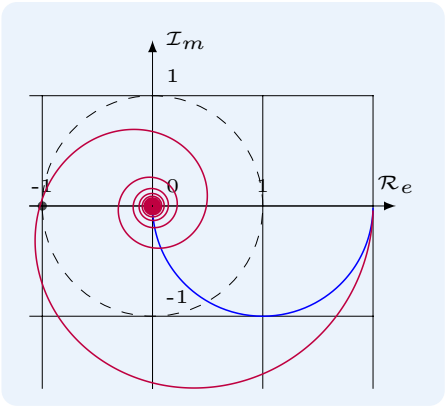

(b) Nyquist diagram

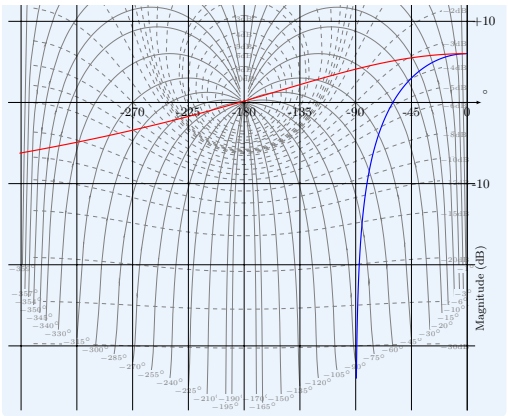

(c) Nichols plot

Figure 5.2.: Frequency response plots of $\frac{2}{(s+1)}$ (blue lines) and $\frac{2}{(s+1)}e^{-1.25s}$(red lines)

where

$$L_r(s) = \mathtt{P}(s)\mathtt{C}(s) \tag{5.3}$$

is assumed to be rational. It is obvious from the frequency response of $L(s)$,

$$L(j\omega) = L_r(j\omega)e^{-j\omega\tau} = |L_r(j\omega)|e^{j\ arg\ L_r(j\omega)}e^{-j\omega\tau} = |L_r(j\omega)|e^{j(arg\ L_r(j\omega)-\omega\tau)} \tag{5.4}$$

that the magnitude of $L(j\omega)$ is not affected by the delay element but, however, additional phase lag is introduced. This phase lag grows linearly with the frequency ω and is proportional to the dead time τ. With these cues the frequency response plots of $L(s)$ can be produced from those of $L_r(s)$ by following simple rules.

Bode plot: the magnitude plot does not change while the phase plot is shifted down by $^{180}/_{\pi\omega\tau}$ degrees at the frequency of $\omega\,{}^{\text{rad}}/_{\text{s}}$.

Nyquist diagram: every point on the diagram of $L_r(s)$ is rotated by $\omega\tau$ radians in clockwise direction.

Nichols chart: every point on the chart is shifted to the left by $\frac{180}{\pi}\omega\tau$ degrees.

Example 5.2.1. Stability analysis of the closed loop system in the presence of loop delays using the Nyquist criterion.

Consider a first order transfer function $L_r(s) = \frac{2}{s+1}$ and a dead time of $\tau = 0.25\,\text{s}$. Using the rules from above, Figure 5.2 depicts the frequency response plots of $L_r(s)$ and $L(s)$.

From the frequency response plots of Figure 5.2 it can be inferred, with the help of Nyquist stability criterion, that the closed-loop system will be unstable with the dead-time, while the system without dead-time is stable. For example, the Nyquist plot of the open-loop transfer function $\frac{2}{s+1}e^{-1.25s}$ shown in Figure 5.2 (b) does encircle the critical point $(-1, 0)$, thus making the corresponding closed-loop system unstable. Moreover it is readily seen from these plots that larger the τ, smaller the stability margins are. Although this is encountered in many practical applications, it is not generic. The following example illustrates such an exception.

Example 5.2.2. Illustration of interlaces stability of closed loop system in the presence of loop delays using the Nyquist criterion [MP05].

Consider the system with $L_r(s) = \dfrac{0.4}{s^2 + 0.1s + 1}$. The Nichols and Nyquist plots of this open-loop transfer function with different delays are presented in Figure 5.3. It is readily seen from both the plots that the closed-loop system is stable for $\tau = 0$ and $\tau = 5$ (blue lines) but is unstable for $\tau = 1$ (red lines). This happens when the phase lag at the first crossover frequency is greater than π and the phase lag at the second crossover frequency is smaller than 3π, i.e. when the resonance peak is between the two critical points and the Nichols plot do not encircle neither of the two critical points. Also in case of the Nyquist diagram it is evident that the plot with $\tau = 1$ encircles the critical point once, making the closed-loop unstable.

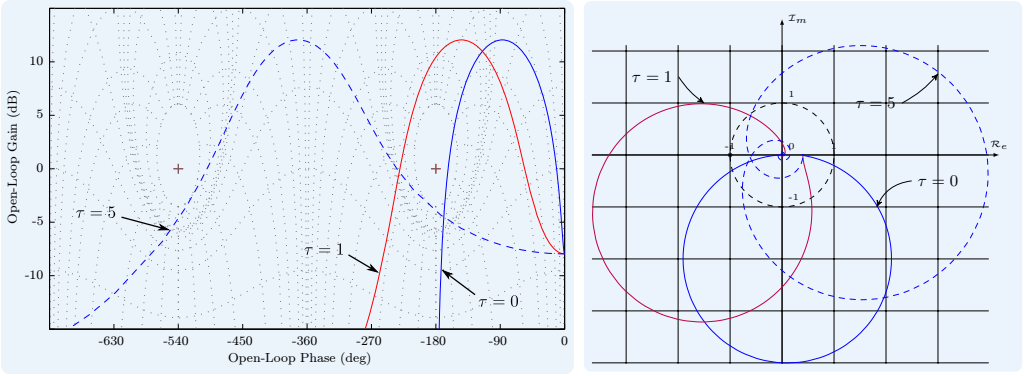

(a) Nichols plot (b) Nyquist diagram

Figure 5.3.: Frequency response plots of $\dfrac{0.4}{s^2 + 0.1s + 1} e^{-\tau s}$.

Pole placement

Adapting the classical pole placement method to systems involving dead-times is considerably more complicated than adapting the Nyquist stability criterion. This complication is easily understood by considering the characteristic polynomial of the closed-loop system given in Figure 5.1

$$\Delta_{CL}(s) = A(s) + B(s)e^{-s\tau}, \tag{5.5}$$

where the polynomials

$$A(s) = s^n + a_{n-1}s^{n-1} + \ldots + a_0 \text{ and } B(s) = b_m s^m + b_{m-1}s^{m-1} + \ldots + b_0$$

are the denominator and the numerator polynomials, respectively, of the open-loop (loop) transfer function $L_r(s)$ given in Equation (5.3). The presence of irrational element due to the dead-time in the characteristic polynomial results in infinite number of roots for every $\tau > 0$. This simple facts makes the pole placement and/or stability study of the closed loop system complicated in comparison to the stability study based on frequency domain as presented in previous section.

Rational approximations of the delay systems

The technical difficulties mentioned above for stability analysis or pole placement for systems involving time delays in continuous time originate from the infinite dimensionality of the delay element $e^{-s\tau}$. Idea here is to approximate the delay element (the system with delay element) by a finite-dimensional system so that the standard analysis and design techniques can be applied. Towards this goal we write the infinite-dimensional time delay as

$$e^{-s\tau} = \frac{e^{-s\tau/2}}{e^{s\tau/2}} \approx \frac{1 - \dfrac{s\tau}{2}}{1 + \dfrac{s\tau}{2}}, \tag{5.6}$$

where approximation is achieved with Taylor series expansion. A better approximation for the irrational exponential function is given by Padé approximant, a detailed discussion of which is presented in [Paro4]. The Padé approximation for the delay element is given as

$$e^{-s\tau} \approx \frac{P_n(-s)}{P_n(s)}, \tag{5.7}$$

where $P_n(s)$ is a stable polynomial of degree n which is the degree of Padé approximation and

$$P_n(s) = \sum_{i=0}^{n} \frac{\tau^i\,(2n-i)!n!}{(2n)!\,(n-i)!i!}\,s^i. \tag{5.8}$$

Thus the first two Padé approximations are given by, $P_1(s) = 1 + \dfrac{s\tau}{2}$ and $P_2(s) = 1 + \dfrac{s\tau}{2} + \dfrac{s^2\tau^2}{12}$.

Any rational approximation of the delay element has only a finite phase lag, where as the phase lag of $e^{-j\omega\tau}$ approaches infinity as ω increases. Thus the approximation makes sense only when considered over a finite frequency range. Figure 5.4 shows the bode plots of the transfer function $L(s) = \frac{2}{s+1}\, e^{-1.25s}$ with different orders of Padé approximations. It can be clearly seen that the Padé approximation of the delay

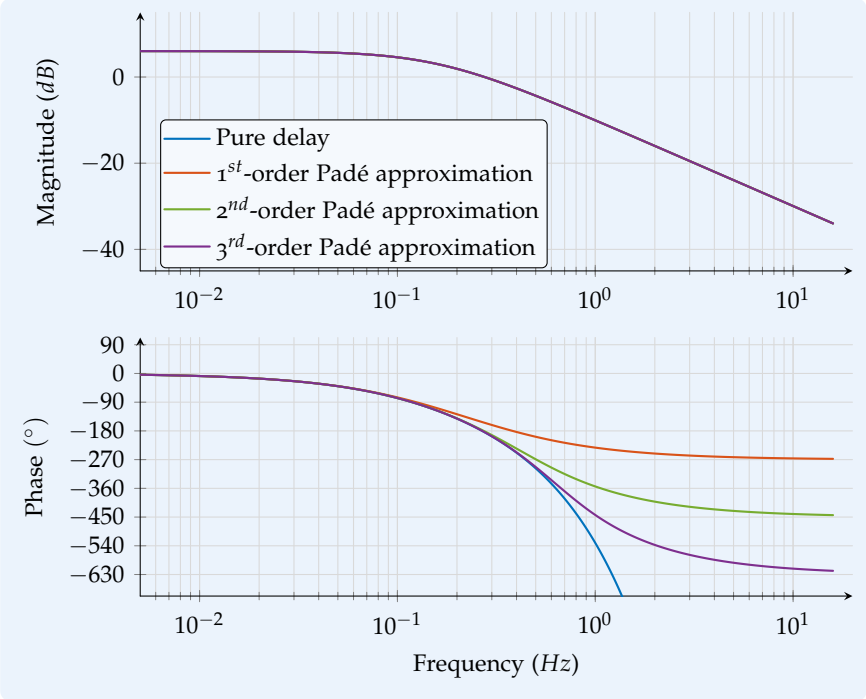

Figure 5.4.: Bode plot showing the influence of Padé approximation on the phase lag.

element of increasing order matches the phase lag from the pure delay within increasing frequency ranges.

5.3. Smith predictor and its robustness against mismatches in dead time

5.3.1. DTC using Smith predictor for SISO system

Smith predictor [Smi57] is a classic example of DTC which uses the infinite-dimensional pure delay element within the controller. It is a well-known method for controlling

systems with a constant loop delay that uses a model of the plant and the delay to control the system as if there were no delay in the loop [ÅH95]. The block diagram of a typical Smith controller is depicted in Figure 5.5, where the controller $C(s)$ (dark blue box) consists of a *primary controller* $\hat{C}(s)$ and an internal feedback of the form

$$\Pi(s) = \hat{P}(s) - \hat{P}(s)e^{-\hat{\tau}s} \tag{5.9}$$

called the *Smith predictor*. $\hat{P}(s)$ is the model of the plant $P(s)$ and similarly $\hat{\tau}$ is an estimate of the dead time τ. The role of DTC can be readily understood by the fact that the signal $v(t)$ contains an estimate of $y(t)$ during the dead time. Therefore the adjusted error, $\tilde{e}(t)$, which is fed into the primary controller carries that part of the error which is directly caused by the primary controller. This eliminated the over-corrections usually associated with conventional controllers when operating on processes with large dead times which require significant reductions in the controller gains and frequently result in poor control performance.

The above qualitative argument are supported analytically by examining the signal $\tilde{e}$. It can be seen that $\tilde{e} = r - P(s)u$ (under the assumption that $\hat{P}(s) = P(s)$ and $\hat{\tau} = \tau$, i.e. no uncertainty in the plant model and dead time.), which means that the loop from u to $\tilde{e}$ does not contain any delay element, i.e. the Smith predictor compensates for the time delay. Writing the closed loop transfer function from r to y

$$T_{y,r}(s) = \frac{Y(s)}{R(s)} = \frac{P\hat{C}}{1 + P\hat{C}}e^{-s\tau}, \tag{5.10}$$

where $Y(s)$ and $R(s)$ are the *Laplace*-transformed signals of $y(t)$, $r(t)$ respectively. It is clear from this transfer function that its characteristic equation is now free of any delay element. This offers a clear advantage, compared to the characteristic polynomial of the closed loop given in Equation (5.5). The controller design with Smith-predictor only considers the *delay-free* plant $P(s)$. The designed controller is implemented by adding the Smith predictor as an internal feedback.

5.3.2. Practical stability of DTC with Smith predictor

When the DTC with Smith predictor is properly designed in the ideal case (complete matching between the true and assumed models) the overall system is asymptotically stable. In certain circumstances the overall system may loose its stability when there are slight changes in the dead time. Systems which are asymptotically stable in the nominal

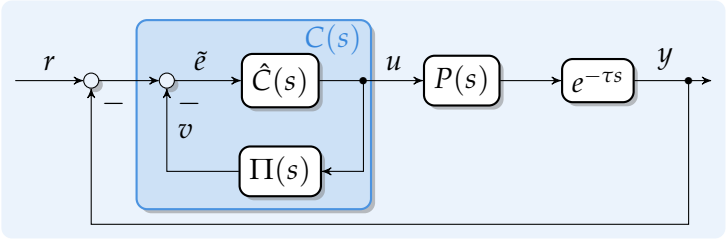

Figure 5.5.: Block diagram showing the dead time compensator using Smith predictor.

case but loose stability for small mismatched between the true and assumed models are called *practically unstable systems*.

We restrict the study of stability here only to mismatches in the dead time, i.e. $\hat{P}(s) = P(s)$. For the system with the DTC controller to be closed-loop practically stable, it is necessary that [Pal80]

$$\lim_{\omega \to \infty} |Q(j\omega)| < \frac{1}{2}, \tag{5.11}$$

where

$$Q(s) = \frac{\hat{C}P}{1 + \hat{C}P}. \tag{5.12}$$

Note that this condition for practical stability does not depend on the dead time. The asymptotic stability in the presence of a mismatch in dead time given by $\Delta\tau := \tau - \hat{\tau}$ is given by the following conditions:

1. A closed loop system is asymptotically stable for any variation $\Delta\tau$ if

$$|Q(j\omega)| < \frac{1}{2} \text{ for all } \omega \geq 0$$

2. There exists a finite positive $(\Delta\tau)_{max}$ such that the closed loop is asymptotically stable for any $|\Delta\tau| < (\Delta\tau)_{max}$ if

$$|Q(j\omega)| \leq 1 \text{ for all } \omega \geq 0 \text{ and } \lim_{\omega \to \infty} |Q(j\omega)| < \frac{1}{2}$$

A conservative estimate for the maximum value of $(\Delta\tau)_{max}$ is given as

$$(\Delta\tau)_{max} = \frac{\pi}{3\omega_s}, \tag{5.13}$$

where ω_s is the frequency above which $|Q(j\omega)| < \frac{1}{2}$.

5.4. Stability of Smith predictor for printing testbench in the presence of dead time mismatch

Consider the plant to be the printing testbench with the parameters as shown in Table 4.1. The controller is once again chosen to be a proportional speed controller as done in Section 4.3.1. A gain of $k_v = 150$ is chosen which is between the benchmarking value and the maximum value achieved using EAF in Section 4.3.2. With these parameters the value of ω_s is equal to 3960 rad/s or 630 Hz, and the corresponding value of $(\Delta\tau)_{max}$ is equal to 0.000265 s. This number is very close to the sample time of the controller, which is equal to the reciprocal of the operating frequency of the servo drive, 0.0002 s. Since the dead time on the printing testbench is estimated using the frequency response measurements, any measurement inaccuracies or unmodeled dynamics will lead to a difference between the estimated and the actual dead time in the plant. As seen from Figure 2.15 the phase response of the measurement is much different from the identified model especially at high frequencies due to unmodeled mechanical components in the drive train.

The dead time is estimated by choosing the frequency at which phase lag is equal to 180°, call it ω_{180°. The total phase lag at this frequency is due to the plant and the dead time. The contribution from the DIO to phase lag, above the resonance frequency, is 90°. Thus the additional 90° of phase lag is only due to the dead time. The phase lag due to pure dead time is given as (from Equation (5.4)),

$$\phi(\omega) = -\omega\tau. \tag{5.14}$$

Using (5.14) the dead time can be approximated as

$$\hat{\tau} = \frac{\pi}{2}\frac{1}{\omega_{180^\circ}}. \tag{5.15}$$

Now, consider τ_a to be the actual dead time in the plant and $\hat{\tau}$ as the measured dead time using (5.15). Since the maximum allowable mismatch in dead time $(\Delta\tau)_{max}$ is known, the worst case allowable mismatch in ω_{180°, represented as $(\Delta\omega)_{180^\circ,max}$ is given as

$$\begin{aligned}(\Delta\omega)_{180^\circ,max} = \omega_{180^\circ,a} - \omega_{180^\circ,m} &= \frac{\pi}{2}\left(\frac{1}{\tau_a} - \frac{1}{\hat{\tau}}\right)\\ (\Delta\omega)_{180^\circ,max} &= \frac{\pi}{2}\left(\frac{\tau_a - \hat{\tau}}{\tau_a\hat{\tau}}\right)\\ &= \frac{\pi}{2}\left(\frac{(\Delta\tau)_{max}}{\tau_a\left(\tau_a + (\Delta\tau)_{max}\right)}\right).\end{aligned} \tag{5.16}$$

In the particular case of printing testbench the value of $(\Delta\omega)_{180^\circ,max}$ is about 37 Hz. This implies any mismatch of 37 Hz and above when calculating the phase crossover frequency from the measurements may affect the closed loop asymptotic stability. This estimate is a very conservative value since the model and actual plant are assumed to be completely matched when calculating this value. Since the measurements are done using a PRBS signal with a limited measurement buffer, the number of frequency points that are calculated from a given measurement are limited. This limitation means that there is always a finite $(\Delta\omega)_{180^\circ}$. Considering these facts, the method of Smith predictor for mitigating the dead time is not further investigated on the printing testbench in this work.

6. Output Tracking for a NMP System

6.1. Introduction

The problem of designing controllers for plants with dead time is complicated because of the irrational models used for the dead time. This is illustrated in Section 5.2.2 using Equation (5.5), where it appears in the denominator of the closed loop system dynamics. One technique to overcome this problem of dealing with irrational transfer functions is to approximate them with a rational transfer function of sufficiently high order. The order of the approximation directly influences the bandwidth over which the rational approximation is valid when compared to the pure delay.

In this thesis, a rational approximation for the dead time with the help of Padé approximant is used. The plant transfer function is extended to consider this rational approximation. This extended plant description has a non-minimum phase nature. This chapter considers the problem of output tracking for such a non-minimum phase plant. First the output tracking problem is reformulated as a state tracking problem by defining state reference profiles calculated using the so-called stable system center technique. Then a robust state tracking controller is designed which ultimately results in the output tracking.

This chapter is organized as follows: Section 6.2 introduces the NMP systems and the concept of internal dynamics which characterize a NMP system in state-space. The Padé approximation for the dead time and the resulting non-minimum phase representation are presented in Section 6.3. The non trivial nature of output tracking for a non-minimum phase systems and the advantages of considering state tracking against output tracking are given in Section 6.4. Section 6.5 presents a technique for calculating the state reference profiles, namely the stable system center technique. Finally, Section 6.6 presents a state tracking controller for the NMP system which results in output tracking.

6.2. Non-minimum phase systems

Consider two transfer functions

$$G_1(s) = \frac{s-z}{s+p} \quad \text{and} \quad G_2(s) = \frac{s+z}{s+p},$$

with their poles and zeros as plotted in Figure 6.1. $G_1(s)$ has one zero $s = z$, $z > 0$ in the open right half-plane. $G_2(s)$ is obtained by reflecting this zero into the left half-plane. Now if the gains and phases of $G_1(s)$ and $G_2(s)$ are compared, then the vector from zero z to any point on the $j\omega$-axis and from zero $-z$ to the same point have the same length, i.e.

$$|G_1(j\omega)| = |G_2(j\omega)|$$

for all $\omega \geq 0$. Although they have the same gain behavior, their phases are quite different. From Figure 6.1,

$$\angle G_1(j\omega) = \theta_1 - \phi \quad \angle G_2(j\omega) = \theta_2 - \phi.$$

and in general $\angle G_1(j\omega) \geq \angle G_2(j\omega)$ for all $\omega \geq 0$. Thus, if a transfer function has right half-plane zeros, reflecting these zeros into the left half-plane gives a transfer function with the same amplitude but a smaller phase[1] than the original transfer function. This motivates the definition of minimum and non-minimum phase systems. A proper rational transfer function is called a *minimum-phase* transfer function if all its zeros lie inside the open left half s-plane, otherwise it is called a *non-minimum phase* transfer function and the corresponding zero as the *non-minimum phase zero*.

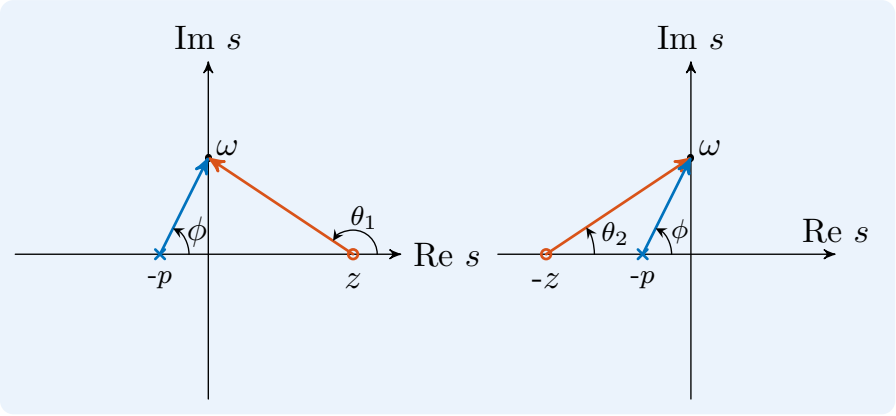

Figure 6.1.: Non-minimum phase transfer function

[1] smaller in terms of absolute value

Given a stable, proper transfer function $P(s)$ with one zero at $s = \alpha,\ \alpha > 0$ the following representation is possible

$$P(s) = P_0(s)\frac{\left(1 - \frac{s}{\alpha}\right)}{\left(1 + \frac{s}{\alpha}\right)}.$$

The transfer function $P_0(s)$ has poles and zeros with negative real part only. The BIBO stable transfer function

$$A(s) = \frac{\left(1 - \frac{s}{\alpha}\right)}{\left(1 + \frac{s}{\alpha}\right)}$$

is the so-called *All-pass filter*, the gain of which is $|A(j\omega)| = 1,\ \forall\omega$. The phase behavior of $A(s)$ is non trivial and depends on its order[2], and for a first order All-pass filter the response is shown in Figure 6.2. Given a standard control loop with $C(s)$ denoting the controller transfer function, the open loop transfer function given by $L(s) = C(s)P(s)$ can also be split into an All-pass and a transfer function with stable poles and zeros.

$$L(s) = L_0(s)A(s),$$

where $L_0(s) = C(s)P_0(s)$. Due to the additional phase lag from the non-minimum phase zero the stability margins of the open loop transfer function are altered. Thus the non-minimum phase zeros may render an otherwise stable control loop unstable.

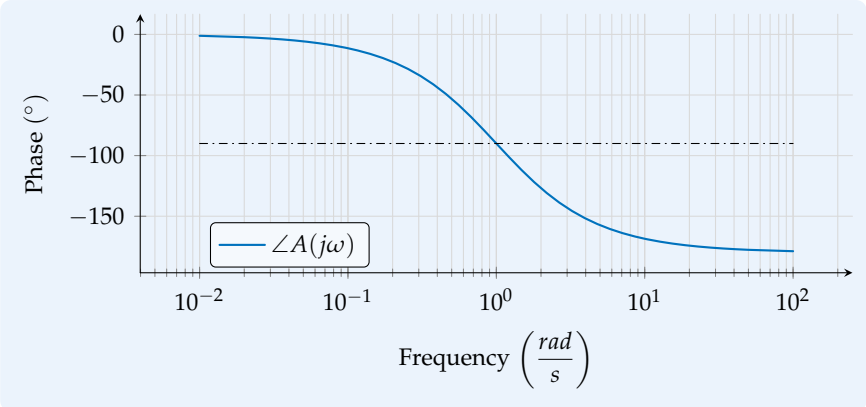

Figure 6.2.: Phase behaviour of $A(s)$

[2]The order of $A(s)$ is equal to the number of zeros of $P(s)$ with positive real part.

6.2.1. Non-minimum phase system and internal dynamics

Non-minimum phase systems can also be recognized from the state space representation when it is transformed into the so-called Byrnes-Isidori normal form [BI88; BI91]. Consider a system represented by the transfer function

$$G(s) = \frac{\beta_0 + \beta_1 s + \ldots + \beta_{m-1} s^{m-1} + s^m}{\alpha_0 + \alpha_1 s + \ldots + \alpha_{n-1} s^{n-1} + s^n}, \tag{6.1}$$

where $\alpha_0, \alpha_1, \ldots, \alpha_{n-1}$, $\beta_0, \beta_1, \ldots, \beta_{m-1}$ are constant coefficients. It is also assumed that the numerator and denominator are co-prime polynomials and that $n \geq m$. A minimal state-space realization (both controllable and observable) of $G(s)$ is given as

$$\dot{\mathbf{x}}(t) = \underbrace{\begin{bmatrix} 0 & 1 & 0 & \ldots & 0 \\ 0 & 0 & 1 & \ddots & 0 \\ \vdots & \vdots & & \ddots & \vdots \\ 0 & 0 & 0 & \ldots & 1 \\ -\alpha_0 & -\alpha_1 & -\alpha_2 & \ldots & -\alpha_{n-1} \end{bmatrix}}_{\mathbf{A}} \mathbf{x} + \underbrace{\begin{bmatrix} 0 \\ 0 \\ \vdots \\ 0 \\ 1 \end{bmatrix}}_{\mathbf{b}} u(t) \tag{6.2a}$$

$$y(t) = \underbrace{\begin{bmatrix} \beta_0 & \beta_1 & \ldots & \beta_{m-1} & 1 & 0 & \ldots & 0 \end{bmatrix}}_{\mathbf{c}^T} \mathbf{x}. \tag{6.2b}$$

In order to transform this state space representation into the Byrnes-Isidori normal form, the following $n \times n$ nonsingular state transformation [Svao6] is used

$$\mathbf{T} = \underbrace{\begin{bmatrix} & \mathbf{c}^T & \\ & \mathbf{c}^T\mathbf{A} & \\ & \vdots & \\ & \mathbf{c}^T\mathbf{A}^{n-m-1} & \\ 1 & & 0 \\ & \ddots & & \ddots \\ & & 1 & & 0 \end{bmatrix}}_{\begin{matrix} m & n-m \end{matrix}} \Bigg\} m, \tag{6.3}$$

where $n - m$ represents the so-called *relative degree*[3] of the system. The resulting state vector in the new coordinates $\mathbf{z}(t) = \mathbf{T}\mathbf{x}(t)$, is partitioned as

$$\mathbf{z}(t) = \begin{bmatrix} \boldsymbol{\xi}(t) \\ \boldsymbol{\eta}(t) \end{bmatrix}, \tag{6.4}$$

with

$$\boldsymbol{\xi}(t) = \begin{bmatrix} \xi_1(t) \\ \xi_2(t) \\ \vdots \\ \xi_{n-m}(t) \end{bmatrix} = \begin{bmatrix} z_1(t) \\ z_2(t) \\ \vdots \\ z_{n-m} \end{bmatrix} = \begin{bmatrix} y(t) \\ \dot{y}(t) \\ \vdots \\ y^{(n-m-1)}(t) \end{bmatrix} \tag{6.5}$$

and

$$\boldsymbol{\eta}(t) = \begin{bmatrix} \eta_1(t) \\ \eta_2(t) \\ \vdots \\ \eta_m(t) \end{bmatrix} = \begin{bmatrix} z_{n-m+1}(t) \\ z_{n-m+2}(t) \\ \vdots \\ z_n(t) \end{bmatrix} = \begin{bmatrix} x_1(t) \\ x_2(t) \\ \vdots \\ x_m(t) \end{bmatrix} \tag{6.6}$$

to get the *Byrnes-Isidori normal* form given as

$$\dot{\xi}_1(t) = \xi_2(t) \tag{6.7a}$$

$$\dot{\xi}_2(t) = \xi_3(t) \tag{6.7b}$$

$$\vdots$$

$$\dot{\xi}_{n-m-1}(t) = \xi_{n-m} \tag{6.7c}$$

$$\dot{\xi}_{n-m}(t) = \mathbf{a}^T\mathbf{z} + b_2'u \tag{6.7d}$$

$$\dot{\boldsymbol{\eta}}(t) = \mathbf{P}\boldsymbol{\xi} + \mathbf{Q}\boldsymbol{\eta}, \tag{6.7e}$$

[3]Refer to Section C.4

where $\mathbf{a}^T = \mathbf{c}^T\mathbf{A}^{n-m}\mathbf{T}^{-1}$, $b_2' = \mathbf{c}^T\mathbf{A}^{n-m-1}\mathbf{b}$, $\mathbf{P} \in \mathbb{R}^{m\times(n-m)}$, $\mathbf{Q} \in \mathbb{R}^{m\times m}$ and

$$[\mathbf{P} \quad \mathbf{Q}] = \begin{bmatrix} \underbrace{\begin{matrix} 1 & & \\ & \ddots & \\ & & 1 \end{matrix}}_{m} & \underbrace{\begin{matrix} 0 & & \\ & \ddots & \\ & & 0 \end{matrix}}_{n-m} \end{bmatrix} \mathbf{A}\mathbf{T}^{-1}. \tag{6.8}$$

As seen from (6.5) and (6.7), $\boldsymbol{\xi}(t) \in \mathbb{R}^{n-m}$ describes the *input-output dynamics* whereas $\boldsymbol{\eta}(t) \in \mathbb{R}^m$ describes the so-called *internal dynamics*, so named as they are the unobservable part of the dynamics.

The system dynamics in Byrnes-Isidori normal form given by (6.7) reduces to the so-called *zero dynamics* [Isi95] when the output $y(t)$ and all its higher derivatives are set identically to zero $\forall t \geq 0$ by proper choice of input and initial conditions. For the system considered above, the zero dynamics are given as

$$\dot{\boldsymbol{\eta}}(t) = \mathbf{Q}\boldsymbol{\eta}(t). \tag{6.9}$$

From (6.6) the dynamics of the internal state are given as (using (6.2))

$$\begin{aligned} \dot{\eta}_1 &= \dot{x}_1 = x_2 \\ \dot{\eta}_2 &= \dot{x}_2 = x_3 \\ &\vdots \quad \vdots \\ \dot{\eta}_m &= \dot{x}_m = x_{m+1}. \end{aligned} \tag{6.10}$$

Using the output equation in (6.2)

$$y(t) = \beta_0 x_1 + \beta_1 x_2 + \ldots + \beta_{m-1} x_m + x_{m+1}, \tag{6.11}$$

and due to the definition of zero dynamics $y(t) = 0$, so

$$x_{m+1} = -\beta_0 x_1 - \beta_1 x_2 - \ldots - \beta_{m-1} x_m. \tag{6.12}$$

using (6.12) and (6.10) the matrix $\mathbf{Q}$ in (6.9) is given as

$$\mathbf{Q} = \begin{bmatrix} 0 & 1 & 0 & \ldots & 0 \\ 0 & 0 & 1 & \ldots & 0 \\ \vdots & \vdots & \vdots & \ddots & \vdots \\ -\beta_0 & -\beta_1 & -\beta_2 & \ldots & -\beta_{m-1} \end{bmatrix}. \tag{6.13}$$

The characteristic polynomial of the matrix $\mathbf{Q}$ in (6.13) is

$$\Delta(s) = s^m + \beta_{m-1}s^{m-1} + \ldots + \beta_1 s + \beta_0, \tag{6.14}$$

and this polynomial is same as the numerator polynomial of the system transfer function given in (6.1). So the eigenvalues of $\mathbf{Q}$ coincide with the zeros of the transfer function, i.e. the stability of internal dynamics depends on the zeros of the transfer function. Thus the internal dynamics of a non-minimum phase system are unstable.

6.3. Representation of dead-time using NMP system

Consider the case where a signal $y(t)$ is measured using a device which introduces a delay of τ seconds. Thus the measured signal $y_m(t)$ in the *laplacian* domain is represented as

$$\mathscr{L}\{y_m(t)\} = Y_m(s) = Y(s)e^{-s\tau} \approx Y(s)\frac{\left(1-\frac{s\tau}{2}\right)}{\left(1+\frac{s\tau}{2}\right)}, \tag{6.15}$$

where the last rational transfer function is the first order Padé approximation for the dead time (cf. Equation (5.6)). A new output variable $\check{Y}_m(s)$[4] is introduced to make this approximation exact. Thus

$$\check{Y}_m(s) = \left(\frac{1-\frac{s\tau}{2}}{1+\frac{s\tau}{2}}\right) Y(s)$$

$$\check{Y}_m(s)\left(1+\frac{s\tau}{2}\right) = Y(s)\left(1-\frac{s\tau}{2}\right).$$

Transforming back into time domain yields

$$\check{y}_m + \dot{\check{y}}_m\frac{\tau}{2} = y - \dot{y}\frac{\tau}{2}. \tag{6.16}$$

Introducing the new state variable $\zeta := \check{y}_m + y$ Equation (6.16) reads as

$$\dot{\zeta} = \frac{2}{\tau}\zeta - \frac{4}{\tau}\check{y}_m. \tag{6.17}$$

[4] *Laplace* transform of $\check{y}_m(t)$ is $\check{Y}_m(s)$

One can readily see that the homogeneous part of the above differential equation, considering $\check{y}_m$ as the input, is unstable and that the stability characteristics of this differential equation is influenced by the non-minimum phase zero in the transfer function (6.15). Any arbitrary order Padé approximation of the time delay contributes at least one non-minimum phase zero to the transfer function of the system, thus any plant with output/input delay can be approximated by a non-minimum phase system of a sufficient order.

6.4. Output tracking for a non-minimum phase system

As shown in the previous section, a plant with output delay can be represented as a non-minimum phase system by approximating the dead time as a rational function with the help of Padé approximation. This section considers the problem of output tracking for such a non-minimum phase system.

6.4.1. Introduction and literature review

It is well known that zeros cannot be moved with the help of feedback while the poles can be arbitrarily placed when the given system is controllable [Won79]. The presence of unstable zeros lead to internal stability issues. Solvability of the output tracking problem, considering that the reference profile is generated from an exo-system, is related to some conditions on the transmission zeros of a combination of the given system and the exo-system [Hua04, Chap. 1]. In particular, the presence of right half-plane transmission zeros impose limitations on the tracking. In the case of nonlinear systems the NMP nature of the plant restricts the application of powerful nonlinear control techniques such as feedback linearizion [MK93] and sliding mode control.

Two classical techniques for output tracking are inversion and output regulation. The inversion based techniques provides exact output tracking but leads to internal stability issues in case of non-minimum phase systems, because of the unstable zeros. Stable system inversion in the coordinates of the Byrnes-Isidori normal form is proposed in [DCP96; CP96; ZD04]. The main idea is to apply reverse-time integration of the unstable internal dynamics. This however, results in reference trajectories that are noncausal.

The output regulation theory developed in [IB90] ensured asymptotic output tracking and internal stability for a class of nonlinear systems with reference trajectories generated

by an exo-system. The control law proposed in [IB90] uses feedback stabilisation of a certain state trajectory calculated as the solution of nonlinear partial differential equations which is not always easy. Approximate solutions to this partial differential equation are proposed in [GK93]. Control of NMP systems via sliding mode control was also first studied in this paper. Gopalswamy and Hedrick identified a particular solution of the internal dynamics that is acceptable (ideal internal dynamics) and used an output redefinition technique to make these ideal internal dynamics attractive. The central idea was to use the input to control robustly (against matched perturbations) the modified output and use this controlled output to stabilize the internal dynamics.

Before proceeding to the discussion about the problems with output tracking in the case of a NMP system, the stabilization problem is first considered.

Example 6.4.1. (Problem of stabilizing a NMP system) Consider the following LTI-SISO system

$$\begin{bmatrix} \dot{x}_1 \\ \dot{x}_2 \\ \dot{x}_3 \end{bmatrix} = \begin{bmatrix} 0 & 0 & 1 \\ 0 & -1 & 1 \\ 0 & 4 & -1.2 \end{bmatrix} \begin{bmatrix} x_1 \\ x_2 \\ x_3 \end{bmatrix} + \begin{bmatrix} 0 \\ -0.2 \\ -20 \end{bmatrix} u, \tag{6.18}$$

and the output is given as

$$y = x_1 - x_2. \tag{6.19}$$

The given system is completely controllable and is open-loop unstable with the eigenvalues at $\{0, -3.1, 0.9\}$. The input-output transfer function is given as

$$G(s) = \frac{Y(s)}{U(s)} = \frac{0.2\,(s + 10.816)\,(s - 9.616)}{s(s + 3.102)(s - 0.902)}. \tag{6.20}$$

It is clear from the transfer function that the given system has a NMP-zero at $s = 9.616$. The input-output (I/O) dynamics are of order one (i.e. the relative degree is one) and are given as

$$\dot{y} = -y + x_1 + 0.2u \tag{6.21}$$

and the residual dynamics of order two which are not directly involved in the I/O relation are given as

$$\begin{bmatrix} \dot{x}_1 \\ \dot{x}_3 \end{bmatrix} = \begin{bmatrix} 0 & 1 \\ 4 & -1.2 \end{bmatrix} \begin{bmatrix} x_1 \\ x_3 \end{bmatrix} + \begin{bmatrix} 0 \\ 1 \end{bmatrix} (-4y - 20u). \tag{6.22}$$

Consider the output stabilization problem using sliding mode control method. For the system (6.21), the sliding surface is introduced as $\sigma = y = 0$, and the equivalent control providing the system motion on the sliding surface is identified from (6.21) and (6.22) as

$$u = u_{eq} = -5x_1. \tag{6.23}$$

The sliding mode dynamics on the surface $\sigma = 0$ are given as

$$\begin{bmatrix} \dot{x}_1 \\ \dot{x}_3 \end{bmatrix} = \begin{bmatrix} 0 & 1 \\ 104 & -1.2 \end{bmatrix} \begin{bmatrix} x_1 \\ x_3 \end{bmatrix}. \tag{6.24}$$

The dynamics described by (6.24) are the zero dynamics and they are unstable as the eigenvalues are $\{-10.816, 9.616\}$. The instability of the zero dynamics causes the equivalent control (6.23) to grow unbounded resulting in the loss of internal stability. ▲

6.4.2. Problem formulation

The following LTI SISO plant is considered

$$\dot{\mathbf{x}} = \mathbf{A}\mathbf{x} + \mathbf{b}u, \quad y = \mathbf{c}^T\mathbf{x}, \tag{6.25}$$

where $\mathbf{x} \in \mathbb{R}^n$ and $y \in \mathbb{R}$ are state vector and the controlled output respectively, $u \in \mathbb{R}$ is the control input. $\mathbf{A} \in \mathbb{R}^{n\times n}, \mathbf{b}, \mathbf{c} \in \mathbb{R}^n$ are system matrix and input, output vectors respectively. $(\mathbf{A}, \mathbf{b})$ is a controllable pair and $(\mathbf{A}, \mathbf{c})$ is an observable one. Consider the change of coordinates using (6.3) which brings the system into Byrnes-Isidori normal form given as

$$\dot{\boldsymbol{\xi}}(t) = \mathbf{R}\boldsymbol{\xi} + \mathbf{S}\boldsymbol{\eta} + \mathbf{b}_2 u \tag{6.26a}$$

$$\dot{\boldsymbol{\eta}}(t) = \mathbf{P}\boldsymbol{\xi} + \mathbf{Q}\boldsymbol{\eta}, \tag{6.26b}$$

where the terms $\mathbf{R}, \mathbf{S}$ and $\mathbf{P}, \mathbf{Q}$ are as defined in (6.29) and (6.8), and $\mathbf{b}_2 = \begin{bmatrix} 0 & 0 & \dots & b_2' \end{bmatrix}^T$. It is assumed that both the states $\boldsymbol{\xi}$, $\boldsymbol{\eta}$ can be measured/estimated. The plant is assumed to be a non-minimum phase system, meaning the zero dynamics are unstable, i.e. $\mathbf{Q}$ is non-Hurwitz.

Given a smooth output reference profile, $y_c(t) \in \mathbb{R}$ (assumed to be generated by a known exosystem of known order), the problem is to design an output tracking controller.

This controller should be able to drive the tracking error $e_y := y_c(t) - y(t)$ to zero asymptotically in the presence of system model uncertainties while maintaining the internal stability. The characteristic polynomial of the linear time-invariant exosystem generating the smooth output reference profile is assumed to be given by

$$\Delta_k(s) = s^k + \rho_{k-1}s^{k-1} + \ldots + \rho_1 s + \rho_0, \tag{6.27}$$

where k is the order of the exosystem and $\rho_0, \rho_1, \ldots, \rho_{k-1}$ are non-negative real numbers.

6.4.3. Reformulation of the output tracking problem as a state tracking problem

Any controller that deals with the task of output tracking of a nonminimum-phase system has to ensure the internal dynamics are stable. In the case of a non-minimum phase system the internal dynamics are unstable and so they have to be stabilized explicitly by feedback. For this purpose a state-feedback controller is designed. The considered output tracking problem can be reformulated as a state-tracking problem by calculating the state reference trajectories (for both external and internal dynamics). If these reference trajectories are identified such that the state-tracking asymptotically yields output tracking for any reference profile, then the state-tracking problem can be solved using conventional SMC techniques.

For obtaining the state-reference trajectories, dynamic inversion of the plant can be used. But, for a nonminimum-phase system this inverse is unstable. As mentioned in Section 6.4.1, a bounded reference trajectory for the internal state $\boldsymbol{\eta}_c \in \mathbb{R}^m$ can be calculated as the solution to a partial differential algebraic equation of the center manifold [IB90]. A method to get a bounded solution to the unstable internal dynamics (6.26b) driven by $y_c(t)$ (reference output trajectory) asymptotically is the so-called *stable system center technique* [SS02].

6.5. State reference profile generation via stable system center approach

6.5.1. System center

The output tracking problem of non-minimum phase system (6.7) is considered here. For the sake of convenience, system (6.7) which is already in the Byrnes-Isidori normal form is rearranged, such that it is as well in the *regular form*[5] [UGS99], as

$$\dot{\boldsymbol{\eta}} = \mathbf{Q}\boldsymbol{\eta} + \mathbf{P}\boldsymbol{\xi} \tag{6.28a}$$

$$\dot{\boldsymbol{\xi}} = \mathbf{S}\boldsymbol{\eta} + \mathbf{R}\boldsymbol{\xi} + \mathbf{b}_2 u, \tag{6.28b}$$

where

$$\begin{bmatrix} \mathbf{R} & \mathbf{S} \end{bmatrix}_{(n-m)\times n} = \begin{bmatrix} \overbrace{\begin{matrix} 0 & 1 & 0 & \dots & 0 \end{matrix}}^{n-m} & \overbrace{\begin{matrix} 0 & \dots & 0 \end{matrix}}^{m} \\ \begin{matrix} 0 & 0 & 1 & \dots & 0 \end{matrix} & \begin{matrix} 0 & \dots & 0 \end{matrix} \\ \begin{matrix} \vdots & \vdots & \vdots & \ddots & \vdots \end{matrix} & \begin{matrix} \vdots & \ddots & \vdots \end{matrix} \\ \begin{matrix} 0 & 0 & 0 & \dots & 1 \end{matrix} & \begin{matrix} 0 & \dots & 0 \end{matrix} \\ \multicolumn{2}{c}{\mathbf{c}^T\mathbf{A}^{n-m}\mathbf{T}^{-1}} \end{bmatrix}, \tag{6.29a}$$

$$\mathbf{b}_2 = \begin{bmatrix} 0 & 0 & \dots & \mathbf{c}^T\mathbf{A}^{n-m-1}\mathbf{b} \end{bmatrix}^T, \qquad \mathbf{b}_2 \in \mathbb{R}^{(n-m)} \tag{6.29b}$$

and $\mathbf{P}, \mathbf{Q}$ are as defined in (6.8).

As mentioned in Section 6.4.2 the output reference profile $y_c(t)$ is assumed to be generated from a known exosystem. First, the state reference profile $\boldsymbol{\xi}_c(t)$ for the state $\boldsymbol{\xi}(t)$ is calculated using Equation (6.5). Then, according to relation (6.28a) the state reference profile for the internal state, represented by $\boldsymbol{\eta}_c(t)$, should satisfy the differential equation

$$\dot{\boldsymbol{\eta}}_c = \mathbf{P}\boldsymbol{\xi}_c + \mathbf{Q}\boldsymbol{\eta}_c. \tag{6.30}$$

[5] useful for the design of sliding mode controller

The internal dynamics (ID) in reference coordinates can be written as

$$\dot{\boldsymbol{\eta}}_c(t) = \mathbf{P}\boldsymbol{\xi}_c + \mathbf{Q}\boldsymbol{\eta}_c \tag{6.31a}$$

$$y_c(t) = \begin{bmatrix} 1 & 0 & \dots & 0 \end{bmatrix} \boldsymbol{\xi}_c + \mathbf{0}_{(1\times m)}\boldsymbol{\eta}_c. \tag{6.31b}$$

This linear system of differential-algebraic equation (DAE) is named as *the system center* [Sht97]. The state reference profiles can be extracted by solving the system center. The existence of solution for the DAE is guaranteed (shown in the following Section 6.5.2) by the observability assumption for the given system.

6.5.2. Existence of solutions to the system center

Consider the system center given in (6.31)

$$\dot{\boldsymbol{\eta}}_c(t) = \mathbf{P}\boldsymbol{\xi}_c + \mathbf{Q}\boldsymbol{\eta}_c \tag{6.32a}$$

$$y_c(t) = \mathbf{e}_1^T\boldsymbol{\xi}_c + \mathbf{0}_{(1\times m)}\boldsymbol{\eta}_c, \tag{6.32b}$$

where $\mathbf{e}_1^T$ is the standard basis unit vector. This is rewritten as

$$\underbrace{\begin{bmatrix} \mathbf{0} & \mathbf{0} \\ \mathbf{0} & \mathbf{I}_{m\times m} \end{bmatrix}}_{=:\mathbf{E}_d} \begin{bmatrix} \dot{\boldsymbol{\xi}}_c \\ \dot{\boldsymbol{\eta}}_c \end{bmatrix} = \underbrace{\begin{bmatrix} \mathbf{e}_1^T \\ \mathbf{P} \quad \mathbf{Q} \end{bmatrix}}_{=:\mathbf{A}_d} \begin{bmatrix} \boldsymbol{\xi}_c \\ \boldsymbol{\eta}_c \end{bmatrix} + \underbrace{\begin{bmatrix} -y_c(t) \\ \mathbf{0} \end{bmatrix}}_{=:\mathbf{f}(t)}, \tag{6.33}$$

where $\mathbf{P} \in \mathbb{R}^{m\times n-m}$, $\mathbf{Q} \in \mathbb{R}^{m\times m}$ and $\mathbf{A}_d \in \mathbb{R}^{(m+1)\times n}$. Equation (6.33) is in the standard form of linear differential-algebraic equations with constant coefficients (cf. (2.1) in [KM06]). According to [KM06], a given DAE is solvable for a given smooth inhomogeneity $\mathbf{f}(t)$ if and only if the matrix pair $(\mathbf{E}_d, \mathbf{A}_d)$ is regular. The matrix pair $(\mathbf{E}_d, \mathbf{A}_d)$ is called regular if both the matrices $\mathbf{A}_d, \mathbf{E}_d$ are square and the so-called *characteristic polynomial* $p(s)$ defined by

$$p(s) = \det(s\mathbf{E}_d - \mathbf{A}_d) \tag{6.34}$$

is not the zero polynomial. In our case the matrices are not square, so we consider the other states of $\boldsymbol{\xi}_c(t)$ as in (6.5) to extend the algebraic constraint of the system center

as

$$\mathbf{0}\,\dot{\boldsymbol{\xi}}_c = \mathbf{I}_{(n-m)}\boldsymbol{\xi}_c + \begin{bmatrix} -y_c(t) \\ -\dot{y}_c(t) \\ -\ddot{y}_c(t) \\ \vdots \\ -y_c^{(n-m-1)}(t) \end{bmatrix}. \tag{6.35}$$

Due to the special structure of the considered system (minimal realization) and the transformation matrix $\mathbf{T}$ from (6.3), the matrix $\mathbf{P}$ is reduced to

$$\mathbf{P}_{(m\times n-m)} = \begin{bmatrix} 0 & 0 & \dots & 0 \\ 0 & 0 & \dots & 0 \\ \vdots & \vdots & \ddots & \vdots \\ 1 & 0 & \dots & 0 \end{bmatrix}. \tag{6.36}$$

Now using Equation (6.9), the new DAE is given as

$$\underbrace{\begin{bmatrix} \mathbf{0} & \mathbf{0} \\ \mathbf{0} & \mathbf{I}_{m\times m} \end{bmatrix}}_{\mathbf{E}_{d,r}} \begin{bmatrix} \dot{\boldsymbol{\xi}}_c \\ \dot{\boldsymbol{\eta}}_c \end{bmatrix} = \underbrace{\begin{bmatrix} 1 & 0 & \dots & 0 & 0 & \dots & \dots & \dots & 0 \\ 0 & 1 & \dots & 0 & 0 & \dots & \dots & \dots & 0 \\ \vdots & \vdots & \ddots & \vdots & \vdots & & \ddots & & \vdots \\ 0 & 0 & \dots & 1 & 0 & \dots & \dots & \dots & 0 \\ 0 & 0 & \dots & 0 & 0 & 1 & 0 & \dots & 0 \\ 0 & 0 & \dots & 0 & 0 & 0 & 1 & \dots & 0 \\ \vdots & \vdots & \ddots & \vdots & \vdots & \vdots & \vdots & \ddots & \vdots \\ 0 & 0 & \dots & 0 & 0 & 0 & 0 & \dots & 1 \\ 1 & 0 & \dots & 0 & -\beta_0 & -\beta_1 & -\beta_2 & \dots & -\beta_{m-1} \end{bmatrix}}_{\mathbf{A}_{d,r}} \begin{bmatrix} \boldsymbol{\xi}_c \\ \boldsymbol{\eta}_c \end{bmatrix} + \underbrace{\begin{bmatrix} -y_c(t) & -\dot{y}_c(t) & -\ddot{y}_c(t) & \dots & -y_c^{(n-m-1)}(t) & 0 & 0 & \dots & 0 \end{bmatrix}^T}_{\mathbf{f}_r(t)}. \tag{6.37}$$

Using the assumption on the input reference profile, $\mathbf{f}_r(t)$ can be considered smooth, and now additionally the matrices, $\mathbf{E}_{d,r}$ and $\mathbf{A}_{d,r}$ are square. Thus we check if the characteristic polynomial $p(s) = \det(s\mathbf{E}_{d,r} - \mathbf{A}_{d,r})$ is a zero polynomial. As can be seen from Equation (6.37) $\mathbf{A}_{d,r}$ has full rank (because $\beta_0 \neq 0$) implying that the characteristic

polynomial $p(s)$ is not a zero polynomial which, further implies that the considered matrix pair $(\mathbf{E}_{d,r}, \mathbf{A}_{d,r})$ is regular. Thus a solution to the DAE given in Equation (6.37) exists.

The regularity of the matrix pair is closely related to the choice of state transformation matrix given in (6.3), as the structure of the matrix $\mathbf{A}_{d,r}$ depends on the choice of matrix $\mathbf{T}$. This matrix is only invertible when it has full rank. The last m rows of $\mathbf{T}$ are linearly independent and the first $(n-m)$ rows are same as the rows of the observability matrix for the system (6.1) (as defined in [Kal59]). Since the original system in (6.2) is assumed to be observable these rows are linearly independent. Thus, the observability of the considered system results in an invertible transformation matrix $\mathbf{T}$ as given in (6.3). In conclusion, the existence of solutions to the DAE in (6.37) according to [BCP95, Theorem 2.3.1] depends on the regularity of the matrix pair $(\mathbf{E}_{d,r}, \mathbf{A}_{d,r})$ which in turn depends on the observability of the considered system.

6.5.3. Stable system center approach

The system center describing the dynamics of the internal state reference profile $\boldsymbol{\eta}_c(t)$ is given in Section 6.5.1 and the existence of solutions to this system center is established in the previous section. Different techniques to solve a given DAE are presented in literature for example [BCP95; KM06]. Due to the NMP nature of the problem, the matrix $\mathbf{Q}$ from Equation (6.9) is non-Hurwitz rendering the system center described by (6.31) unstable. Thus a direct integration of this unstable system center will result in an unbounded reference signal for the internal states $\boldsymbol{\eta}_c(t)$ demanding an unbounded input signal for asymptotic tracking.

A method to generate a stable system center (SSC) which provides output tracking in systems with linear unstable internal dynamics is developed in [SS01]. The key idea is to use a dynamic extension of the system center that achieves a stable system center from which the bounded state reference profiles are calculated. Subsequent stabilization of the state tracking-error results in the output tracking of the original system. To this end the bounded $\boldsymbol{\eta}^*(t)$, which asymptotically approaches $\boldsymbol{\eta}_c(t)$, is selected as a solution of the equation

$$\dot{\boldsymbol{\eta}}^*(t) = \boldsymbol{\theta}_c(t) + \mathbf{Q}\boldsymbol{\eta}^*(t) - \mathbf{g}^*(t) \tag{6.38}$$

where the term $\boldsymbol{\theta}_c$ is given as

$$\boldsymbol{\theta}_c(t) = \mathbf{P}\boldsymbol{\xi}_c(t), \tag{6.39}$$

and the dynamics of the term $\mathbf{g}^*(t)$ are chosen such that they converge to zero asymptotically, i.e. $\lim_{t\to\infty} \mathbf{g}^*(t) = 0$. A suitable choice for the dynamics of $\mathbf{g}^*(t)$ is given as

$$\sum_{j=k-1}^{0} \mathbf{T}_j \mathbf{g}^{*(j)} = \boldsymbol{\eta}^{*(k)} + \sum_{i=k-1}^{0} \rho_i \boldsymbol{I} \boldsymbol{\eta}^{*(i)} \tag{6.40}$$

where $\rho_0, \rho_1, \ldots, \rho_{k-1}$ are the coefficients of the characteristic polynomial describing the k^{th}-order exosystem generating the output reference profile (6.27), $\boldsymbol{I} = \mathbf{I}_{m\times m}$ is the identity matrix, and the constant matrices $\mathbf{T}_{k-1}, \ldots, \mathbf{T}_0 \in \mathbb{R}^{m\times m}$ are to be chosen. With the proper choice of these constant matrices

- a bounded state reference profile $\boldsymbol{\eta}^*(t)$ which asymptotically reaches the $\boldsymbol{\eta}_c(t)$ can be generated, and
- $\lim_{t\to\infty} \mathbf{g}^*(t) = 0$ holds.

According to SSC the internal state reference profile $\boldsymbol{\eta}^*(t)$ which asymptotically converges to $\boldsymbol{\eta}_c(t)$ is given by the following matrix differential equation

$$\boldsymbol{\eta}^{*(k)} + c_{k-1}\boldsymbol{\eta}^{*(k-1)} + \ldots + c_1\dot{\boldsymbol{\eta}}^* + c_0\boldsymbol{\eta}^* = -\left(\mathbf{M}_{k-1}\boldsymbol{\theta}_c^{(k-1)} + \ldots + \mathbf{M}_1\dot{\boldsymbol{\theta}}_c + \mathbf{M}_0\boldsymbol{\theta}_c\right) \tag{6.41}$$

where the numbers $c_0, c_1, \ldots, c_{k-1}$ are chosen to provide eigenvalue placement for the convergence $\boldsymbol{\eta}^* \to \boldsymbol{\eta}_c$ and the matrices $\mathbf{M}_{k-1}, \ldots, \mathbf{M}_0$ are given as

$$\begin{aligned}
\mathbf{M}_{k-1} &= \left(\mathbf{I} + c_{k-1}\mathbf{Q}^{-1} + \ldots + c_0\mathbf{Q}^{-k}\right)\left(\mathbf{I} + \rho_{k-1}\mathbf{Q}^{-1} + \ldots + \rho_0\mathbf{Q}^{-k}\right)^{-1} - \mathbf{I} \\
\mathbf{M}_{k-2} &= c_{k-2}\mathbf{Q}^{-1} + \ldots + c_0\mathbf{Q}^{-k+1} - (\mathbf{M}_{k-1} + \mathbf{I})\left(\rho_{k-2}\mathbf{Q}^{-1} + \ldots + \rho_0\mathbf{Q}^{-k+1}\right) \\
&\vdots \qquad\qquad \vdots \qquad\qquad \vdots \\
\mathbf{M}_1 &= c_1\mathbf{Q}^{-1} + c_0\mathbf{Q}^{-2} - (\mathbf{M}_{k-1} + \mathbf{I})\left(\rho_1\mathbf{Q}^{-1} + \rho_0\mathbf{Q}^{-2}\right) \\
\mathbf{M}_0 &= c_0\mathbf{Q}^{-1} - (\mathbf{M}_{k-1} + \mathbf{I})\,\rho_0\mathbf{Q}^{-1}.
\end{aligned} \tag{6.42}$$

The derivation of the matrix transfer function in Equation (6.41) and the proofs for the convergence of $\boldsymbol{\eta}^*(t) \to \boldsymbol{\eta}_c(t)$ and $\mathbf{g}^*(t)$ are given in Appendix B.2.

The driving term in the internal dynamics equation $\boldsymbol{\theta}_c(t)$ can be obtained with the help of the relation (6.5) as

$$\boldsymbol{\theta}_c(t) = \mathbf{P}\boldsymbol{\xi}_c(t) = \mathbf{P}\begin{bmatrix} -y_c(t) & -\dot{y}_c(t) & -\ddot{y}_c(t) & \ldots & -y_c^{(n-m-1)}(t) \end{bmatrix}^T. \tag{6.43}$$

6.6. Sliding mode controller design

Once the state reference trajectories $\boldsymbol{\eta}_c(t)$ and $\boldsymbol{\xi}_c(t)$ are identified, the problem of providing state-tracking in the system (6.7) can be solved using sliding mode control as follows. Introduce the error coordinates $\mathbf{e}_{\boldsymbol{\eta}}(t) = \boldsymbol{\eta}(t) - \boldsymbol{\eta}_c(t)$ and $\mathbf{e}_{\boldsymbol{\xi}}(t) = \boldsymbol{\xi}(t) - \boldsymbol{\xi}_c(t)$. The system in error coordinates is given as

$$\dot{\mathbf{e}}_{\boldsymbol{\eta}} = \mathbf{Q}\mathbf{e}_{\boldsymbol{\eta}} + \mathbf{P}\mathbf{e}_{\boldsymbol{\xi}} \tag{6.44a}$$

$$\dot{\mathbf{e}}_{\boldsymbol{\xi}} = \mathbf{S}\mathbf{e}_{\boldsymbol{\eta}} + \mathbf{R}\mathbf{e}_{\boldsymbol{\xi}} + \mathbf{b}_2 u, \tag{6.44b}$$

Define the sliding surface $\boldsymbol{\sigma} \in \mathbb{R}^{n-m}$ as

$$\boldsymbol{\sigma} = \mathbf{e}_{\boldsymbol{\xi}} + \boldsymbol{\lambda}^T \mathbf{e}_{\boldsymbol{\eta}}, \qquad \boldsymbol{\lambda}^T \in \mathbb{R}^{(n-m)\times m}. \tag{6.45}$$

In sliding mode, i.e. when $\boldsymbol{\sigma} = \mathbf{0}$,

$$\mathbf{e}_{\boldsymbol{\xi}} = -\boldsymbol{\lambda}^T \mathbf{e}_{\boldsymbol{\eta}} \tag{6.46}$$

and the internal state dynamics is given as

$$\dot{\mathbf{e}}_{\boldsymbol{\eta}} = (\mathbf{Q} - \mathbf{P}\boldsymbol{\lambda}^T)\mathbf{e}_{\boldsymbol{\eta}}. \tag{6.47}$$

Asymptotic stability of the internal state dynamics (6.47) can be ensured by choosing the eigenvalues of the matrix $(\mathbf{Q} - \mathbf{P}\boldsymbol{\lambda}^T)$ to be in the left half-plane. The ability of arbitrary eigenvalue placement for $(\mathbf{Q} - \mathbf{P}\boldsymbol{\lambda}^T)$ depends on the controllability [Kal59] of the pair $(\mathbf{Q}, \mathbf{P})$. Controllability of the pair $(\mathbf{Q}, \mathbf{P})$ is given when the pair $(\mathbf{A}, \mathbf{b})$ is controllable (see Section B.1 for the proof of this statement). Thus the internal state dynamics can be asymptotically stabilized in sliding mode by appropriate choice of $\boldsymbol{\lambda}$.

Depending on the relative degree of the system under consideration an output redefinition is required for designing the SMC law. The following conditions on relative degree are given

- Relative degree $\gamma = 1$: a standard first order sliding mode control law is suitable to enforce sliding mode
- Relative degree $\gamma > 1$:
  - first an output redefinition (see [GK93]) such that $\gamma = 1$ is performed and later a standard SMC law is used

- higher order sliding mode control laws can as well be used here.

In the case of output tracking for a DIO suffering from output delay, the relative degree of the system is equal to one, and thus a standard SMC law is designed in Chapter 7.

7. Stable System Center Approach based Output Tracking for a DIO

7.1. Introduction

The stable system center technique introduced in the previous chapter is used for output tracking of a DIO system suffering from output delay. First, the state space representation of the DIO system is considered along with the dead time and then, it is extended to a NMP system by approximating the output delay using the Padè approximation (Section 7.2). Results of simulation study are presented in Section 7.3 followed by the results from an experimental implementation on the Quanser rotary flexible joint in Section 7.4.

7.2. Representation of DIO with output delay as NMP system

The state space representation of the DIO system as given in (2.7) is

$$\frac{d}{dt}\begin{bmatrix}\dot{\varphi}_M\\ \Delta\varphi\\ \dot{\varphi}_L\end{bmatrix} = \begin{bmatrix}-\frac{d}{J_M} & -\frac{k}{J_M} & \frac{d}{J_M}\\ 1 & 0 & -1\\ \frac{d}{J_L} & \frac{k}{J_L} & -\frac{d}{J_L}\end{bmatrix}\begin{bmatrix}\dot{\varphi}_M\\ \Delta\varphi\\ \dot{\varphi}_L\end{bmatrix} + \begin{bmatrix}\frac{1}{J_M}\\ 0\\ 0\end{bmatrix} T_e \tag{7.1}$$

$$y = \begin{bmatrix}1 & 0 & 0\end{bmatrix}\begin{bmatrix}\dot{\varphi}_M\\ \Delta\varphi\\ \dot{\varphi}_L\end{bmatrix}. \tag{7.2}$$

The measured output y_m is available with a dead time of τ seconds, i.e.

$$Y_m(s) = Y(s)e^{-s\tau}, \tag{7.3}$$

where $Y_m(s)$ and $Y(s)$ are *Laplace* transforms of $y_m(t)$ and $y(t)$ respectively. Following the procedure described in Section 6.3, an additional state variable $\zeta = \check{y}_m + y$ is introduced to include the rational approximation of the dead time into the state space realization given by (7.1). Dynamics of the additional state variable $\zeta(t)$ are given by

$$\dot{\zeta} = \frac{2}{\tau}\zeta - \frac{4}{\tau}\check{y}_m. \tag{7.4}$$

Now, the state space model is extended by including the dynamics of $\check{y}_m$ as follows

$$\dot{\check{y}}_m = \dot{\zeta} - \dot{y}, \tag{7.5}$$

using (7.2) and (7.4)

$$\begin{aligned}
\dot{\check{y}}_m &= \frac{2}{\tau}\zeta - \frac{4}{\tau}\check{y}_m - \left(-\frac{d}{J_M}y - \frac{k}{J_M}\Delta\varphi + \frac{d}{J_M}\dot{\varphi}_L + \frac{1}{J_M}T_e\right) \\
&= \frac{2}{\tau}\zeta - \frac{4}{\tau}\check{y}_m + \frac{d}{J_M}\left(\zeta - \check{y}_m\right) + \frac{k}{J_M}\Delta\varphi - \frac{d}{J_M}\dot{\varphi}_L - \frac{1}{J_M}T_e \\
\dot{\check{y}}_m &= \left(\frac{2}{\tau} + \frac{d}{J_M}\right)\zeta + \left(-\frac{4}{\tau} - \frac{d}{J_M}\right)\check{y}_m + \frac{k}{J_M}\Delta\varphi - \frac{d}{J_M}\dot{\varphi}_L - \frac{1}{J_M}T_e.
\end{aligned} \tag{7.6}$$

Thus the extended state space realization representing the non-minimum phase approximation of the DIO with output delay is given as

$$\begin{bmatrix} \dot{\check{y}}_m \\ \dot{\zeta} \\ \Delta\dot{\varphi} \\ \ddot{\varphi}_L \end{bmatrix} = \begin{bmatrix} a_{11} & a_{12} & \frac{k}{J_M} & \frac{-d}{J_M} \\ \frac{-4}{\tau} & \frac{2}{\tau} & 0 & 0 \\ -1 & 1 & 0 & -1 \\ -\frac{d}{J_L} & \frac{d}{J_L} & \frac{k}{J_L} & -\frac{d}{J_L} \end{bmatrix} \cdot \begin{bmatrix} \check{y}_m \\ \zeta \\ \Delta\varphi \\ \dot{\varphi}_L \end{bmatrix} + \begin{bmatrix} -\frac{1}{J_M} \\ 0 \\ 0 \\ 0 \end{bmatrix} \cdot T_e, \tag{7.7}$$

$$\dot{\mathbf{x}}_e \quad = \quad \mathbf{A}_e \quad \cdot \quad \mathbf{x}_e \quad + \quad \mathbf{b}_e \quad \cdot u$$

where $a_{11} = -\frac{4}{\tau} - \frac{d}{J_M}$ and $a_{12} = \frac{2}{\tau} + \frac{d}{J_M}$.
This approximation is pictorially represented in Figure 7.1. The transfer function

describing the DIO system with the Padé approximation of the time delay is given as

$$G_{dio,td} = \frac{1}{(J_M + J_L)s} \frac{J_L s^2 + ds + k}{\left(\frac{J_M J_L}{J_M + J_L}\right) s^2 + ds + k} \left(\frac{1 - \frac{s\tau}{2}}{1 + \frac{s\tau}{2}}\right). \tag{7.8}$$

It has a relative degree[1] of 1, i.e. if the input-output dynamics are defined by the state $\xi(t)$ then, $\xi \in \mathbb{R}$ and if internal dynamics are described by the state $\boldsymbol{\eta}(t)$, then $\boldsymbol{\eta} \in \mathbb{R}^3$. In this case,

$$\xi := \check{y}_m, \text{ and} \tag{7.9}$$

$$\boldsymbol{\eta} := \begin{bmatrix} \zeta \\ \Delta\varphi \\ \dot{\varphi}_L \end{bmatrix}. \tag{7.10}$$

Thus the zero dynamics for the system given in Equation (7.7) can be written as

$$\dot{\boldsymbol{\eta}}(t) = \begin{bmatrix} \dot{\zeta} \\ \Delta\dot{\varphi} \\ \ddot{\varphi}_L \end{bmatrix} = \underbrace{\begin{bmatrix} \frac{2}{\tau} & 0 & 0 \\ 1 & 0 & -1 \\ \frac{d}{J_L} & \frac{k}{J_L} & \frac{-d}{J_L} \end{bmatrix}}_{:=\mathbf{Q}} \begin{bmatrix} \zeta \\ \Delta\varphi \\ \dot{\varphi}_L \end{bmatrix}. \tag{7.11}$$

Inspecting the spectrum of $\mathbf{Q}$

$$\lambda(\mathbf{Q}) = \left\{ \frac{2}{\tau}, \frac{-\left(d - \sqrt{d^2 - 4J_L k}\right)}{2J_L}, \frac{-\left(d + \sqrt{d^2 - 4J_L k}\right)}{2J_L} \right\}, \tag{7.12}$$

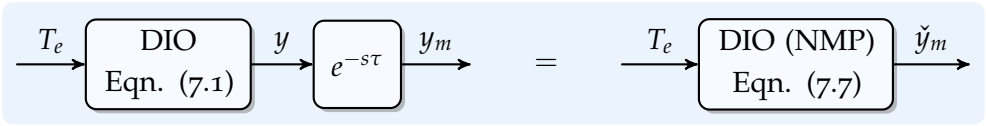

Figure 7.1.: Approximating the DIO with output time delay as a non-minimum phase system

[1] Refer C.4.

and considering the fact that J_L, k, d and τ are all positive, there is always one positive eigenvalue at $\frac{2}{\tau}$ rendering the zero dynamics unstable.

The vector $\mathbf{P} \in \mathbb{R}^{3\times 1}$, $R \in \mathbb{R}, b_2 \in \mathbb{R}$ and the vector $\mathbf{S} \in \mathbb{R}^{1\times 3}$ for the considered DIO system are given as

$$\mathbf{P} = \begin{bmatrix} -\frac{4}{\tau} \\ -1 \\ -\frac{d}{J_L} \end{bmatrix}, \quad R = -\frac{4}{\tau} - \frac{d}{J_M}, \quad b_2 = -\frac{1}{J_M} \text{ and } \mathbf{S} = \begin{bmatrix} \frac{2}{\tau} + \frac{d}{J_M} & \frac{k}{J_M} & \frac{-d}{J_M} \end{bmatrix}. \tag{7.13}$$

Thus using Equations (7.9) and (7.13) the DIO system with output delay in the Byrnes-Isidori normal form[2] is given as

$$\dot{\boldsymbol{\eta}}(t) = \mathbf{P}\check{y}_m(t) + \mathbf{Q}\boldsymbol{\eta}(t) \tag{7.14a}$$

$$\dot{\check{y}}_m(t) = R\check{y}_m(t) + \mathbf{S}\boldsymbol{\eta}(t) + b_2 u. \tag{7.14b}$$

7.3. Simulation of output tracking for a DIO system represented as an NMP system

Using the NMP representation of a DIO with output delay as given in the previous section, a SSC based reference trajectory generator as well as a standard first order SMC based state-tracking controller will be simulated in this section.

7.3.1. SSC based reference profile generation

For the generation of a bounded reference profile from the unstable internal dynamics (7.14a) using the method of SSC, first the following third-order characteristic polynomial is assumed for the exosystem generating the output reference profile

$$\Delta_3(s) = s\left(s^2 + \omega_n^2\right), \tag{7.15}$$

[2] simultaneously in the regular form for SMC law design

where ω_n is the frequency of the sinusoidal reference signal $y_c(t)$.
Now, the system center is written as

$$\begin{aligned}\dot{\boldsymbol{\eta}}_c(t) &= \mathbf{P}\xi_c(t) + \mathbf{Q}\boldsymbol{\eta}_c(t)\\ y_c(t) &= \xi_c(t) + \mathbf{0}\boldsymbol{\eta}_c(t).\end{aligned} \tag{7.16a}$$

According to the SSC method the bounded reference profile $\boldsymbol{\eta}^*(t)$ which asymptotically approached $\boldsymbol{\eta}_c(t)$ is given by the relation[3]

$$\bar{\boldsymbol{\eta}}^*(s) = -\frac{\left(\mathbf{M}_{k-1}s^{k-1} + \ldots + \mathbf{M}_1 s + \mathbf{M}_0\right)}{\left(s^k + c_{k-1}s^{k-1} + \ldots + c_1 s + c_0\right)}\mathbf{P}\boldsymbol{\Xi}_c(s) \tag{7.17}$$

where the numbers $c_0, c_1, \ldots, c_{k-1}$ are chosen to provide eigenvalue placement for the convergence of the bounded internal state reference profile and the matrices $\mathbf{M}_{k-1}, \ldots, \mathbf{M}_0$ are as given in (6.42) and $\boldsymbol{\Xi}_c(s)$ is the *Laplace* transform of $\boldsymbol{\xi}(t)$. The order of the exosystem generating the output reference profile is $k = 3$, and using (7.15) the coefficients of the characteristic polynomial defining the exosystem are given as $\rho_2 = 0, \rho_1 = \omega_n^2, \rho_0 = 0$. Using these values, the matrices from (6.42) are reduced as follows

$$\left.\begin{aligned}\mathbf{M}_2 &= \left(\mathbf{I} + c_2\mathbf{Q}^{-1}c_1\mathbf{Q}^{-2} + c_0\mathbf{Q}^{-3}\right)\left(\mathbf{I} + \omega_n^2\mathbf{Q}^{-2}\right)^{-1} - \mathbf{I}\\ \mathbf{M}_1 &= c_1\mathbf{Q}^{-1} + c_0\mathbf{Q}^{-2} - \omega_n^2\left(\mathbf{M}_2 + \mathbf{I}\right)\mathbf{Q}^{-1}\\ \mathbf{M}_0 &= c_0\mathbf{Q}^{-1}\end{aligned}\right\}. \tag{7.18}$$

And the transfer matrix generating the bounded internal reference profile is given by the following matrix transfer function

$$\bar{\boldsymbol{\eta}}^*(s) = -\frac{\left(\mathbf{M}_2 s^2 + \mathbf{M}_1 s + \mathbf{M}_0\right)}{\left(s^3 + c_2 s^2 + c_1 s + c_0\right)}\mathbf{P}\boldsymbol{\Xi}_c(s). \tag{7.19}$$

7.3.2. Sliding mode control law for state tracking

The original problem of output tracking is solved indirectly by stabilizing the system in error coordinates which are defined as

$$e_{\xi}(t) = e_y(t) = y_c(t) - \check{y}_m(t), \tag{7.20a}$$

$$\mathbf{e}_{\boldsymbol{\eta}}(t) = \boldsymbol{\eta}_c(t) - \boldsymbol{\eta}(t). \tag{7.20b}$$

[3]Once again the usual representation for the *Laplace*-transform holds as in page 100

Thus, the system in error coordinates is given as

$$\dot{\mathbf{e}}_{\eta} = \mathbf{Q}\mathbf{e}_{\eta} + \mathbf{P}e_y \tag{7.21a}$$

$$\dot{e}_y = \mathbf{S}\mathbf{e}_{\eta} + Re_y + b_2 u. \tag{7.21b}$$

For the use of a SMC law, the following sliding surface is defined

$$\sigma := e_y + \boldsymbol{\lambda}^T \mathbf{e}_{\eta}, \tag{7.22}$$

where $\boldsymbol{\lambda} \in \mathbb{R}^{3\times 1}$ is a design vector. Assuming that the sliding occurs, i.e. in sliding mode $\sigma(t) \equiv 0$,

$$e_y = -\boldsymbol{\lambda}^T \mathbf{e}_{\eta}, \tag{7.23}$$

implying that the system is described by the following reduced order dynamics

$$\begin{aligned} \dot{\mathbf{e}}_{\eta} &= \mathbf{Q}\mathbf{e}_{\eta} - \mathbf{P}\boldsymbol{\lambda}^T \mathbf{e}_{\eta}, \\ \dot{\mathbf{e}}_{\eta} &= \left(\mathbf{Q} - \mathbf{P}\boldsymbol{\lambda}^T\right) \mathbf{e}_{\eta}. \end{aligned} \tag{7.24}$$

Thus the choice of vector $\boldsymbol{\lambda}^T$ influences the dynamics of $\mathbf{e}_{\eta}(t)$ in sliding mode, and it is chosen such that the matrix $\left(\mathbf{Q} - \mathbf{P}\boldsymbol{\lambda}^T\right)$ has negative eigenvalues. The ability of placing arbitrary eigenvalues of this matrix is guaranteed by the controllability property of the pair $(\mathbf{Q}, \mathbf{P})$, which in turn depends on the controllability[4] of the pair $(\mathbf{A}_e, \mathbf{b}_e)$ from Equation (7.7). The controllability of the pair $(\mathbf{A}_e, \mathbf{b}_e)$ can be easily verified by the *Hautus* rank test [Hau70], the matrix $\mathbf{H}_u \in \mathbb{R}^{4\times 5}$ given as

$$\begin{aligned} \mathbf{H}_u &= \begin{bmatrix} s\mathbf{I} - \mathbf{A}_e & \mathbf{b}_e \end{bmatrix} \\ \mathbf{H}_u &= \begin{bmatrix} s + \dfrac{d}{J_M} + \dfrac{4}{\tau} & -\dfrac{d}{J_M} - \dfrac{2}{\tau} & -\dfrac{k}{J_M} & \dfrac{d}{J_M} & -\dfrac{1}{J_M} \\ \dfrac{4}{\tau} & s - \dfrac{2}{\tau} & 0 & 0 & 0 \\ 1 & -1 & s & 1 & 0 \\ \dfrac{d}{J_L} & -\dfrac{d}{J_L} & -\dfrac{k}{J_L} & s + \dfrac{d}{J_L} & 0 \end{bmatrix} \end{aligned} \tag{7.25}$$

has for all the eigenvalues of the matrix $\mathbf{A}_e$ the rank 4. It can be seen directly from (7.25) the last three columns are linearly independent and depending on the value of the complex variable s, the first two columns would at least give one column that is linearly

[4]Refer Appendix B.1

independent with the last three columns. Thus the pair $(\mathbf{A}_e, \mathbf{b}_e)$ is controllable and so is the pair $(\mathbf{Q}, \mathbf{P})$.

It is assumed when writing Equation (7.23) that the sliding mode is enforced on the system. In order to enforce sliding mode, one choice for the input $u(t)$ is given by the following condition on the derivative of the sliding surface

$$\frac{d\sigma}{dt} \stackrel{!}{=} -\kappa \operatorname{sgn}(\sigma), \qquad \kappa \in \mathbb{R}_+. \tag{7.26}$$

Using Equation (7.22),

$$\dot{e}_y + \boldsymbol{\lambda}^T \dot{\mathbf{e}}_{\boldsymbol{\eta}} = -\kappa \operatorname{sgn}(\sigma). \tag{7.27}$$

The left hand side of Equation (7.27) is expanded using Equation (7.20)

$$\dot{e}_y + \boldsymbol{\lambda}^T \dot{\mathbf{e}}_{\boldsymbol{\eta}} = \frac{d}{dt}\left(y_c - \check{y}_m\right) + \boldsymbol{\lambda}^T \frac{d}{dt}\left(\boldsymbol{\eta}_c - \boldsymbol{\eta}\right). \tag{7.28}$$

As both the reference profiles $y_c(t)$ and $\boldsymbol{\eta}_c(t)$ are known and are free of any high frequency noise, their time derivatives $\dot{y}_c(t)$ and $\dot{\boldsymbol{\eta}}_c(t)$ respectively can be numerically calculated. Thus using (7.14), Equation (7.28) is expanded as

$$\dot{e}_y + \boldsymbol{\lambda}^T \dot{\mathbf{e}}_{\boldsymbol{\eta}} = \dot{y}_c - \left(R\check{y}_m + \mathbf{S}\boldsymbol{\eta} + b_2 u\right) + \boldsymbol{\lambda}^T \left(\dot{\boldsymbol{\eta}}_c - \mathbf{P}\check{y}_m - \mathbf{Q}\boldsymbol{\eta}\right). \tag{7.29}$$

Considering that the vector

$$\boldsymbol{\lambda}^T = \begin{bmatrix} \lambda_1 & \lambda_2 & \lambda_3 \end{bmatrix}, \tag{7.30}$$

and substituting Equations (7.10), (7.13) into Equation (7.29) results in

$$\dot{e}_y + \boldsymbol{\lambda}^T \dot{\mathbf{e}}_{\boldsymbol{\eta}} = \dot{y}_c + \boldsymbol{\lambda}^T \dot{\boldsymbol{\eta}}_c + \nu_1 \check{y}_m + \nu_2 \zeta + \nu_3 \Delta\varphi + \nu_4 \dot{\varphi}_L + \frac{u}{J_M}, \tag{7.31}$$

where the constants ν_1, ν_2, ν_3 and $\nu_4 \in \mathbb{R}$ are given as follows

$$\left.\begin{aligned} \nu_1 &= \frac{4}{\tau}\left(1 + \lambda_1\right) + \lambda_2 + d\left(\frac{1}{J_M} + \frac{\lambda_3}{J_L}\right) \\ \nu_2 &= -\frac{2}{\tau}\left(1 + \lambda_1\right) - \lambda_2 - d\left(\frac{1}{J_M} + \frac{\lambda_3}{J_L}\right) \\ \nu_3 &= -k\left(\frac{1}{J_M} + \frac{\lambda_3}{J_L}\right) \\ \nu_4 &= d\left(\frac{1}{J_M} + \frac{\lambda_3}{J_L}\right) + \lambda_2 \end{aligned}\right\}. \tag{7.32}$$

Substituting back Equations (7.31) and (7.32) in (7.27) and solving for the control input results in

$$u = J_M \left(-\kappa \, \mathrm{sgn}(\sigma) - \dot{y}_c - \boldsymbol{\lambda}^T \dot{\boldsymbol{\eta}}_c - \nu_1 \check{y}_m - \nu_2 \zeta - \nu_3 \Delta\varphi - \nu_4 \dot{\varphi}_L \right). \tag{7.33}$$

For the sake of simulation it is assumed that all the state variables are available within the controller and that there is no uncertainty in the plant. Thus any value $\kappa > 0$ will drive the system trajectories in finite time to the sliding surface. On the sliding surface, i.e. during sliding mode the system behaves as a reduced order system given by the dynamics of $\mathbf{e}_\eta$ in (7.24).

7.3.3. Simulation of SMC based output tracking for DIO with output delay using SSC technique

The structure of the SIMULINK model used for the simulation is given in Figure 7.2. The exosystem generates the output reference profile to be tracked and the SSC generates the internal state reference profile. The NMP model is used to generate the states $\boldsymbol{\eta}$, $\check{y}_m$, and their corresponding errors are fed into the SMC law based tracking controller to generate the required control input u. For the sake of simulation the parameters of the RFJ given in Table 2.3 are used as the DIO model. The exosystem is parametrized such that the frequency of the sinusoidal output reference profile $\omega_n = 2\ rad/s$, the amplitude to be 4 rad/s and has an offset of 0.5 rad/s. For the implementation of SSC to generate a bounded internal state reference profile, i.e. for the implementation of transfer matrix given in Equation (7.19), the parameters c_0, c_1 and c_2 are chosen such that the denominator of (7.19) has three eigenvalues at -6.

For the sliding mode controller, first constants describing the sliding surface, $\boldsymbol{\lambda}^T$, are chosen such that eigenvalues of the matrix describing the reduced order dynamics in

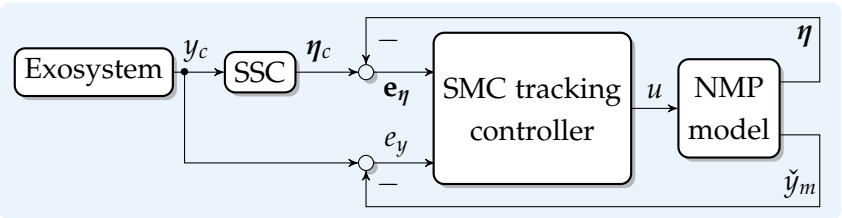

Figure 7.2.: Block diagram showing the SM output tracking controller using SSC.

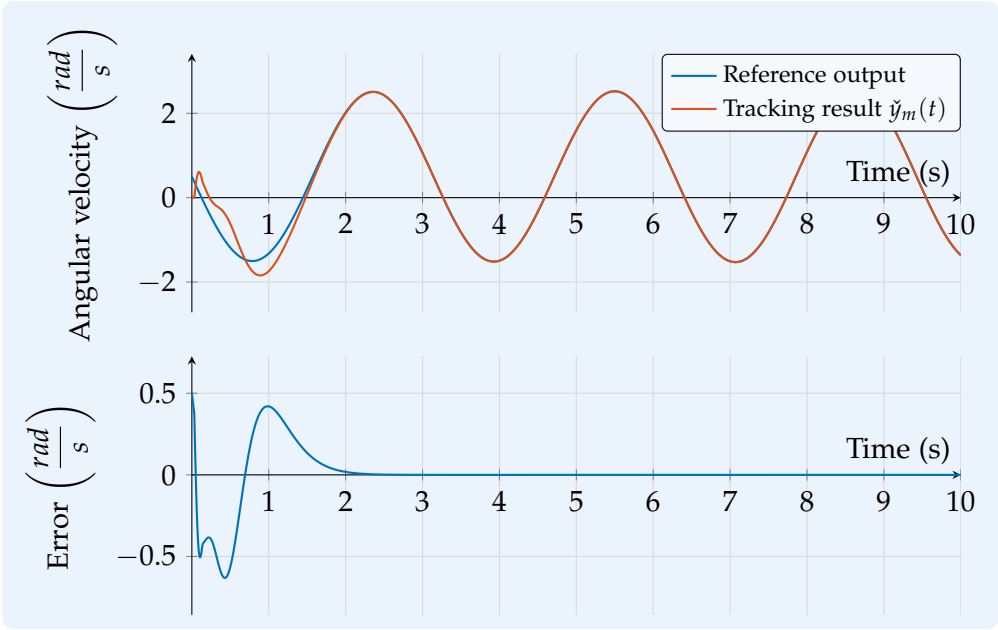

(a) Simulated trajectory tracking

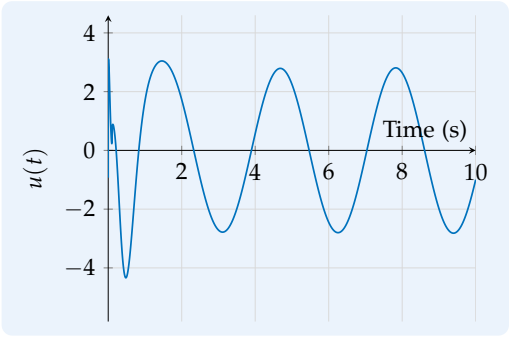

(b) Control input

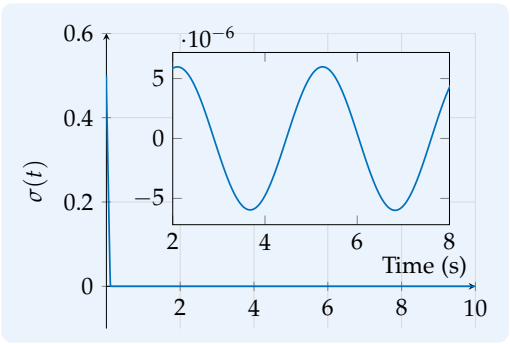

(c) Sliding variable

Figure 7.3.: Results of NMP output tracking using SSC and SMC law based feedback considering the whole internal state vector $\boldsymbol{\eta}$ in the feedback

sliding mode are at $-15-12, -10$. This choice of eigenvalues results in

$$\boldsymbol{\lambda}^T = \begin{bmatrix} -0.73 & -5.6 & 0.13 \end{bmatrix}. \tag{7.34}$$

Finally the gain of the discontinuous sign function for the sliding mode control law is chosen as $\kappa = 5$. In an effort to make the control input signal continuous/smooth, i.e. to eliminate chattering, the discontinuous function $\text{sgn}(.)$ is replaced by the following saturated linear relation within a thin boundary layer neighboring the sliding surface

$$sat_{\phi}(\sigma) = \begin{cases} \text{sgn}(\sigma), & |\sigma| \geq \phi \\ \dfrac{\sigma}{\phi}, & |\sigma| < \phi, \end{cases} \tag{7.35}$$

where ϕ gives the thickness of the boundary layer.

The plant, SSC and the SMC based state tracking controller are implemented in SIMULINK. This model is simulated using a fixed-step solver with a sample time of 1 ms. The simulated states are used for the control, i.e. all the states are assumed to be measurable[5]. Figure 7.3a plots the result of output tracking along with the tracking error, whereas Figures 7.3b and 7.3c plot the calculated control signal and the sliding variable dynamics. The sliding variable starts from an initial value away from zero and converges to zero in finite time and stays at zero, but due to the included linear approximation of the sign function with in a boundary layer, the sliding variable does not exactly slide along zero, but oscillates around $\sigma = 0$.

Instead of considering the whole internal state $\boldsymbol{\eta}(t)$ in the design of the sliding surface one could only consider the dynamics of $\zeta(t)$ (cf. Equation (7.7)), as the dynamics of $\begin{bmatrix} \Delta\varphi & \dot{\varphi}_L \end{bmatrix}$ are bounded input bounded state stable. Thus, the new sliding variable is defined as

$$\sigma = e_y + \lambda e_\zeta, \tag{7.36}$$

and by a suitable choice of the input $u(t)$, sliding mode is enforced. In sliding mode

$$e_y = -\lambda e_\zeta, \tag{7.37}$$

and the reduced order dynamics are given as

$$\dot{e}_\zeta = \left(\frac{2}{\tau} + \frac{4}{\tau}\lambda \right) e_\zeta. \tag{7.38}$$

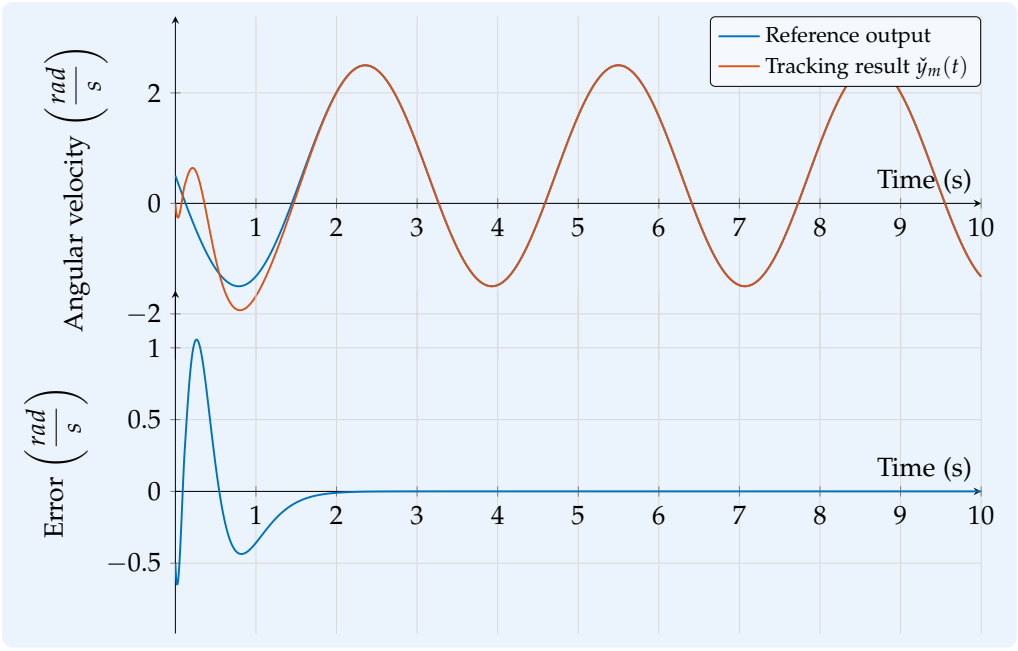

(a) Simulated output tracking using SSC and SMC

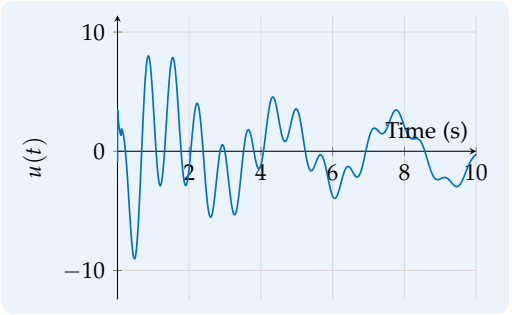

(b) Control input

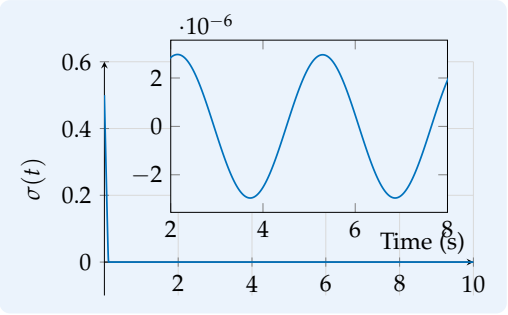

(c) Sliding variable

Figure 7.4.: Results of NMP output tracking using SSC and SMC law based feedback considering only a part of the internal state namely ζ in the feedback

Thus the error in the internal sate $e_\zeta(t)$ is driven to zero by an appropriate choice of variable λ

$$\lambda < -0.5, \tag{7.39}$$

which ensures that the output error is also driven to zero asymptotically (Equation 7.37). The appropriate choice of input signal to enforce sliding mode can be derived from Equations (7.33) and (7.32) by choosing $\lambda_2, \lambda_3 = 0$ and $\lambda_1 = \lambda \in \mathbb{R}$ and replacing $\dot{\boldsymbol{\eta}}_c$ by $\dot{\zeta}_c$ as

$$u = J_M \left(-\kappa \operatorname{sgn}(\sigma) - \dot{y}_c - \lambda \dot{\zeta}_c - \nu_1 \check{y}_m - \nu_2 \zeta + \frac{k}{J_M} \Delta\varphi - \frac{d}{J_M} \dot{\varphi}_L \right), \tag{7.40}$$

where $\nu_1 = \dfrac{4}{\tau}(1+\lambda) + \dfrac{d}{J_M}$ and $\nu_2 = -\dfrac{2}{\tau}(1+\lambda) - \dfrac{d}{J_M}$.

For the sake of simulation the variable $\lambda = -0.75$ is chosen. The results of simulation are plotted in Figures 7.4a and 7.4. It can be seen clearly from Figure 7.4a that the precision of output tracking is similar to the previous result, whereas the control signal shown in Figure 7.4b is more oscillatory when compared to the previous experiment. Also the precision of sliding variable dynamics in sliding mode in both the cases is similar. Note that the following assumptions are made for the simulations above

- all the states are available
- no model (plant) uncertainties
- the signal $\check{y}_m$ is used in the feedback.

Since the signals $\zeta(t)$ and $\check{y}_m(t)$ are only introduced in the extended model and are not part of the original DIO model, an observer is designed (as presented in the next section) for estimating these signals.

7.3.4. Sliding mode observer for unmeasurable states

Since only the output, angular velocity of the motor, $y(t)$ is available for measurement an observer is designed for estimating the rest of the states. A sliding mode observer is designed for this purpose [MRH13]. Consider the system given in the regular form (7.14) which is rewritten here as

$$\dot{\boldsymbol{\eta}}(t) = \mathbf{P}\check{y}_m(t) + \mathbf{Q}\boldsymbol{\eta}(t) \tag{7.41a}$$

$$\dot{\check{y}}_m(t) = R\check{y}_m(t) + \mathbf{S}\boldsymbol{\eta}(t) + b_2 u. \tag{7.41b}$$

[5] A SMC law based observer was developed for the actual experiments on the plant.

First the Observability of the system is verified using Hautus criterion[6] similar to Section 7.3.2. The observer proposed by [Utk81] has the form

$$\dot{\hat{\boldsymbol{\eta}}}(t) = \mathbf{P}\tilde{y}(t) + \mathbf{Q}\hat{\boldsymbol{\eta}}(t) + \mathbf{L}\nu \tag{7.42a}$$

$$\dot{\tilde{y}}(t) = R\tilde{y}(t) + \mathbf{S}\hat{\boldsymbol{\eta}}(t) + b_2 u - \nu, \tag{7.42b}$$

where $(\hat{\boldsymbol{\eta}}, \tilde{y})$ represent the state estimates for $(\boldsymbol{\eta}, \check{y}_m)$, $\mathbf{L} \in \mathbb{R}^{3\times 1}$ is a constant feedback gain vector and the discontinuous variable ν is defined by

$$\nu = M \operatorname{sgn}(\tilde{y} - \check{y}_m) \tag{7.43}$$

where $M \in \mathbb{R}_+$. If the errors between the estimates and the true states are written as $\mathbf{e}_1 = \hat{\boldsymbol{\eta}} - \boldsymbol{\eta}$ and $e_2 = \tilde{y} - \check{y}_m$, then using Equation (7.41) the following error dynamics is obtained

$$\dot{\mathbf{e}}_1(t) = \mathbf{P}e_2(t) + \mathbf{Q}\mathbf{e}_1(t) + \mathbf{L}\nu \tag{7.44a}$$

$$\dot{e}_2(t) = Re_2(t) + \mathbf{S}\mathbf{e}_1(t) - \nu. \tag{7.44b}$$

Since the pair $(\mathbf{A}_e, \mathbf{c}^T)$ is observable, the pair $(\mathbf{Q}, \mathbf{S})$ is also observable[7]. As a consequence the vector $\mathbf{L}$ can be chosen such that the eigenvalues of the matrix $(\mathbf{Q} + \mathbf{L}\mathbf{S})$ lie in $\mathbb{C}_-$. Consider a change of coordinates[8], dependent on $\mathbf{L}$, defined by the following transformation matrix

$$\mathbf{T} = \begin{bmatrix} \mathbf{I}_3 & \mathbf{L} \\ \mathbf{0} & 1 \end{bmatrix}. \tag{7.45}$$

Due to the special structure of the chosen transformation matrix $\mathbf{T}$, its inverse is given as

$$\mathbf{T}^{-1} = \begin{bmatrix} \mathbf{I}_3 & -\mathbf{L} \\ \mathbf{0} & 1 \end{bmatrix}. \tag{7.46}$$

Thus, the error dynamics in the new coordinates $\tilde{\mathbf{e}}_1 := \mathbf{e}_1 + \mathbf{L}e_y$ are given as

$$\dot{\tilde{\mathbf{e}}}_1(t) = \tilde{\mathbf{Q}}\tilde{\mathbf{e}}_1(t) + \tilde{\mathbf{P}}e_y(t) \tag{7.47a}$$

$$\dot{e}_y(t) = \mathbf{S}\tilde{\mathbf{e}}_1(t) + \tilde{R}e_y(t) - \nu, \tag{7.47b}$$

[6] rank of the rectangular matrix $\begin{bmatrix} c^T \\ s\mathbf{I} - \mathbf{A}_e \end{bmatrix} \stackrel{!}{=} 4$, where $c^T = \begin{bmatrix} 1 & 0 & 0 & 0 \end{bmatrix}$

[7] This result can be obtained as a dual result to the one obtained in Section B.1

[8] The aim of introducing the coordinate transformation is to simplify the analysis and design of the discontinuous term by restricting its effect to the last differential equation.

where $\tilde{\mathbf{Q}} = \mathbf{Q} + \mathbf{LS}, \tilde{\mathbf{P}} = \mathbf{P} + \mathbf{L}R - \tilde{\mathbf{Q}}\mathbf{L}$ and $\tilde{R} = R - \mathbf{SL}$. Now, by appropriate choice of M sliding mode can be enforced resulting in $e_y = 0$ in some finite time and the reduced plant dynamics in sliding mode are reduced to

$$\dot{\tilde{\mathbf{e}}}_1(t) = \tilde{\mathbf{Q}}\tilde{\mathbf{e}}_1(t). \tag{7.48}$$

By appropriate choice of vector $\mathbf{L}$, it follows that $\tilde{\mathbf{e}}_1 \to 0$ and consequently $\hat{\boldsymbol{\eta}} \to \boldsymbol{\eta}(t)$ as $t \to \infty$. The discontinuous term ν in the observer (7.47b) is responsible for robust stabilisation of the error system. Now, consider adding a negative output error feedback to these equations [ES98]

$$\dot{\tilde{\mathbf{e}}}_1(t) = \tilde{\mathbf{Q}}\tilde{\mathbf{e}}_1(t) + \tilde{\mathbf{P}}e_y(t) - \mathbf{G}_1 e_y \tag{7.49a}$$

$$\dot{e}_y(t) = \mathbf{S}\tilde{\mathbf{e}}_1(t) + \tilde{R}e_y(t) - G_2 e_y - \nu. \tag{7.49b}$$

By choosing $\mathbf{G}_1 = \tilde{\mathbf{P}}$ and $G_2 = \tilde{R} - G_2^s$, where $G_2^s < 0$, then

$$\dot{\tilde{\mathbf{e}}}_1(t) = \tilde{\mathbf{Q}}\tilde{\mathbf{e}}_1(t) \tag{7.50a}$$

$$\dot{e}_y(t) = \mathbf{S}\tilde{\mathbf{e}}_1(t) + G_2^s e_y - \nu. \tag{7.50b}$$

Since already, by choice of $\mathbf{L}$, the eigenvalues of the matrix $\tilde{\mathbf{Q}}$ lie in $\mathbb{C}_-$ and $G_2^s < 0$, the error system is asymptotically stable for $\nu \equiv 0$. The discontinuous term now is only responsible for robustness against bounded uncertainties.

7.3.5. Feedback of actual delayed output

The simulation results presented in the previous section use the signal $\check{y}_m(t)$ generated from the NMP system model in the feedback, but in the real world experiment it is required to feedback the actual measured signal $y_m(t)$. Figure 7.5 plots the output tracking result when $y_m(t)$ is fed back (used in the design of the sliding surface) instead of $\check{y}_m(t)$ keeping all the other simulation parameters same as in the previous section[9]. Clearly the tracking results are poor since the controller is actually designed for the output $\check{y}_m(t)$.

In order to improve the tracking performance a Smith predictor type feedback is used. Figure 7.6 shows the block diagram representing the SIMULINK model incorporating this type of feedback. A model of the actual plant $G_{DIO}(s)$ (cf. Equation (2.8)) with the

[9]The internal state measurements from the observer are used in the controller.

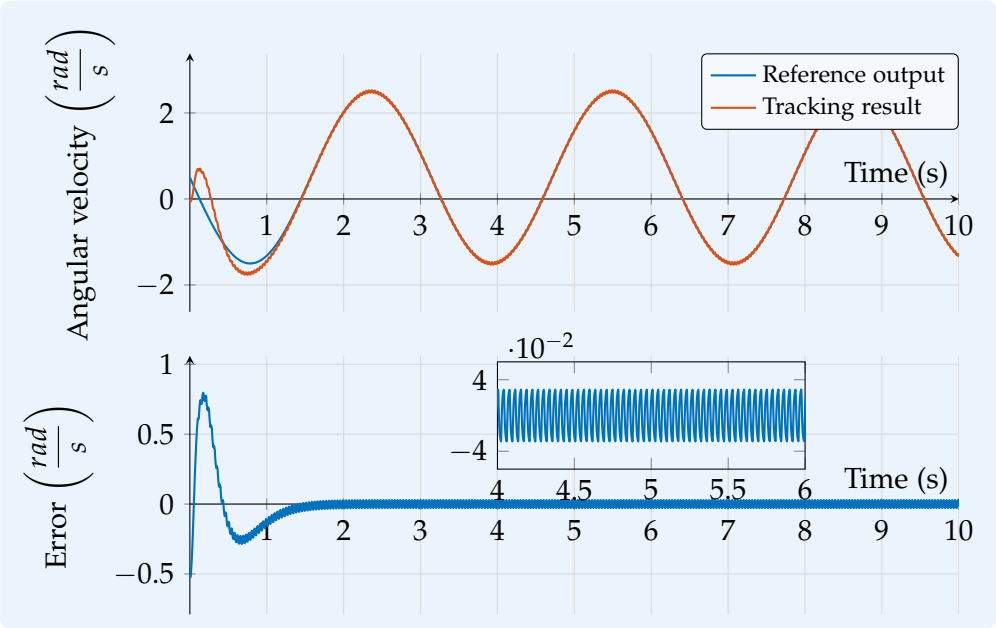

Figure 7.5.: Simulated output tracking by feeding back the delayed output

dead time $e^{-\tau s}$, represented respectively as $\hat{G}_{DIO}(s)$ and $e^{-\hat{\tau} s}$, along with the observer from the previous section are used in the feedback as shown in the block diagram. In case of a perfect model and dead time match, i.e. $\hat{G}_{DIO} = G_{DIO}$, $\hat{\tau} = \tau$ the feedback y_f only consists of the signal $\check{y}_m(t)$. The internal state $\zeta(t)$ estimated by the observer and the error in the internal state $e_\zeta(t)$ are represented in violet for the sake of clarity. The results of output tracking with this kind of feedback are similar to the results reported in Figure 7.4.

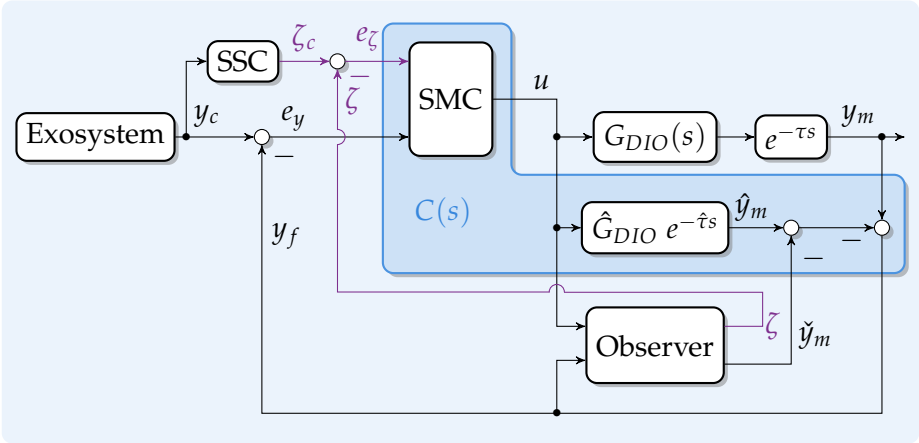

Figure 7.6.: Block diagram showing the Smith predictor type feedback used in NMP output tracking

7.4. Output tracking for rotary flexible joint: experimental results

The RFJ experimental setup from Quanser [Qua] as explained in Section 2.4 behaves as a DIO. The identified parameters including the output dead time are given in Table 2.3. The Simulink models developed in the previous section (cf. Figure 7.6) for the purpose of simulation can be used as well for programming the Quanser RFJ. This is made possible by the code generation functionality of Matlab/Simulink.

Before going into the details of implementation, the Simulink models are first updated to take into account that the actual plant input is voltage applied across the motor. The relation between the torque input to the NMP representation of the RFJ with output delay (6.37) and the actual voltage input to the plant is

$$T_e = K_M U_M, \tag{7.51}$$

where K_M is the motor torque constant as given in (2.23) and U_M is the voltage that is applied to the motor. For the purpose of output tracking, the reference output profile $y_c(t) = \xi_c(t)$ is assumed to be generated by the same exosystem as in Section 7.3.1 whose characteristic polynomial is given as

$$\Delta_3(s) = s\left(s^2 + \omega_n^2\right), \tag{7.52}$$

The reference profile generated by the exosystem is given as

$$y_c(t) = a + b\sin\omega_n(t) + e\cos\omega_n(t), \tag{7.53}$$

where ω_n is the frequency of the reference signal and a, b, e are real numbers. For the experiments the these parameters are chosen as follows

$$a = 0, \quad b = 0.2, \quad e = 0, \text{ and } \omega_n = 2\pi \; rad/s. \tag{7.54}$$

Only the error state $e_\zeta(t)$ is explicitly stabilised using the sliding mode controller. Thus the unstable system center is given as

$$\dot{\zeta}_c = -\frac{4}{\tau}\xi_c + \frac{2}{\tau}\zeta_c \tag{7.55a}$$

$$y_c = \xi_c. \tag{7.55b}$$

Comparing this system center with Equation (7.16)

$$P = -\frac{4}{\tau}, \qquad Q = \frac{2}{\tau}. \tag{7.56}$$

Since the internal state considered for tracking only consists of one variable $\zeta(t)$, the matrices $\mathbf{M}_0, \mathbf{M}_1, \mathbf{M}_2$ in (7.18) reduce to scalars and are given as (using Equation (7.56))

$$\left.\begin{aligned} M_2 &= \frac{4c_2\tau + 2\tau^2(c_1 - \omega_n^2) + c_0\tau^3}{8 + 2\tau^2\omega_n^2} \\ M_1 &= \frac{\tau^2(c_0 - c_2\omega_n^2) + 2\tau(c_1 - \omega_n^2)}{4 + \omega_n^2\tau^2} \\ M_0 &= c_0\frac{\tau}{2} \end{aligned}\right\}. \tag{7.57}$$

The transfer matrix in Equation (7.19) reduces to the following transfer function

$$\bar{\zeta}^*(s) = -\frac{\left(M_2 s^2 + M_1 s + M_0\right)}{s^3 + c_2 s^2 + c_1 s + c_0} P Y_c(s), \tag{7.58}$$

where $\zeta^*(t) \circ\!\!-\!\!\bullet\, \bar{\zeta}^*(s)$, $y_c(t) \circ\!\!-\!\!\bullet\, Y_c(s)$ and the convergence of $\zeta^*(t) \to \zeta_c(t)$ is guaranteed by the choice of parameters c_2, c_1 and c_0. These parameters are chosen such that the denominator of (7.58) has three eigenvalues at -6.

The sliding mode observer as presented in Section 7.3.4 is implemented first for estimating the signals $\check{y}_m(t)$ and $\zeta(t)$. The sliding mode controller as given in (7.40) is modified for the QUANSER RFJ as

$$U_M = u = \frac{J_M}{K_M}\left(-\kappa\,\mathrm{sgn}(\sigma) - \dot{y}_c - \lambda\dot{\zeta}_c - \nu_1\check{y}_m - \nu_2\zeta + \frac{k}{J_M}\Delta\varphi - \frac{d}{J_M}\dot{\varphi}_L\right), \tag{7.59}$$

with $\nu_1 = \frac{4}{\tau}(1+\lambda) + \frac{d}{J_M}$ and $\nu_2 = -\frac{2}{\tau}(1+\lambda) - \frac{d}{J_M}$.
The discontinuous terms in both the controller and observer are replaced by the saturated linear relation within a thin boundary layer neighbouring the sliding surface as was done in Section 7.3.3. The boundary layer widths are represented as ϕ_{ctrl} and ϕ_O respectively in the controller and the observer. The parameters for the experiment are chosen as given in Table 7.1. The sample time was chosen as 1 ms for the experiments through out this section. The output tracking result using these parameters is plotted in Figure 7.7. It is obvious from the error plot that the tracking error in the output is not driven to zero. This is because of the unmodelled friction that is acting both on the motor side and the load side. The friction on the load side is unmatched with respect to the control input U_M, so the SMC is not able to compensate this disturbance[10].

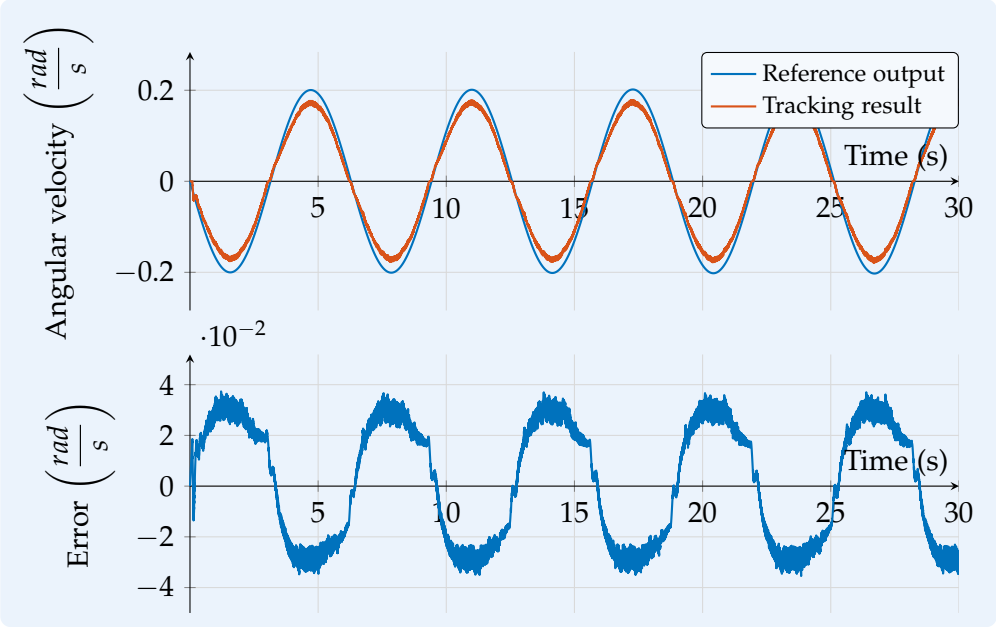

Figure 7.7.: Tracking result from Quanser RFJ experimental set up using SSC and SMC based state tracking controller.

In order to improve the performance of the tracking controller, the classical technique of adding an integrator by extending the system order is employed. Towards this end the new state variable ϵ is introduced as

$$\frac{d\epsilon}{dt} = y_c - y_f = e_y. \tag{7.60}$$

[10]See Appendix C for more details about matched and unmatched disturbances.

Table 7.1.: Controller parameters

SMC		Observer	
Parameter	Value	Parameter	Value
λ	-1.75	G_2^s	-5.5
κ	50	M	300
ϕ_{ctrl}	0.05	ϕ_O	0.01

Using this new state variable, the system in error coordinates given by (7.21) is extended as (considering only $\zeta(t)$ for internal state)

$$\begin{aligned}
\dot{e}_\zeta &= \frac{2}{\tau}e_\zeta - \frac{4}{\tau}e_y \\
\dot{e}_y &= \left(\frac{2}{\tau} + \frac{d}{J_M}\right)e_\zeta + \left(-\frac{4}{\tau} - \frac{d}{J_M}\right)e_y + \frac{k}{J_M}\Delta\varphi - \frac{d}{J_M}\dot{\varphi}_L - \frac{K_M}{J_M}U_M \\
\dot{\epsilon} &= e_y.
\end{aligned} \tag{7.61}$$

The sliding surface defined in (7.22) is also extended to include the new state vector as

$$\sigma(t) = e_y(t) + \lambda \mathrm{e}_\zeta(t) + \mu\epsilon(t) = e_y(t) + \lambda e_\zeta(t) + \mu\int_0^t e_y(\tilde{t})d\tilde{t}. \tag{7.62}$$

The control input U_M from (7.59) is extended as

$$U_M = u = \frac{J_M}{K_M}\left(-\kappa\,\mathrm{sgn}(\sigma) - \dot{y}_c - \lambda\dot{\zeta}_c - \nu_1\check{y}_m - \nu_2\zeta + \frac{k}{J_M}\Delta\varphi - \frac{d}{J_M}\dot{\varphi}_L - \mu e_y\right). \tag{7.63}$$

Using the sliding surface with the integral of the output error and the controller as given in (7.63) the improved tracking results obtained on the RFJ experimental set up are plotted in Figure 7.8. It is clear from the figure that the tracking error increases when the angular velocity crosses zero because of the static friction present in the system. This static friction is generated by the multiple slip rings present between the carrier and the base frames as shown in Figure 2.16 on page 29. Since the friction on the load side is unmatched with respect to the control input, U_M

The same experiment is conducted with a PI controller replacing the state tracking SMC law. The PI controller parameters are tuned such that the peak in the measured angular velocity is as close to 0.2 rad/s as possible and that the oscillations in the velocity response are minimum. The parameters used for the experimentation are $k_p = 12, k_i = 80$, where k_p and k_i are the proportional and integral gains respectively.

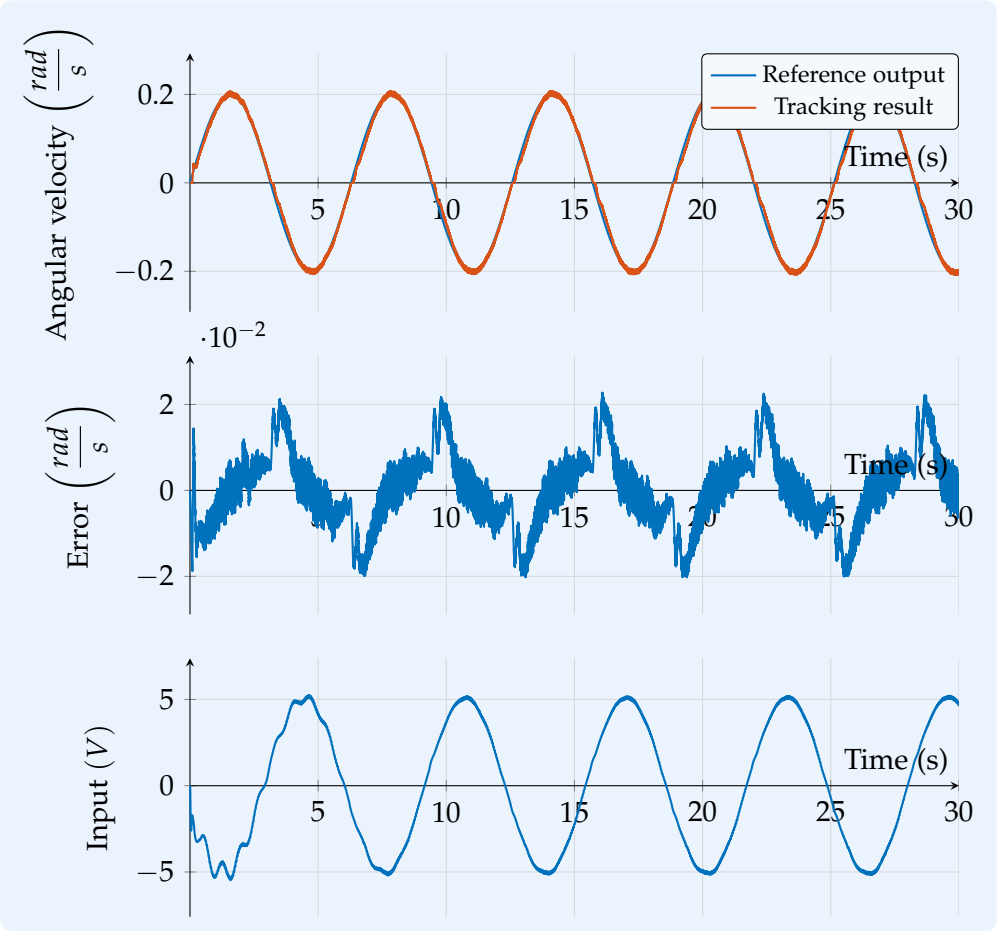

Figure 7.8.: Output tracking result from QUANSER RFJ experimental set up using SSC and SMC with integral action.

One can clearly see the improvement that the SSC based state tracking brings to the output tracking. The major reason behind this improvement is the fact that the PI controller has as its input the error in the output signal calculated using the delayed measured signal, whereas the SSC based SMC controller has the delay free output signal $\check{y}_m(t)$ within the feedback.

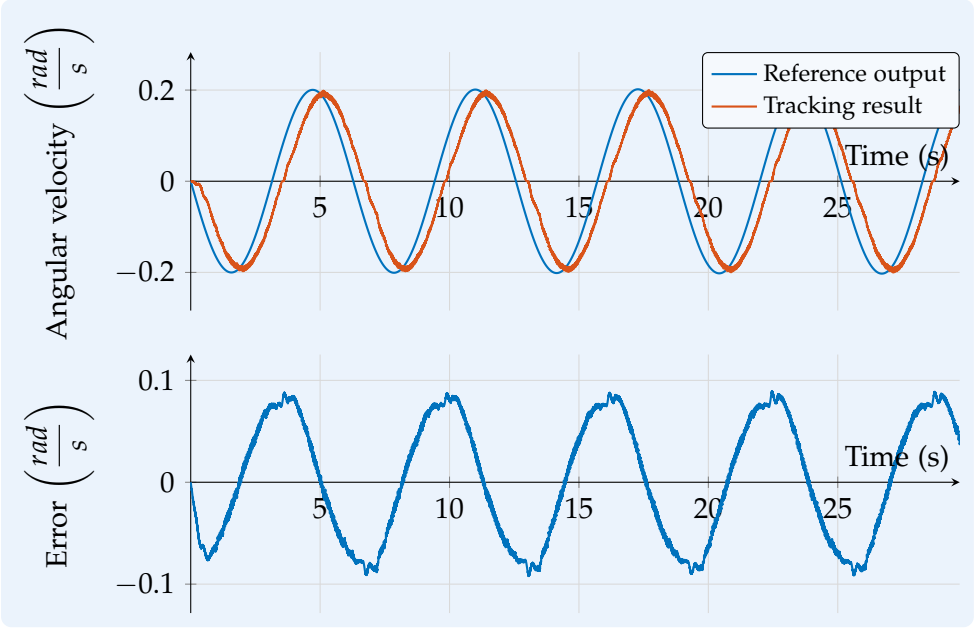

Figure 7.9.: Tracking result from RFj with PI controller.

8. Conclusion and Outlook

This thesis deals with a motion control system involving a dual-inertia system whose velocity loop bandwidth is limited by mechanical resonance. When the resonance mode is weakly damped, this loop results in torsional oscillations that degrades the loops response and might even damage the mechanical structure. Any control engineering technique that is designed to improve the response of such a velocity control loop should take into account the influence of the location of the resonance frequency in relation to the loop's phase crossover frequency. Following two categories are distinguished, low-resonance frequency and high-resonance frequency. A system is said to be suffering from low-resonance frequency if the resonance frequency is closer to the phase crossover frequency (typically between 100 to 300 Hz), and high-resonance frequency (typically between 400 Hz and above) if it is much higher than the phase crossover frequency. Most frequently encountered problem of high-resonance frequency can be overcome by using digital filters like the Notch or Bi-quad filters. But the low-frequency resonance, due to its close proximity to the phase crossover frequency demands more attention. The work in this thesis is concerned with the systems suffering from low-frequency resonance.

Using a mathematical model the two phenomena namely mechanical resonance and dead times, responsible for the loss of velocity control loop's gain margin in the considered system, are elucidated in Sections 2.1 and 2.2. The work reported in this thesis is divided into two parts, and the first part deals with the extended acceleration feedback technique which is designed to win back a part of the gain margin that is lost due to the mechanical resonance. AF technique effectively reduces drive's sensitivity to mechanical resonance by increasing its inertia. Interestingly the results presented in Chapter 3 using the AF technique did not bring in any noticeable improvement in the speed response. A systematic investigation based on frequency domain analysis and describing function analysis (Section 4.1) followed by careful design of additional filters resulted in the EAF technique presented in Section 4.2. The implementation details, the

achieved improvements both in frequency (in terms of increase in the gain margin) and time domain (in terms of the control error) are reported in Section 4.3.

The second part of the work dealt with mitigation of dead time in the control loop. The technique used herein is based on a non-minimum phase representation of the dead time using Padé approximation. Thus, the output tracking problem for a system with output delay is approximated as the non-minimum phase output tracking problem. The unstable internal dynamics introduced by the Padé approximation is calculated (asymptotically) using the so-called stable system center technique in Section 6.5. Using this signal, the output tracking problem is reformulated as a state-tracking problem and a sliding mode controller is designed (Section 6.6). The sliding mode controller drives both the output tracking errors and also the error from the stable system center approach to zero. This technique is implemented on a laboratory test setup and the details are presented in Chapter 7.

Following are a list of problems of interest for further work:

- applicability of the EAF method in case of three mass system;
- robustness of the SMC with stable system center technique in case of variable dead-time system as in the case of networked drives, i.e. where a controller drives more than one motor via a communication network;
- online identification of the characteristic polynomial describing the exo-system generating the output reference profile as reported in [Sht+12].
- The SMC used in the work cannot cope with the disturbance on the load side as it is unmatched with respect to the control signal. Techniques for compensating unmatched disturbances could be investigated for the current application [YLY13; Yan+14; LBF13]
- Investigation of the advantages and realization of a controller if an additional measurement velocity/position from the load side is available or is estimated [SO07; SO08].

Appendices

A. Relative Stability: Phase and Gain margins

Considering a unity-feedback system as shown in Figure 1.2. If the transfer functions of the controller and the plant are $C(s)$ and $G(s)$, respectively, then the stability of this feedback loop can be verified by asserting that the poles of its transfer function given as

$$T(s) = \frac{G(s)C(s)}{1 + G(s)C(s)} \tag{A.1}$$

have negative real part. One can also use Bode or Nyquist plot of the loop transfer function $L(s) := G(s)C(s)$ for determining the stability of $T(s)$. An added advantage with these frequency domain plots is the ability to determine a measure for the degree of stability of the closed-loop system which is useful when designing control systems.

A.1. Gain margin, Phase margin and stability

Consider the bode plot of an open-loop transfer function as shown in Figure A.1. The frequency at which the phase of $L(s)$ is equal to -180° is known as the *phase crossover frequency*, represented as ω_p. The frequency at which the gain of $L(s)$ crosses the $0\ dB$-line is known as the *gain crossover frequency*, represented as ω_g. The, *gain margin* is defined as the distance between the $0\ dB$-line and the gain at the phase crossover frequency. Similarly, the *phase margin* is defined as the distance measured in $^\circ$ between the -180°-line and the phase at the gain crossover frequency. These concepts are also similarly defined on the *Nyquist plot*, which plots the real part of the open-loop transfer function against its imaginary part with increasing frequencies.

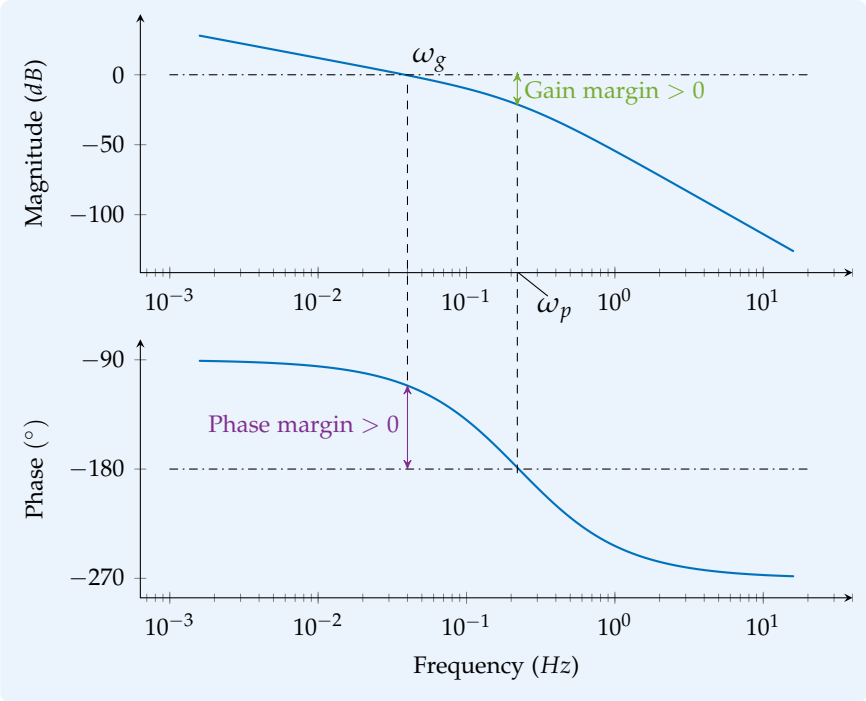

Figure A.1.: Phase margin and gain margin

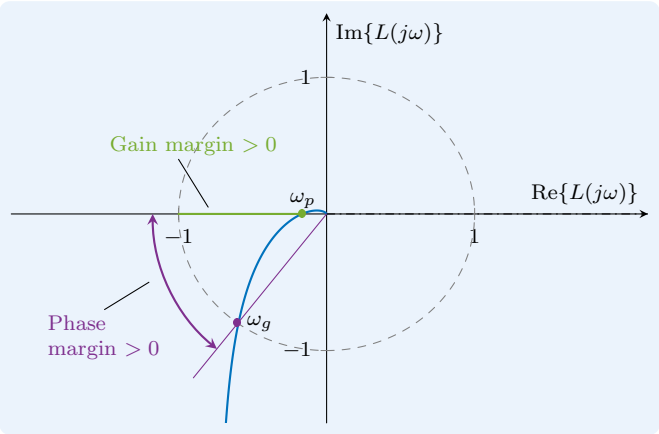

Figure A.2.: Phase margin and gain margin on Nyquist plot

The stability of $T(s)$ given in (A.1) can be inferred from the Bode plot, if both the gain and phase margins are positive for a given $L(s)$. However, this criterion is only valid when the open loop transfer function is stable and there are no multiple gain and/or phase crossovers. The stability analysis using Nyquist plot does not have this restriction and is also valid for unstable loop transfer functions. In the case of the Nyquist plot, the point $(-1, 0)$ is known as the *critical point*, while it represents the situation where the open loop gain is 1, i.e. 0 dB and the phase if $-180°$. The $T(s)$ in (A.1) is stable if and only if the Nyquist plot of $L(s)$ does not pass through the critical point and the number of counter-clockwise encirclements of the critical point equals the number of *open* right-half-plane poles of $L(s)$.

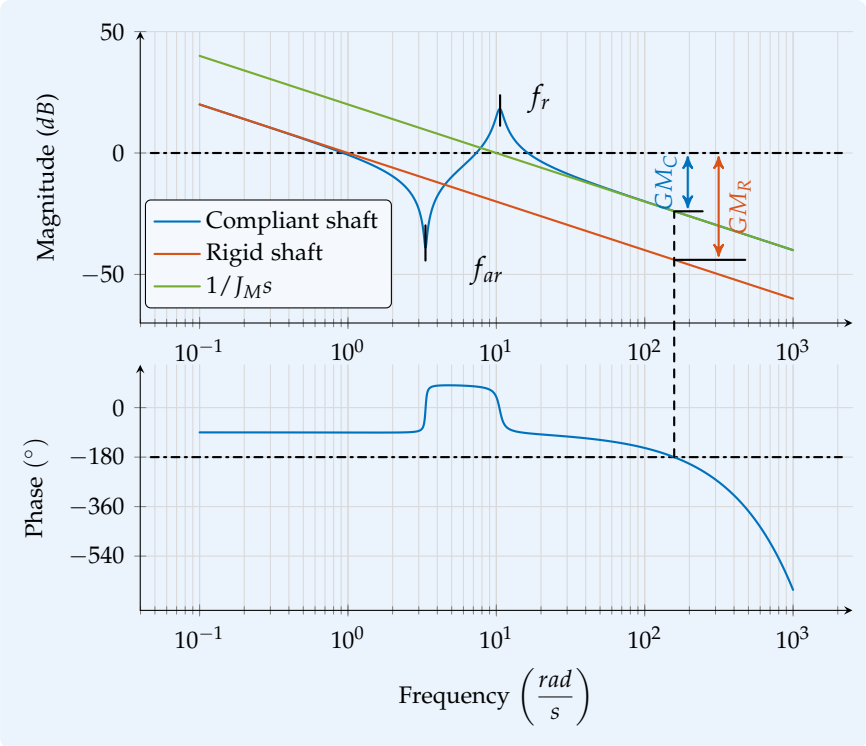

Figure A.3.: Plot depicting the erosion of gain margin due to the elastic shaft

A.2. Bode and Nyquist plots for unity-feedback loop with DIO

Consider the Bode plot of an open-loop transfer function (2.21) consisting of the DIO and a proportional speed controller as shown in Figure A.3. From the first glance it is clear that there are multiple gain crossovers at $\approx 1,\ 7$ and $10.8\frac{rad}{s}$ as well as multiple phase crossovers at $-180°, -540°, \ldots$,etc. It seems to be incorrect to consider in this case gain margin as a measure of relative stability.

Now, consider the Nyquist plot for this same DIO transfer function as plotted[1] in Figure A.4. The plot begins for smaller frequencies at $-\infty$, while the phase at low frequencies is $-90°$, and crosses the unit circle (corresponds to the $0\ dB$-line in Bode plot) three times and goes to the origin after infinite encirclements around it (due to the considered dead time). It can be seen from the inlet of Figure A.4, which zooms close to the origin, that the loop transfer function always remains to the right of the critical point. Thus it can be concluded from the Nyquist plot that the closed loop system will indeed be stable and that gain margin can be used as a measure of stability.

In fact according to [HEE01], a closed-loop system is stable if the open-loop system is stable and the Bode plot of the open-loop transfer function has a magnitude less than $0\ dB$ at all frequencies corresponding to a phase lag of $180° + n * 360°$, with $n = 0, 1, \ldots, \infty$. The gain margin in this case with multiple gain crossovers is calculated from the crossover frequency corresponding to a larger n, whichever exhibits the largest magnitude in dB. In the case of DIO, this calculation is shown on both the Bode plot A.3 and the Nyquist plot A.4.

[1] k_p is increased to 3 for the sake of illustration

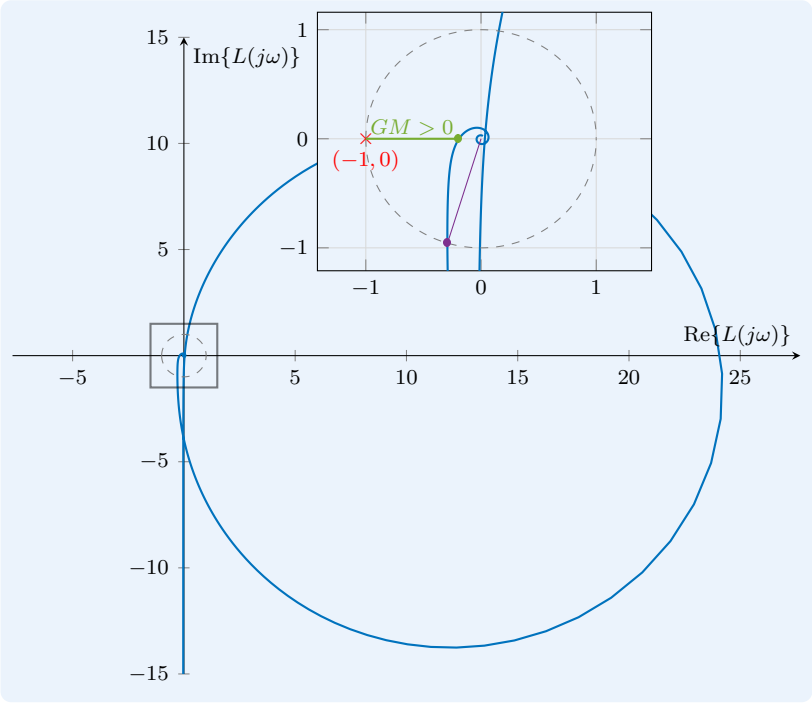

Figure A.4.: Phase margin and gain margin on Nyquist plot

B. Stable System Center Technique- Proofs

B.1. Controllability proof

A proof of the controllability assumption for the pair $(\mathbf{P}, \mathbf{Q})$ given the controllability of pair $(\mathbf{A}, \mathbf{b})$ is presented here. Remember that the Byrnes-Isidori normal form given in the regular form by Equations (6.28a) and (6.28b) is obtained from the fully controllable system (6.2) with the help of a linear nonsingular state transformation (6.3). So, if the pair $(\mathbf{A}, \mathbf{b})$ is controllable, then so is the pair $(\bar{\mathbf{A}}, \bar{\mathbf{b}})$ where

$$\bar{\mathbf{A}} = \begin{pmatrix} \mathbf{Q} & \mathbf{P} \\ \mathbf{S} & \mathbf{R} \end{pmatrix} \text{ and } \bar{\mathbf{b}} = \begin{pmatrix} \mathbf{0} \\ \mathbf{b}_2 \end{pmatrix}.$$

Then, using the Hautus rank test [Hau70]

$$\text{row rank } \begin{pmatrix} s\mathbf{I}_n - \bar{\mathbf{A}} & \bar{\mathbf{b}} \end{pmatrix} = n.$$

$$\Rightarrow \quad \text{row rank } \begin{pmatrix} s\mathbf{I}_m - \mathbf{Q} & -\mathbf{P} & \mathbf{0} \\ -\mathbf{S} & s\mathbf{I}_{n-m} - \mathbf{R} & \mathbf{b}_2 \end{pmatrix} = n \qquad \forall s$$

$$\Rightarrow \quad \text{row rank } \begin{pmatrix} s\mathbf{I}_m - \mathbf{Q} & -\mathbf{P} \end{pmatrix} = m \qquad \forall s$$

$$\Leftrightarrow \quad \text{row rank } \begin{pmatrix} s\mathbf{I}_m - \mathbf{Q} & \mathbf{P} \end{pmatrix} = m \qquad \forall s.$$

Therefore the pair $(\mathbf{Q}, \mathbf{P})$ is controllable.

B.2. SSC

The dynamic variable $\mathbf{g}^*$ is introduced as follows

$$\dot{\boldsymbol{\eta}}^* = \mathbf{Q}\boldsymbol{\eta}^* + \boldsymbol{\theta}_c + \mathbf{g}^*, \tag{B.1}$$

where $\boldsymbol{\theta}_c$ is given as

$$\boldsymbol{\theta}_c = \mathbf{P}\boldsymbol{\xi}_c$$

and the dynamics of $\mathbf{g}^*$ are given by the following differential equation

$$\boldsymbol{\eta}^{*(k)} + \rho_{k-1}\mathbf{I}_m\boldsymbol{\eta}^{*(k-1)} + \ldots + \rho_1\mathbf{I}_m\dot{\boldsymbol{\eta}}^* + \rho_0\mathbf{I}_m\boldsymbol{\eta}^* = \mathbf{T}_{k-1}\mathbf{g}^{*(k-1)} + \ldots + \mathbf{T}_1\dot{\mathbf{g}}^* + \mathbf{T}_0\mathbf{g}^*. \tag{B.2}$$

Here $\mathbf{I}_m \in \mathbb{R}^{m\times m}$ is the identity matrix, k the order of the exo-system as mentioned in Section 6.5.3 and the matrices $\mathbf{T}_0, \mathbf{T}_1, \ldots, \mathbf{T}_{k-1} \in \mathbb{R}^{m\times m}$ are to be chosen properly. Using (B.2), the following equation holds in *Laplacian* domain

$$\left(\mathbf{T}_{k-1}s^{k-1} + \ldots + \mathbf{T}_1 s + \mathbf{T}_0\right)\mathbf{G}^*(s) = \left(s^k\mathbf{I} + \rho_{k-1}s^{k-1}\mathbf{I} + \ldots + \rho_1 s\mathbf{I} + \rho_0\mathbf{I}\right)\bar{\boldsymbol{\eta}}^*(s), \tag{B.3}$$

where $\mathbf{G}^*(s)$ and $\bar{\boldsymbol{\eta}}^*(s)$ are the variables $\mathbf{g}^*$ and $\boldsymbol{\eta}^*$ in *Laplacian* domain. Similarly, (B.1) in *Laplacian* domain[1]

$$s\bar{\boldsymbol{\eta}}^* = \mathbf{Q}\bar{\boldsymbol{\eta}}^* + \bar{\boldsymbol{\Theta}}_c + \mathbf{G}^*. \tag{B.4}$$

Substituting (B.4) in (B.3) to eliminate $\mathbf{G}^*(s)$ results in the following matrix differential equation

$$\begin{aligned}\Big[&s^k\left(\mathbf{I} - \mathbf{T}_{k-1}\right) + s^{k-1}\left(\mathbf{T}_{k-1}\mathbf{Q} - \mathbf{T}_{k-2} + \rho_{k-1}\mathbf{I}\right) + \ldots + \\ &+ s\left(\rho_1\mathbf{I} + \mathbf{T}_1\mathbf{Q} - \mathbf{T}_0\right) + \left(\mathbf{T}_0\mathbf{Q} - \rho_0\mathbf{I}\right)\Big]\bar{\boldsymbol{\eta}}^* = -\left(\mathbf{T}_{k-1}s^{k-1} + \ldots + \mathbf{T}_1 s + \mathbf{T}_0\right)\bar{\boldsymbol{\Theta}}_c.\end{aligned} \tag{B.5}$$

Pre-multiplying (B.5) with $\left(\mathbf{I} - \mathbf{T}_{k-1}\right)^{-1}$ on both sides results in

$$\begin{aligned}\Big[&s^k + s^{k-1}\left(\mathbf{I} - \mathbf{T}_{k-1}\right)^{-1}\left(\rho_{k-1}\mathbf{I} + \mathbf{T}_{k-1}\mathbf{Q} - \mathbf{T}_{k-2}\right) + \ldots + \\ &+ s\left(\mathbf{I} - \mathbf{T}_{k-1}\right)^{-1}\left(\rho_1\mathbf{I} + \mathbf{T}_1\mathbf{Q} - \mathbf{T}_0\right) + \left(\mathbf{I} - \mathbf{T}_{k-1}\right)^{-1}\left(\mathbf{T}_0\mathbf{Q} + \rho_0\mathbf{I}\right)\Big]\bar{\boldsymbol{\eta}}^* \\ &= -\left[\left(\mathbf{I} - \mathbf{T}_{k-1}\right)^{-1}\mathbf{T}_{k-1}s^{k-1} + \ldots + \left(\mathbf{I} - \mathbf{T}_{k-1}\right)^{-1}\mathbf{T}_1 s + \left(\mathbf{I} - \mathbf{T}_{k-1}\right)^{-1}\mathbf{T}_0\right]\bar{\boldsymbol{\Theta}}_c.\end{aligned} \tag{B.6}$$

[1] $\boldsymbol{\theta}_c(t) \circ\!\!-\!\!\bullet\, \bar{\boldsymbol{\Theta}}_c(s)$

In order to provide desired eigenvalue placement for the asymptotic convergence $\boldsymbol{\eta}^* \to \boldsymbol{\eta}_c$ the coefficient matrices in (B.6) are chosen as

$$\begin{aligned} c_{k-1}\mathbf{I} &= (\mathbf{I} - \mathbf{T}_{k-1})^{-1} (\rho_{k-1}\mathbf{I} + \mathbf{T}_{k-1}\mathbf{Q} - \mathbf{T}_{k-2}) \\ &\vdots \\ c_1\mathbf{I} &= (\mathbf{I} - \mathbf{T}_{k-1})^{-1} (\rho_1\mathbf{I} + \mathbf{T}_1\mathbf{Q} - \mathbf{T}_0) \\ c_0\mathbf{I} &= (\mathbf{I} - \mathbf{T}_{k-1})^{-1} (\rho_0\mathbf{I} + \mathbf{T}_0\mathbf{Q}) \,. \end{aligned} \tag{B.7}$$

It remains to represent the matrices $\mathbf{T}_0, \mathbf{T}_1, \ldots, \mathbf{T}_{k-1}$ in terms of the chosen numbers $c_0, c_1, \ldots, c_{k-1}$ and $\rho_0, \rho_1, \ldots, \rho_{k-1}$ and the known matrix $\mathbf{Q}$. To this end, the following matrices are defined

$$\begin{aligned} \mathbf{M}_{k-1} &:= (\mathbf{I} - \mathbf{T}_{k-1})^{-1} \mathbf{T}_{k-1} \\ &\vdots \\ \mathbf{M}_1 &:= (\mathbf{I} - \mathbf{T}_{k-1})^{-1} \mathbf{T}_1 \\ \mathbf{M}_0 &:= (\mathbf{I} - \mathbf{T}_{k-1})^{-1} \mathbf{T}_0. \end{aligned} \tag{B.8}$$

Now, consider for example

$$\begin{aligned} c_0\mathbf{I} &= (\mathbf{I} - \mathbf{T}_{k-1})^{-1} (\mathbf{T}_0\mathbf{Q} + \rho_0\mathbf{I}) \\ &= (\mathbf{I} - \mathbf{T}_{k-1})^{-1} \mathbf{T}_0\mathbf{Q} + (\mathbf{I} - \mathbf{T}_{k-1})^{-1} \rho_0\mathbf{I}, \end{aligned}$$

using the definition in (B.8)

$$\begin{aligned} c_0\mathbf{I} &= \mathbf{M}_0\mathbf{Q} + (\mathbf{I} - \mathbf{T}_{k-1})^{-1} \rho_0\mathbf{I} \\ \Rightarrow \mathbf{M}_0 &= -(\mathbf{I} - \mathbf{T}_{k-1})^{-1} \rho_0\mathbf{Q}^{-1} + c_0\mathbf{Q}^{-1}. \end{aligned} \tag{B.9}$$

Similar calculation yields

$$\begin{aligned} \mathbf{M}_1 &= c_1\mathbf{Q}^{-1} + c_0\mathbf{Q}^{-2} - (\mathbf{I} - \mathbf{T}_{k-1})^{-1} \left(\rho_0\mathbf{Q}^{-2} + \rho_1\mathbf{Q}^{-1}\right) \\ &\vdots \\ \mathbf{M}_{k-1} &= c_{k-1}\mathbf{Q}^{-1} + \ldots + c_1\mathbf{Q}^{-k+1} + c_0\mathbf{Q}^{-k} - (\mathbf{I} - \mathbf{T}_{k-1})^{-1} \left(\rho_0\mathbf{Q}^{-k} + \ldots + \rho_{k-1}\mathbf{Q}^{-1}\right). \end{aligned} \tag{B.10}$$

Consider

$$\begin{aligned}\mathbf{M}_{k-1} &= \left(\mathbf{I}-\mathbf{T}_{k-1}\right)^{-1}\mathbf{T}_{k-1}\\ \left(\mathbf{I}-\mathbf{T}_{k-1}\right)\mathbf{M}_{k-1} &= \mathbf{T}_{k-1}\\ \left(\mathbf{I}-\mathbf{T}_{k-1}\right)\left(\mathbf{M}_{k-1}+\mathbf{I}\right) &= \mathbf{I}\\ \mathbf{M}_{k-1}+\mathbf{I} &= \left(\mathbf{I}-\mathbf{T}_{k-1}\right)^{-1}.\end{aligned} \tag{B.11}$$

Substituting (B.11) into (B.10)

$$\begin{aligned}\mathbf{M}_{k-1} &= \left(\mathbf{I}+c_{k-1}\mathbf{Q}^{-1}+\ldots+c_0\mathbf{Q}^{-k}\right)\left(\mathbf{I}+\rho_{k-1}\mathbf{Q}^{-1}+\ldots+\rho_0\mathbf{Q}^{-k}\right)^{-1}-\mathbf{I},\\ \mathbf{M}_{k-2} &= c_{k-2}\mathbf{Q}^{-1}+\ldots+c_0\mathbf{Q}^{-k+1}-\left(\mathbf{M}_{k-1}+\mathbf{I}\right)\left(\rho_{k-2}\mathbf{Q}^{-1}+\ldots+\rho_0\mathbf{Q}^{-k+1}\right),\\ &\vdots\\ \mathbf{M}_1 &= c_1\mathbf{Q}^{-1}+c_0\mathbf{Q}^{-2}-\left(\mathbf{M}_{k-1}+\mathbf{I}\right)\left(\rho_1\mathbf{Q}^{-1}+\rho_0\mathbf{Q}^{-2}\right)\\ \mathbf{M}_0 &= c_0\mathbf{Q}^{-1}-\left(\mathbf{M}_{k-1}+\mathbf{I}\right)\rho_0\mathbf{Q}^{-1}.\end{aligned} \tag{B.12}$$

Thus the particular choice of coefficients given that $\mathbf{Q}$ is nonsingular ensures $\boldsymbol{\eta}^* \to \boldsymbol{\eta}_c$ asymptotically.

It remains to show that the introduced dynamic variable $\mathbf{g}^* \to$ as $t \to \infty$. Firstly, (B.1) is differentiated $(k-1)$-times

$$\begin{aligned}\dot{\boldsymbol{\eta}}^* &= \mathbf{Q}\boldsymbol{\eta}^*+\boldsymbol{\theta}_c+\mathbf{g}^*,\\ \ddot{\boldsymbol{\eta}}^* &= \mathbf{Q}\dot{\boldsymbol{\eta}}^*+\dot{\boldsymbol{\theta}}_c+\dot{\mathbf{g}}^*,\\ &\vdots\\ \boldsymbol{\eta}^{*(k)} &= \mathbf{Q}\boldsymbol{\eta}^{*(k-1)}+\boldsymbol{\theta}_c^{(k-1)}+\mathbf{g}^{*(k-1)}\end{aligned} \tag{B.13}$$

and substituted into (B.2) results in

$$\begin{aligned}&\boldsymbol{\theta}_c^{(k)}+\rho_{k-1}\mathbf{I}_m\boldsymbol{\theta}_c^{(k-1)}+\ldots+\rho_1\mathbf{I}_m\dot{\boldsymbol{\theta}}_c+\rho_0\mathbf{I}_m\boldsymbol{\theta}_c=-\Big[\left(\mathbf{I}-\mathbf{T}_{k-1}\right)\mathbf{g}^{*(k)}+\\ &\quad+\left(\mathbf{T}_{k-1}\mathbf{Q}-\mathbf{T}_{k-2}+\rho_{k-1}\mathbf{I}\right)\mathbf{g}^{*(k-1)}+\ldots+\left(\rho_1\mathbf{I}+\mathbf{T}_1\mathbf{Q}-\mathbf{T}_0\right)\dot{\mathbf{g}}^*+\left(\mathbf{T}_0\mathbf{Q}-\rho_0\mathbf{I}\right)\mathbf{g}^*\Big].\end{aligned} \tag{B.14}$$

If each component $\boldsymbol{\theta}_{c,i},\ i=0,1,\ldots,n-m$ can be defined by a linear exosystem with the characteristic polynomial (6.27), then in steady state

$$\left(s^k+\rho_{k-1}s^{k-1}+\ldots+\rho_1 a+\rho_0\right)\boldsymbol{\theta}_c \equiv \mathbf{0}. \tag{B.15}$$

Thus in *Laplacian* domain

$$\begin{aligned}\Big[s^k\mathbf{I} + s^{k-1}\left(\mathbf{I}-\mathbf{T}_{k-1}\right)^{-1}\left(\mathbf{T}_{k-1}\mathbf{Q}-\mathbf{T}_{k-2}+\rho_{k-1}\mathbf{I}\right)+ \\ +\ldots+\left(\mathbf{I}-\mathbf{T}_{k-1}\right)^{-1}\left(\mathbf{T}_0\mathbf{Q}-\rho_0\mathbf{I}\right)\Big]\,\mathbf{G}^*(s)=\mathbf{0},\end{aligned} \tag{B.16}$$

and due to the particular selection of coefficients (cf. (B.7)) the asymptotic convergence of $\mathbf{g}^* \to \mathbf{0}$ is guaranteed given that $\mathbf{Q}$ is a nonsingular matrix.

C. Sliding Mode Control

C.1. Conventional Sliding Mode

Sliding mode control (SMC)[Utk77], a nonlinear control technique, is considered as one of the main methods for control and observation under uncertainty conditions [Mor+15]. Classified as a kind of variable structure control system, SMC technique alters the dynamics of a system by applying a discontinuous control signal that forces the system to move along a carefully selected surface in the state space. Based on the current state of the system, SMC switches between two (continuous) control laws forcing the system trajectories to move towards a predefined *sliding surface*. This sliding surface is so designed such that the control task is achieved asymptotically (or even in finite time) when the system is in *sliding mode*, i.e. when the system is sliding along the sliding surface.

The design of a sliding mode controller is achieved in two steps. First, an appropriate sliding surface which defines the dynamics of the controlled system is sliding mode is designed [Sht+14]. The second step is to design a discontinuous control law that forces the system trajectories to reach the sliding surface in finite time. This phase is known as the *reaching phase*.

For the sake of illustration consider a double integrator given as

$$\ddot{x} = u, \tag{C.1}$$

and let the choice of the sliding surface, σ be a linear combination of the states gives as

$$\sigma = cx + \dot{x}, \tag{C.2}$$

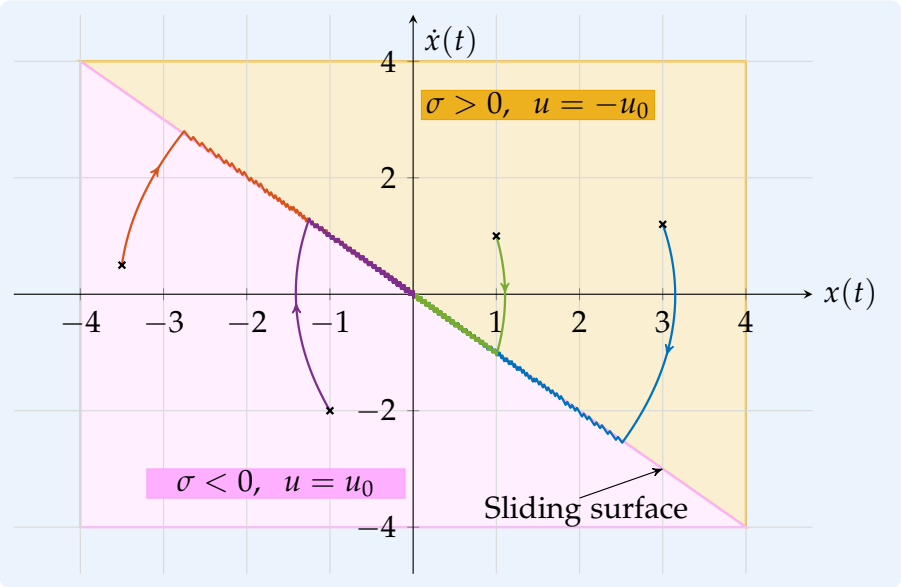

Figure C.1.: System trajectories of the double integrator controlled with SMC

where $c \in \mathbb{R}$ is a constant. Now the (discontinuous) sliding mode control signal is chosen as

$$u = -u_0 \operatorname{sgn}(\sigma), \tag{C.3}$$

where the following definition of the sign operator is used

$$\operatorname{sgn}(s) = \begin{cases} 1, & \text{if } s > 0, \\ 0, & \text{if } s = 0, \\ -1, & \text{if } s < 0. \end{cases} \tag{C.4}$$

Based on this control signal, the state plane can be divided into two semi-planes, the upper and the lower depending on the sign of σ as shown in Figure C.1. Due to the choice of the sign of the control signal based on the present state, the state trajectories are always moving towards the switching line $\sigma = 0$, and once the trajectory reaches this line, they are switched about this line with (theoretically) infinite frequency. So, the trajectories cannot leave this switching line $\sigma = 0$. Thus, the system in sliding mode is governed by the equation $\sigma = cx + \dot{x} = 0$ implying that the time evolution of the system in sliding mode is only influenced by the constant c and not by the original plant parameters and/or disturbances. For example, consider that an unknown bounded disturbance $d(t)$ acts on the double integrator

$$\ddot{x} = u + d(t), \tag{C.5}$$

with $|d(t)| \leq D > 0$. With the same sliding surface as considered before, let us now look at the dynamics of the sliding variable σ

$$\begin{aligned} \dot{\sigma} &= c\dot{x} + \ddot{x} \\ \dot{\sigma} &= c\dot{x} + u + d. \end{aligned} \tag{C.6}$$

In order to make the system trajectories move to the sliding surface and stay there, the sliding variable is made attractive[1] by choosing u such that (using Figure C.1)

$$\sigma\dot{\sigma} \overset{!}{<} 0 \tag{C.7}$$

$$\Rightarrow \dot{\sigma} = -\kappa \operatorname{sgn}(\sigma), \tag{C.8}$$

where the constant $\kappa \in \mathbb{R}$. Using (C.6),

$$u = -\kappa \operatorname{sgn}(\sigma) - d - c\dot{x}. \tag{C.9}$$

Assume that the velocity $\dot{x}(t)$ is measured and can be compensated directly in the control signal. Now, choosing κ such that $\kappa > D$ ensures that the condition (C.8) is met implying that the system trajectories *reach* the sliding surface irrespective of the disturbance acting on the plant. Thus the SMC is robust against perturbations and/or modelling uncertainties in the plant. Another advantage of the sliding mode controller is that once the sliding surface is reached the motion of the trajectories is governed by the 1^{st}-order system, which guarantees that there will be no overshoot in the system response.

Fast switching action around the switching line between $+u_0$ and $-u_0$ is known as the *Chattering* phenomenon (see Figure C.2), and in reality the frequency of this switching action is not infinitely high but is limited due to the physical limitations of the switching element. This chattering behaviour is a disadvantage of the classical SMC law as this control signal will reduce the life of any physical actuator. One well-known technique to avoid the chattering phenomenon is to replace the discontinuous signal with a saturated linear relation within a thin boundary layer neighbouring the sliding surface as shown in(7.35). Another restriction for the use of sliding mode control techniques is that the constraint to be held at zero (σ) has to be of relative degree[2] 1, that is the control needs to explicitly appear in the first time derivative of the constraint. Suppose that the problem

[1] In order to make the surface attractive, using Figure C.1, one can formulate that $\sigma\dot{\sigma} \overset{!}{<} 0$ and the relation (C.8) follows

[2] Refer Section C.4

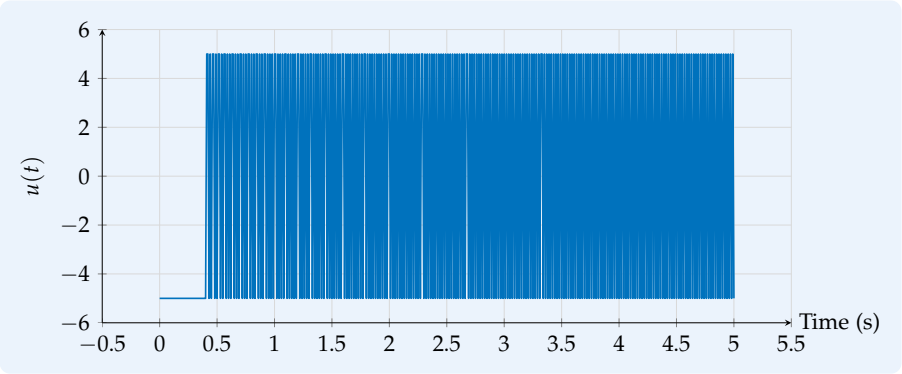

Figure C.2.: Discontinuous control action with SMC

is to keep the sliding variable s at zero and that the control appears in $\ddot{s}$. This problem cannot be tackled with the conventional (classical) sliding mode control. Second- and higher-order sliding mode controllers [Lev93] introduced in Section C.3 are developed for such problems.

C.2. Matched and unmatched disturbances

Consider once again the double integrator with bounded time varying disturbance as mentioned in the previous section. This system is rewritten here in state space with $x_1 := x$ and $x_2 := \dot{x}$

$$\dot{x}_1 = x_2 \tag{C.10a}$$
$$\dot{x}_2 = u + d \tag{C.10b}$$

It has been shown in the previous section that the system dynamics in sliding mode are insensitive to the bounded disturbance $d(t)$. However, one has to bear in mind that the disturbance is entering in the second equation (C.10b). Consider another disturbance $w(t)$ entering in the first equation (C.10a) as follows

$$\dot{x}_1 = x_2 + w \tag{C.11a}$$
$$\dot{x}_2 = u + d \tag{C.11b}$$

where $|w(t)| < W$. Assume that an SMC u is designed such that the trajectories of the system (C.11) reach the sliding surface in finite time and maintain motion on the sliding

surface. In sliding mode the following relation is valid

$$\sigma = 0 \quad \Rightarrow x_2 = -cx_1. \tag{C.12}$$

Therefore the reduced order system dynamics are given as

$$\dot{x}_1 = x_2 + w \tag{C.13a}$$
$$x_2 = -cx_1. \tag{C.13b}$$

It is evident from (C.11) and (C.13) that the disturbance $d(t)$ does not affect the system dynamics in sliding mode while the disturbance $w(t)$ can prevent the states from converging to zero in the sliding mode. Thus, there is a basic difference between $d(t)$ entering the input channel (system equation containing the input u) and $w(t)$. The disturbance $d(t)$ is called a *matched* disturbance (matched by the control) and the disturbance $w(t)$ the *unmatched* disturbance.

C.3. Second-order Sliding mode control

As mentioned in Section C.1, conventional sliding mode provides robustness against matched uncertainties/disturbances, however suffer from two major drawbacks that of relative degree requirement and chattering. Suppose now that it is required to keep the sliding variable s at zero and the control appears in $\ddot{s}$, i.e. the relative degree $\gamma = 2$. Now, one can select a new variable $\sigma = s + \dot{s}$ and then use conventional SMC to make $\sigma = 0$ in finite time, then s tends asymptotically to zero. However keeping it at exact zero is not possible and it is required to estimate $\dot{s}$ which is usually not measured. Both these tasks can be accomplished by the 2-order sliding mode techniques.

Consider the same 2-order technique applied to a system where $\gamma = 1$, by considering the control derivative as a new virtual control input. Then the task of driving s to zero is achieved by means of continuous control as a consequence the chattering effect is significantly attenuated.

As an example for a 2-order sliding mode technique the so-called *super-twisting* control is introduced here. Consider once again the double integrator system with bounded disturbance as in (C.5). Assuming that the term $\varphi(t, \dot{x}) := c\dot{x} + d = 0$ in the sliding variable dynamics (C.6), choose the following continuous control

$$u = -k|\sigma|^{1/2}\,\mathrm{sgn}(\sigma), \quad k > 0. \tag{C.14}$$

Then the sliding variable dynamics (C.6) become

$$\dot{\sigma} = -k|\sigma|^{1/2}\,\mathrm{sgn}(\sigma), \tag{C.15}$$

and it is clear that the sliding variable σ reaches zero in finite time. However, when the term $\varphi(t, \dot{x}) \neq 0$, the σ-dynamics become

$$\dot{\sigma} = c\dot{x} + d - k|\sigma|^{1/2}\,\mathrm{sgn}(\sigma) \tag{C.16}$$

and convergence to zero does not occur. If an additional term that tracks $\varphi(t, \dot{x})$ in finite time is added to the control input u, then the disturbance will be completely compensated. Towards this goal the following extension for u is presented [EKL93]

$$u = k_1|\sigma|^{1/2}\,\mathrm{sgn}(\sigma) + u_1 \tag{C.17}$$

$$\dot{u}_1 = k_2\,\mathrm{sgn}(\sigma). \tag{C.18}$$

Also let the term $|\dot{\varphi}(t, \dot{x})| < C$, the by choosing $k_2 = 1.1C$ and $k_1 = 1.5\sqrt{C}$ the goal of driving σ to zero in finite time is achieved as the term u_1 becomes equal to $\varphi(t, \dot{x})$ in finite time. Finally the super-twisting is continuous since both $k_1|\sigma|^{1/2}$ and $u_1 = k_2 \int \mathrm{sgn}(\sigma)dt$ are continuous.

C.4. Relative degree

Consider a single-input, single-output system described as

$$\dot{\mathbf{x}} = \mathbf{f}(\mathbf{x}) + \mathbf{g}(\mathbf{x})u \tag{C.19}$$

$$y = h(\mathbf{x}), \tag{C.20}$$

where $\mathbf{x} \in \mathbb{R}^n$, u and $y \in \mathbb{R}$ and $\mathbf{f} : \mathbb{R}^n \to \mathbb{R}^n, \mathbf{g} : \mathbb{R}^n \to \mathbb{R}^n$ are smooth vector fields and $h : \mathbb{R}^n \to \mathbb{R}$ a smooth scalar function of the state $\mathbf{x}$. Then the derivative of y with respect to time is given by

$$\frac{dy}{dt} = \frac{\partial h}{\partial \mathbf{x}}\frac{dx}{dt}, \tag{C.21}$$

using Equation (C.19)

$$\frac{dy}{dt} = \frac{\partial h}{\partial \mathbf{x}}\left(\mathbf{f}(\mathbf{x}) + \mathbf{g}(\mathbf{x})u\right). \tag{C.22}$$

Rearranging Equation (C.22) results in

$$\frac{dy}{dt} = \underbrace{\frac{\partial h}{\partial \mathbf{x}}\mathbf{f}(\mathbf{x})}_{:=L_{\mathbf{f}}h} + \underbrace{\frac{\partial h}{\partial \mathbf{x}}\mathbf{g}(\mathbf{x})}_{:=L_{\mathbf{g}}h} u, \tag{C.23}$$

where the scalar functions $L_{\mathbf{f}}h$ and $L_{\mathbf{g}}h$ are the *Lie derivatives* [Sch36] of function h with respect to (or along) the vector fields $\mathbf{f}(\mathbf{x})$ and $\mathbf{g}(\mathbf{x})$ respectively. Thus, the Lie derivative $L_{\mathbf{f}}h$ can be interpreted as the derivative of h along integral curves (or solution trajectories) of the vector field $\mathbf{f}$. Higher order Lie derivatives are defined similarly

$$L_{\mathbf{f}}^2 h := L_{\mathbf{f}}(L_{\mathbf{f}}h) = \frac{\partial (L_{\mathbf{f}}h)}{\partial \mathbf{x}}\mathbf{f}(\mathbf{x}). \tag{C.24}$$

If the first derivative of the output $\dot{y}$ is not influenced by the input signal u, i.e. $L_{\mathbf{g}}h \equiv 0$ for all $\mathbf{x}$ in some neighbourhood of $\mathbf{0}$. Then (C.23) becomes

$$\dot{y} = L_{\mathbf{f}}h. \tag{C.25}$$

The second derivative of the output is

$$\frac{d^2y}{dt^2} = L_{\mathbf{f}}^2 h + L_{\mathbf{g}}(L_{\mathbf{f}}h)u. \tag{C.26}$$

Again if we consider $L_{\mathbf{g}}(L_{\mathbf{f}}h) \equiv 0$, $\forall \mathbf{x}$ in some neighbourhood of $\mathbf{0}$,

$$\begin{aligned} \frac{dy}{dt} &= L_{\mathbf{f}}h \\ \frac{d^2y}{dt^2} &= L_{\mathbf{f}}^2 h \\ &\vdots \\ \frac{d^\gamma y}{dt^\gamma} &= L_{\mathbf{f}}^\gamma h + L_{\mathbf{g}}\left(L_{\mathbf{f}}^{\gamma-1}h\right) u. \end{aligned} \tag{C.27}$$

It is assumed that the γ^{th}-derivative of $y(t)$ "sees" the input signal $u(t)$. In this case the system described by (C.19) and (C.20) is said to have a *relative degree* γ.

In order to understand the meaning of relative degree γ in the case of a linear system consider the following state space realization of an LTI SISO system of order n with input u and output y

$$\dot{\mathbf{x}}(t) = \mathbf{A}\mathbf{x}(t) + \mathbf{b}u(t), \quad y(t) = \mathbf{c}^T\mathbf{x}(t) + du(t). \tag{C.28}$$

The transfer function for the realization given above is given as

$$G(s) := \frac{y(s)}{u(s)} = d + \mathbf{c}^T(s\mathbf{I} - \mathbf{A})^{-1}\mathbf{b}. \tag{C.29}$$

Consider that the determinant of the characteristic polynomial, $\det(s\mathbf{I} - \mathbf{A})$ is known and given as

$$\det(s\mathbf{I} - \mathbf{A}) = s^n + a_{n-1}s^{n-1} + \ldots + a_1 s + a_0, \tag{C.30}$$

where $a_i \in \mathbb{R}$ for $i = 0, 1, \ldots, n-1$.
Also let

$$\mathrm{Adj}(s\mathbf{I} - \mathbf{A}) = \mathbf{B}_0 s^{n-1} + \mathbf{B}_1 s^{n-2} + \ldots + \mathbf{B}_{n-2}s + \mathbf{B}_{n-1}, \tag{C.31}$$

where $\mathbf{B}_i \in \mathbb{R}^{n\times n}$ for $i = 0, 1, \ldots, n-1$ are constant matrices[3] [Ros70]. We have that

$$(s\mathbf{I} - \mathbf{A})\,\mathrm{adj}(s\mathbf{I} - \mathbf{A}) = \det(s\mathbf{I} - \mathbf{A})\mathbf{I}. \tag{C.32}$$

Substituting (C.31), the left hand side of (C.32)

$$\begin{aligned}(s\mathbf{I} - \mathbf{A}) &\left(\mathbf{B}_0 s^{n-1} + \mathbf{B}_1 s^{n-2} + \ldots + \mathbf{B}_{n-2}s + \mathbf{B}_{n-1}\right) \\ &= \mathbf{B}_0 s^n + (\mathbf{B}_1 - \mathbf{A}\mathbf{B}_0)\, s^{n-1} + \ldots + (\mathbf{B}_{n-1} - \mathbf{A}\mathbf{B}_{n-2})\, s - \mathbf{A}\mathbf{B}_{n-1}.\end{aligned} \tag{C.33}$$

A comparison of coefficients with the right hand side of (C.31) using (C.30) results in

$$\left.\begin{aligned}\mathbf{B}_0 &= \mathbf{I} \\ \mathbf{B}_1 - \mathbf{A}\mathbf{B}_0 &= a_{n-1}\mathbf{I} \\ \mathbf{B}_2 - \mathbf{A}\mathbf{B}_1 &= a_{n-2}\mathbf{I} \\ &\vdots \\ \mathbf{B}_{n-1} - \mathbf{A}\mathbf{B}_{n-2} &= a_1\mathbf{I} \\ -\mathbf{A}\mathbf{B}_{n-1} &= a_0\mathbf{I}\end{aligned}\right\}. \tag{C.34}$$

Using the relation $(s\mathbf{I} - \mathbf{A})^{-1} = \frac{1}{\det(s\mathbf{I}-\mathbf{A})}\,\mathrm{adj}(s\mathbf{I} - \mathbf{A})$,(C.31) and (C.34) the transfer function (C.29) is rewritten as

$$G(s) = d + \frac{\begin{aligned}(s^{n-1} + a_{n-1}s^{n-2} + \ldots + a_2 s + a_1)\mathbf{c}^T\mathbf{b} + \\ (s^{n-2} + \ldots + a_3 s + a_2)\mathbf{c}^T\mathbf{A}\mathbf{b} + \ldots \\ \ldots + (s + a_{n-1})\mathbf{c}^T\mathbf{A}^{n-2}\mathbf{b} + \\ + \mathbf{c}^T\mathbf{A}^{n-1}\mathbf{b}\end{aligned}}{s^n + a_{n-1}s^{n-1} + \ldots + a_1 s + a_0}. \tag{C.35}$$

[3]The order of the polynomial in (C.31) is $n-1$ as the adjoint matrix is composed of determinants of the cofactor matrices of $s\mathbf{I} - \mathbf{A}$ which have the dimension $n-1$.

If the difference of the degree of denominator and numerator polynomials of a given transfer function is represented by δ, then the value of δ can easily be calculated using the system parameters.
Consider the case when $d = 0$[4], the degree difference δ depends on the existence of the terms given by $\mathbf{c}^T\mathbf{A}^{j-1}\mathbf{b}$ for $j = 1, 2, \ldots, n$ as follows

$$\delta = \min\left\{ j \ : \ \mathbf{c}^T\mathbf{A}^{j-1}\mathbf{b} \neq 0; \quad j = 1, 2, \ldots, n \right\}. \tag{C.36}$$

The vectors $\mathbf{c}^T\mathbf{A}^{j-1}\mathbf{b}$ for $j = 1, 2, \ldots, n$ are precisely the vectors that influence the effect of input u on the j^{th} derivative of the output y. So, the degree difference δ and relative degree γ are identical in the case of linear systems.

[4]If $d \neq 0$ then $\delta = 0$.

Bibliography

[ABP04a] N. Amann, J. Bocker, and F. Prenner. "Active damping of drive train oscillations for an electrically driven vehicle." In: *Mechatronics, IEEE/ASME Transactions on* 9.4 (Dec. 2004), pp. 697–700. ISSN: 1083-4435. DOI: 10.1109/TMECH.2004.839036.

[ABP04b] Notker Amann, Joachim Böcker, and Franz Prenner. "Active damping of drive train oscillations for an electrically driven vehicle." In: *Mechatronics, IEEE/ASME Transactions on* 9.4 (2004), pp. 697–700.

[ACO] B&R ACOPOSmulti. *B&R ACOPOSmulti*. URL: http://www.br-automation.com/en/products/motion-control/acoposmulti/ (visited on 09/01/2015).

[AH11] U. Angeringer and M. Horn. "Sliding mode drive line control for an electrically driven vehicle." In: *Control Applications (CCA), 2011 IEEE International Conference on*. Sept. 2011, pp. 521–526. DOI: 10.1109/CCA.2011.6044416.

[ÅH95] Karl J Åström and Tore Hägglund. "PID controllers: theory, design, and tuning." In: *Instrument Society of America, Research Triangle Park, NC* (1995).

[BCP95] K. Brenan, S. Campbell, and L. Petzold. *Numerical Solution of Initial-Value Problems in Differential-Algebraic Equations*. Society for Industrial and Applied Mathematics, 1995. DOI: 10.1137/1.9781611971224. eprint: http://epubs.siam.org/doi/pdf/10.1137/1.9781611971224. URL: http://epubs.siam.org/doi/abs/10.1137/1.9781611971224.

[BI88] C.I. Byrnes and A. Isidori. "Local Stabilization of Minimum-phase Nonlinear Systems." In: *Syst. Control Lett.* 11.1 (July 1988), pp. 9–17. ISSN: 0167-6911. DOI: 10.1016/0167-6911(88)90105-3. URL: http://dx.doi.org/10.1016/0167-6911(88)90105-3.

[BI91] C.I. Byrnes and A. Isidori. "Asymptotic stabilization of minimum phase nonlinear systems." In: *Automatic Control, IEEE Transactions on* 36.10 (Oct. 1991), pp. 1122–1137. ISSN: 0018-9286. DOI: 10.1109/9.90226.

[BRA] B&R-Automation. *br-automation*. URL: http://www.br-automation.com/perfection-in-automation/ (visited on 09/01/2015).

[Che95] Chi-Tsong Chen. *Analog and Digital Control System Design: Transfer-function, State-space, and Algebraic Methods*. New York, NY, USA: Oxford University Press, Inc., 1995. ISBN: 0030940702.

[CP96] Degang Chen and BRAD Paden. "Stable inversion of nonlinear non-minimum phase systems." In: *International Journal of Control* 64.1 (1996), pp. 81–97.

[CS90] C. T. Chen and B. Seo. "The Inward Approach in the Design of Control Systems." In: *IEEE Trans. on Educ.* 33.3 (Aug. 1990), pp. 270–278. ISSN: 0018-9359. DOI: 10.1109/13.57072. URL: http://dx.doi.org/10.1109/13.57072.

[DCP96] Santosh Devasia, Degang Chen, and Brad Paden. "Nonlinear inversion-based output tracking." In: *Automatic Control, IEEE Transactions on* 41.7 (1996), pp. 930–942.

[DKT92] R. Dhaouadi, Kenji Kubo, and M. Tobise. "Two-degree-of-freedom robust speed controller for high performance rolling mill drives." In: *Industry Applications Society Annual Meeting, 1992., Conference Record of the 1992 IEEE*. Oct. 1992, 400–407 vol.1. DOI: 10.1109/IAS.1992.244367.

[EG01] G. Ellis and Zhiqiang Gao. "Cures for low-frequency mechanical resonance in industrial servo systems." In: *Industry Applications Conference, 2001. Thirty-Sixth IAS Annual Meeting. Conference Record of the 2001 IEEE*. Vol. 1. Sept. 2001, 252–258 vol.1. DOI: 10.1109/IAS.2001.955419.

[EKL93] S. V. Emel'yanov, S. K. Korovin, and A. Levant. "High-order sliding modes in control systems." In: *Computational Mathematics and Modeling* 7.3 (1993), pp. 294–318. ISSN: 1573-837X. DOI: 10.1007/BF01128162. URL: http://dx.doi.org/10.1007/BF01128162.

[Ell04] G.H. Ellis. *Control System Design Guide: A Practical Guide*. Electronics & Electrical. Academic Press, Incorporated, 2004. ISBN: 9780122374616.

[ES98] C. Edwards and S. Spurgeon. *Sliding Mode Control: Theory And Applications*. Series in Systems and Control. Taylor & Francis, 1998. ISBN: 9780748406012. URL: https://books.google.at/books?id=uH2RJhIPsiYC.

[Gaw07] Wodek Gawronski. "Control and Pointing Challenges of Large Antennas and Telescopes." In: *Control Systems Technology, IEEE Transactions on* 15.2 (Mar. 2007), pp. 276–289. ISSN: 1063-6536. DOI: 10.1109/TCST.2006.886434.

[GK93] S. Goplaswamy and J. Karl Hedrick. "Tracking nonlinear non-minimum phase systems using sliding control." In: *International Journal of Control* 57.5 (1993), pp. 1141–1158. DOI: 10.1080/00207179308934436. eprint: http://dx.doi.org/10.1080/00207179308934436. URL: http://dx.doi.org/10.1080/00207179308934436.

[Hau70] M.L.J. Hautus. "Stabilization controllability and observability of linear autonomous systems." In: *Indagationes Mathematicae (Proceedings)* 73 (1970), pp. 448–455. ISSN: 1385-7258. DOI: http://dx.doi.org/10.1016/S1385-7258(70)80049-X. URL: http://www.sciencedirect.com/science/article/pii/S138572587080049X.

[HEE01] Jürgen Hahn, Thomas Edison, and Thomas F Edgar. "A note on stability analysis using Bode plots." In: *Chemical Engineering Education* 35.3 (2001), pp. 208–211.

[HN04] Martin Horn and Dourdoumas Nicolaos. *Regelungstechnik: rechnerunterstützter Entwurf zeitkontinuierlicher und zeitdiskreter Regelkreise*. Elektrotechnik : Regelungstechnik. Pearson Studium, 2004. ISBN: 9783827372604. URL: http://books.google.at/books?id=1BgxPQAACAAJ.

[HSC99] Y. Hori, H. Sawada, and Yeonghan Chun. "Slow resonance ratio control for vibration suppression and disturbance rejection in torsional system." In: *Industrial Electronics, IEEE Transactions on* 46.1 (Feb. 1999), pp. 162–168. ISSN: 0278-0046. DOI: 10.1109/41.744407.

[Hua04] J. Huang. *Nonlinear Output Regulation*. Society for Industrial and Applied Mathematics, 2004. DOI: 10.1137/1.9780898718683. eprint: http://epubs.siam.org/doi/pdf/10.1137/1.9780898718683. URL: http://epubs.siam.org/doi/abs/10.1137/1.9780898718683.

[IB90] A. Isidori and C.I. Byrnes. "Output regulation of nonlinear systems." In: *Automatic Control, IEEE Transactions on* 35.2 (Feb. 1990), pp. 131–140. ISSN: 0018-9286. DOI: 10.1109/9.45168.

[IIM04] K. Itoh, M. Iwasaki, and N. Matsui. "Optimal design of robust vibration suppression controller using genetic algorithms." In: *Industrial Electronics, IEEE Transactions on* 51.5 (Oct. 2004), pp. 947–953. ISSN: 0278-0046. DOI: 10.1109/TIE.2004.834943.

[int] EnDAT interface. *EnDAT interface*. URL: http://www.heidenhain.com/en_US/fundamentals/interfaces/endat-22/ (visited on 09/01/2014).

[Isi95] Alberto Isidori. *Nonlinear Control Systems*. Ed. by M. Thoma et al. 3rd. Secaucus, NJ, USA: Springer-Verlag New York, Inc., 1995. ISBN: 3540199160.

[IYH05] Y. Izumikawa, K. Yubai, and J. Hirai. "Fault-tolerant control system of flexible arm for sensor fault by using reaction force observer." In: *Mechatronics, IEEE/ASME Transactions on* 10.4 (Aug. 2005), pp. 391–396. ISSN: 1083-4435. DOI: 10.1109/TMECH.2005.852442.

[JS95] Jun-Keun Ji and Seung-Ki Sul. "Kalman filter and LQ based speed controller for torsional vibration suppression in a 2-mass motor drive system." In: *Industrial Electronics, IEEE Transactions on* 42.6 (Dec. 1995), pp. 564–571. ISSN: 0278-0046. DOI: 10.1109/41.475496.

[Kal59] Rudolf Kalman. "On the general theory of control systems." In: *IRE Transactions on Automatic Control* 4.3 (1959), pp. 110–110.

[Kha02] H.K. Khalil. *Nonlinear Systems*. Pearson Education. Prentice Hall, 2002. ISBN: 9780130673893. URL: https://books.google.at/books?id=t%5C_d1QgAACAAJ.

[KM06] P. Kunkel and V.L. Mehrmann. *Differential-algebraic Equations: Analysis and Numerical Solution*. EMS textbooks in mathematics. European Mathematical Society, 2006. ISBN: 9783037190173. URL: http://books.google.at/books?id=iRZPqCwkI%5C_IC.

[KO07] S. Katsura and K. Ohnishi. "Absolute Stabilization of Multimass Resonant System by Phase-Lead Compensator Based on Disturbance Observer." In: *Industrial Electronics, IEEE Transactions on* 54.6 (Dec. 2007), pp. 3389–3396. ISSN: 0278-0046. DOI: 10.1109/TIE.2007.903931.

[Kri01] R. Krishnan. *Electric Motor Drives: Modeling, Analysis, and Control*. Prentice Hall, 2001. ISBN: 9780130910141. URL: http://books.google.at/books?id=1lgtAQAAMAAJ.

[KSD00] I.N. Kar, K. Seto, and F. Doi. "Multimode vibration control of a flexible structure using H infin;-based robust control." In: *Mechatronics, IEEE/ASME Transactions on* 5.1 (Mar. 2000), pp. 23–31. ISSN: 1083-4435. DOI: 10.1109/3516.828586.

[LBF13] Alejandra Ferreira de Loza, Francisco J. Bejarano, and Leonid Fridman. "Unmatched uncertainties compensation based on high-order sliding mode observation." In: *International Journal of Robust and Nonlinear Control* 23.7 (2013), pp. 754–764. ISSN: 1099-1239. DOI: 10.1002/rnc.2795. URL: http://dx.doi.org/10.1002/rnc.2795.

[Lev03] Arie Levant. "Higher-order sliding modes, differentiation and output-feedback control." In: *International Journal of Control* 76.9-10 (2003), pp. 924–941. DOI: 10.1080/0020717031000099029.

[Lev93] Arie Levant. "Sliding order and sliding accuracy in sliding mode control." In: *International journal of control* 58.6 (1993), pp. 1247–1263.

[Lev98] Arie Levant. "Robust exact differentiation via sliding mode technique." In: *Automatica* 34.3 (Mar. 1998), pp. 379–384. ISSN: 00051098. DOI: 10.1016/S0005-1098(97)00209-4. URL: http://www.sciencedirect.com/science/article/pii/S0005109897002094.

[MK93] N.A. Mahmoud and H.K. Khalil. "Asymptotic stabilization of minimum phase nonlinear systems using output feedback." In: *Decision and Control, 1993., Proceedings of the 32nd IEEE Conference on*. Dec. 1993, 1960–1965 vol.3. DOI: 10.1109/CDC.1993.325538.

[Mor+15] Jaime A Moreno et al. "Adaptive continuous twisting algorithm." In: *International Journal of Control* (2015), pp. 1–9.

[MP05] Leonid Mirkin and ZalmanJ. Palmor. "Control Issues in Systems with Loop Delays." In: *Handbook of Networked and Embedded Control Systems*. Ed. by Dimitrios Hristu-Varsakelis and WilliamS. Levine. Control Engineering. Birkhäuser Boston, 2005, pp. 627–648. ISBN: 978-0-8176-3239-7. DOI: 10.1007/0-8176-4404-0_27. URL: http://dx.doi.org/10.1007/0-8176-4404-0_27.

[MRH10] Vamsi P Makkapati, Markus Reichhartinger, and Martin Horn. "A testbench for high-speed printing." In: *Modelling, Identification, and Control (MIC 2010)*. Vol. 675. 053. 2010, p. 161.

[MRH12] Vamsi Prakash Makkapati, Markus Reichhartinger, and Martin Horn. "Performance improvement of servo drives with mechanical elasticity via Extended Acceleration Feedback." In: *Control Applications (CCA), 2012 IEEE International Conference on*. IEEE. 2012, pp. 1279–1284.

[MRH13] Vamsi Prakash Makkapati, Markus Reichhartinger, and Martin Horn. "Output tracking for dual-inertia system with dead time based on stable system center approach." In: *Control Applications (CCA), 2013 IEEE International Conference on*. IEEE. 2013, pp. 923–928.

[Pal80] Z. Palmor. "Stability properties of Smith dead-time compensator controllers." In: *International Journal of Control* 32.6 (1980), pp. 937–949.

[Par+03] Tae-Sik Park et al. "Robust speed control for torsional vibration suppression of rolling mill drive system." In: *Industrial Electronics Society, 2003. IECON '03. The 29th Annual Conference of the IEEE*. Vol. 1. Nov. 2003, 66–71 vol.1. DOI: 10.1109/IECON.2003.1279956.

[Par04] Jonathan R. Partington. "Some frequency-domain approaches to the model reduction of delay systems." In: *Annual Reviews in Control* 28.1 (2004), pp. 65–73. ISSN: 1367-5788. DOI: http://dx.doi.org/10.1016/j.arcontrol.2004.01.007. URL: http://www.sciencedirect.com/science/article/pii/S1367578804000094.

[Per+07] M.-C. Pera et al. "Enhanced Servo-Control Performance of Dual-Mass Systems." In: *Industrial Electronics, IEEE Transactions on* 54.3 (June 2007), pp. 1387–1399. ISSN: 0278-0046. DOI: 10.1109/TIE.2007.893048.

[Pet97] Magnus Pettersson. "Driveline modeling and control." PhD thesis. Department of Electrical Engineering, Linköping University, 1997.

[Qua] Quanser. *Quanser*. URL: http://www.quanser.com/products/rotary_flexible_joint (visited on 09/01/2015).

[Ros70] H. H. Rosenbrock. *State-Space and Multivariable Theory*. 1970.

[RRF05] J. Reger, H.S. Ramirez, and M. Fliess. "On non-asymptotic observation of nonlinear systems." In: *Decision and Control, 2005 and 2005 European Control*

Conference. CDC-ECC '05. 44th IEEE Conference on. Dec. 2005, pp. 4219–4224. DOI: 10.1109/CDC.2005.1582824.

[Scho9] D. Schröder. *Elektrische Antriebe - Regelung von Antriebssystemen*. Bd. 10. Springer, 2009. ISBN: 9783540896128. URL: http://books.google.at/books?id=imfgNLeW2RAC.

[Sch36] Haantjes J. Schouten J. A. "Zur allgemeinen projektiven Differentialgeometrie." ger. In: *Compositio Mathematica* 3 (1936), pp. 1–51. URL: http://eudml.org/doc/88622.

[Sht+12] Y. Shtessel et al. "Sliding Modes after the First Decade of the 21st Century: State of the Art." In: ed. by Leonid Fridman, Jaime Moreno, and Rafael Iriarte. Berlin, Heidelberg: Springer Berlin Heidelberg, 2012. Chap. Output Tracking and Observation in Nonminimum Phase Systems via Classical and Higher Order Sliding Modes, pp. 351–380. ISBN: 978-3-642-22164-4. DOI: 10.1007/978-3-642-22164-4_13. URL: http://dx.doi.org/10.1007/978-3-642-22164-4_13.

[Sht+14] Yuri Shtessel et al. *Sliding mode control and observation*. Springer, 2014.

[Sht97] Y.B. Shtessel. "Nonlinear output tracking in conventional and dynamic sliding manifolds." In: *Automatic Control, IEEE Transactions on* 42.9 (Sept. 1997), pp. 1282–1286. ISSN: 0018-9286. DOI: 10.1109/9.623093.

[Smi57] O. J. M. Smith. "Closer Control of Loops with Dead Time." In: *Chemical Engineering Progress* 53.5 (1957), pp. 217–219.

[SO06] K. Szabat and T. Orlowska-Kowalska. "Adaptive Control of Two-Mass System using Nonlinear Extended Kalman Filter." In: *IEEE Industrial Electronics, IECON 2006 - 32nd Annual Conference on*. Nov. 2006, pp. 1539–1544. DOI: 10.1109/IECON.2006.347970.

[SO07] K. Szabat and T. Orlowska-Kowalska. "Vibration Suppression in a Two-Mass Drive System Using PI Speed Controller and Additional Feedbacks - Comparative Study." In: *Industrial Electronics, IEEE Transactions on* 54.2 (Apr. 2007), pp. 1193–1206. ISSN: 0278-0046. DOI: 10.1109/TIE.2007.892608.

[SO08] K. Szabat and T. Orlowska-Kowalska. "Performance Improvement of Industrial Drives With Mechanical Elasticity Using Nonlinear Adaptive

Kalman Filter." In: *IEEE Transactions on Industrial Electronics* 55.3 (Mar. 2008), pp. 1075–1084. ISSN: 0278-0046. DOI: 10.1109/TIE.2008.917081.

[SP05] Sigurd Skogestad and Ian Postlethwaite. *Multivariable Feedback Control: Analysis and Design*. John Wiley & Sons, 2005. ISBN: 0470011688.

[SR99] P. Schmidt and T. Rehm. "Notch filter tuning for resonant frequency reduction in dual inertia systems." In: *Industry Applications Conference, 1999. Thirty-Fourth IAS Annual Meeting. Conference Record of the 1999 IEEE*. Vol. 3. 1999, 1730–1734 vol.3. DOI: 10.1109/IAS.1999.805973.

[SS01] Ilya A Shkolnikov and Yuri B Shtessel. "Tracking controller design for a class of nonminimum-phase systems via the method of system center." In: *Automatic Control, IEEE Transactions on* 46.10 (2001), pp. 1639–1643.

[SS02] Ilya A. Shkolnikov and Yuri B. Shtessel. "Tracking in a class of nonminimum-phase systems with nonlinear internal dynamics via sliding mode control using method of system center." In: *Automatica* 38.5 (2002), pp. 837–842. ISSN: 0005-1098. DOI: http://dx.doi.org/10.1016/S0005-1098(01)00275-8. URL: http://www.sciencedirect.com/science/article/pii/S0005109801002758.

[Sva06] Ferdinand Svaricek. "Nulldynamik linearer und nichtlinearer Systeme: Definitionen, Eigenschaften und Anwendungen (Zero Dynamics of Linear and Nonlinear Systems: Definitions, Properties and Applications)." In: *at-Automatisierungstechnik* 54.7/2006 (2006), pp. 310–322.

[UGS99] Vadim Ivanovitch Utkin, Jürgen Guldner, and Jingxin Shi. *Sliding mode control in electromechanical systems*. The Taylor & Francis systems and control book series. London, Philadelphia, PA: Taylor & Francis, 1999. ISBN: 0-7484-0116-4. URL: http://opac.inria.fr/record=b1100341.

[Utk77] V. I. Utkin. "Survey paper variable structure systems with sliding modes." In: *IEEE Transactions on Automatic control* 22.2 (1977), pp. 212–222.

[Utk81] V. I. Utkin. "Principles of identification using sliding regimes." In: *Soviet Physics Doklady* 26 (Mar. 1981), p. 271.

[Val+05a] M.A. Valenzuela et al. "Dynamic compensation of torsional oscillation in paper machine sections." In: *Pulp and Paper Industry Technical Conference, 2005. Conference Record of 2005 Annual*. June 2005, pp. 81–90. DOI: 10.1109/PAPCON.2005.1502052.

[Val+05b] M.A. Valenzuela et al. "Dynamic compensation of torsional oscillation in paper machine sections." In: *Pulp and Paper Industry Technical Conference, 2005. Conference Record of 2005 Annual*. June 2005, pp. 81–90. DOI: 10.1109/PAPCON.2005.1502052.

[VBL05] M.A. Valenzuela, J.M. Bentley, and R.D. Lorenz. "Evaluation of torsional oscillations in paper machine sections." In: *Industry Applications, IEEE Transactions on* 41.2 (Mar. 2005), pp. 493–501. ISSN: 0093-9994. DOI: 10.1109/TIA.2005.844383.

[Vid02] M. Vidyasagar. *Nonlinear Systems Analysis*. Classics in Applied Mathematics. Society for Industrial and Applied Mathematics, 2002. ISBN: 9780898715262. URL: https://books.google.de/books?id=%5C_JLrm1rRRUIC.

[VPE05] S. Villwock, M. Pacas, and T. Eutebach. "Application of the Welch-method for the automatic parameter identification of electrical drives." In: *Industrial Electronics Society, 2005. IECON 2005. 31st Annual Conference of IEEE*. Nov. 2005. DOI: 10.1109/IECON.2005.1569118.

[Vuk12] S.N. Vukosavic. *Electrical Machines*. Power Electronics and Power Systems. Springer, 2012. ISBN: 9781461403999. URL: http://books.google.ca/books?id=GgKeQLVw-tAC.

[Wan+06] Jianhui Wang et al. "Torsional Vibration Suppression of Rolling Mill with Constrained Model Predictive Control." In: *Intelligent Control and Automation, 2006. WCICA 2006. The Sixth World Congress on*. Vol. 2. 2006, pp. 6401–6405. DOI: 10.1109/WCICA.2006.1714317.

[WGH13] J. Weissbacher, E. Grünbacher, and M. Horn. "Automatic tuning of a servo drive speed controller for industrial applications." In: *Mechatronics (ICM), 2013 IEEE International Conference on*. Feb. 2013, pp. 700–705. DOI: 10.1109/ICMECH.2013.6519127.

[Won79] W. Murray Wonham. *Linear multivariable control : a geometric approach / W. Murray Wonham*. 2d ed. Springer-Verlag New York, 1979, xv, 326 p. : ISBN: 0387903542.

[WS00] H. Wertz and F. Schutte. "Self-tuning speed control for servo drives with imperfect mechanical load." In: *Industry Applications Conference, 2000.*

Conference Record of the 2000 IEEE. Vol. 3. 2000, 1497–1504 vol.3. DOI: 10.1109/IAS.2000.882081.

[Yan+14] J. Yang et al. "High-Order Mismatched Disturbance Compensation for Motion Control Systems Via a Continuous Dynamic Sliding-Mode Approach." In: *IEEE Transactions on Industrial Informatics* 10.1 (Feb. 2014), pp. 604–614. ISSN: 1551-3203. DOI: 10.1109/TII.2013.2279232.

[YLY13] J. Yang, S. Li, and X. Yu. "Sliding-Mode Control for Systems With Mismatched Uncertainties via a Disturbance Observer." In: *IEEE Transactions on Industrial Electronics* 60.1 (Jan. 2013), pp. 160–169. ISSN: 0278-0046. DOI: 10.1109/TIE.2012.2183841.

[ZD04] Qingze Zou and Santosh Devasia. "Preview-based inversion of nonlinear nonminimum-phase systems: VTOL example." In: *Decision and Control, 2004. CDC. 43rd IEEE Conference on*. Vol. 4. IEEE. 2004, pp. 4350–4356.

[Zha00] G. Zhang. "Speed control of two-inertia system by PI/PID control." In: *Industrial Electronics, IEEE Transactions on* 47.3 (June 2000), pp. 603–609. ISSN: 0278-0046. DOI: 10.1109/41.847901.

[ZRH07] Josef Zehetner, Johann Reger, and Martin Horn. "A derivative estimation toolbox based on algebraic methods-Theory and practice." In: *Control Applications, 2007. CCA 2007. IEEE International Conference on*. IEEE. 2007, pp. 331–336.